FINAL TECHNICAL REPORT

SUBMITTED TO

U.S. Department of Energy
National Energy Technology Laboratory

PROJECT:

DE-FE0009562

Wellbore Seal Repair Using Nanocomposite Materials

Project Period – 10/01/2012 to 8/31/2016

SUBMITTED BY

PD/PI: John Stormont
505-277-6063, 505-277-1988 (fax), jcstorm@unm.edu
University of New Mexico
Department of Civil Engineering
Albuquerque, NM 87131

November 21, 2016

DUNS 868853094

Signed: John C. Stormont, Ph.D., P.E.
Program Director

DISCLAIMER

ACKNOWLEDGEMENT

This material is based upon work supported by the U.S. Department of Energy (DOE) National Energy Technology Laboratory (NETL) under Grant Number DEFE0009562. This project is managed and administered by the University of New Mexico and funded by DOE/NETL and cost-sharing partners.

ABSTRACT

Nanocomposite wellbore repair materials have been developed, tested, and modeled through an integrated program of laboratory testing and numerical modeling. Numerous polymer-cement nanocomposites were synthesized as candidate wellbore repair materials using various combinations of base polymers and nanoparticles. Based on tests of bond strength to steel and cement, ductility, stability, flowability, and penetrability in opening of 50 microns and less, we identified Novolac epoxy reinforced with multi-walled carbon nanotubes and/or alumina nanoparticles to be a superior wellbore seal material compared to conventional microfine cements.

A system was developed for testing damaged and repaired wellbore specimens comprised of a cement sheath cast on a steel casing. The system allows independent application of confining pressures and casing pressures while gas flow is measured through the specimens along the wellbore axis. Repair with the nanocomposite epoxy base material was successful in dramatically reducing the flow through flaws of various sizes and types, and restoring the specimen comparable to an intact condition. In contrast, repair of damaged specimens with microfine cement was less effective, and the repair degraded with application of stress. Post-test observations confirm the complete penetration and sealing of flaws using the nanocomposite epoxy base material.

A number of modeling efforts have supported the material development and testing efforts. We have modeled the steel-repair material interface behavior in detail during slant shear tests, which we used to characterize bond strength of candidate repair materials. A numerical model of the laboratory testing of damaged wellbore specimens was developed. This investigation found that microannulus permeability can satisfactorily be described by a joint model. Finally, a wellbore model has been developed that can be used to evaluate the response of the wellbore system (casing, cement, and microannulus), including the use of either cement or a nanocomposite in the microannulus to represent a repaired system. This wellbore model was successfully coupled with a field-scale model of CO_2 injection, to enable predictions of stress and strains in the wellbore subjected to subsurface changes (i.e. domal uplift) associated with fluid injection.

Contents

EXECUTIVE SUMMARY

The overall goal of the project was to develop and test new materials to repair flaws (voids, fractures, degraded interfaces) in seal systems in wellbores that penetrate formations used for geologic storage of CO_2. Our approach was to modify polymer cements with various nanomaterials to produce polymer nanocomposites that have superior seal repair characteristics compared with conventional materials, particularly for sealing the cement-casing interface. The project had two main efforts: materials development and wellbore system testing. In addition, modeling efforts were undertaken to support the project and provide a means to extend the project outcomes to field applications. These activities are summarized below.

Materials development

Candidate repair materials were synthesized from combinations of 3 different types of base polymers and 4 different nanoparticles. Base polymers were styrene-butadiene rubber (SBR) polymer latex, low modulus polysulfide-siloxane epoxy and novolac epoxy; candidate nanomaterials were carbon nanotubes (CNTs), nanoclay, nanosilica and nanoalumina (ANP) particles. A total of 26 formulations were prepared and tested, along with a type G cement which served as the reference material.

We down-selected candidate materials based on flowability and bond strength testing using slant shear tests. Slant shear tests were also used to obtain stress-strain behavior. We found that all nanocomposites were superior to microfine cement in terms of bond strength and had acceptable flowability. Novolac epoxy combined with CNTs or ANPsparticles produced nanocomposites with the best properties. Additional microscale tests were conducted to characterize the nanocomposite repair material. One important result from these tests was that incorporating ANPs decreasing polymer crosslinking and yields a more flexible material compared with neat epoxy.

Push-out tests were used to investigate the bond strength of shale-cement interfaces that had been repaired with different repair materials. Microphotographs showed the existence of microcracks at the cement-shale interface repaired with microfine cement, whereas repair with Novolac epoxy with and without ANPs showed no gaps. The penetration of the epoxy nanocomposite repair material not only improves the shale-cement bond strength, but it also seals leakage pathways adjacent to the interface and thus improves wellbore seal integrity.

The ability of repair materials to fill microcracks was investigated by injecting material into smooth-walled cracks with widths of 13, 25, 50, 75, and 100 microns formed between transparent plexiglass sheets. Novolac epoxy and Novolac epoxy with 2% ANPs were able to 100% fill the crack width of 13 microns, whereas microfine cement did not penetrate cracks smaller than 50 microns and had incomplete filling of larger cracks.

Integrated wellbore system testing

We have developed an experimental system to test wellbore specimens comprised of a cement sheath cast on a steel casing. The system allows independent application of confining pressures to 35 MPa and casing pressures to 20 MPa while gas flow is measured through the specimens along the wellbore axis at pore pressures up to 15 MPa. Wellbore specimens were created with various flaws, including cement fractures and microannuli between the steel casing and the cement. Thermal transients induced by cooling and heating the casing were used to produce flaws in the wellbore samples, consistent with wellbore damage from field operations that arises from temperature changes within a casing. We interpreted the hydraulic aperture of

the flaws from gas flow measurements. The size (hydraulic aperture) of the microannuli ranged from less than 10 μm to more than 100 μm. This range appears to be on the order of the size of wellbore flaws implied from limited field measurements and observations of leaky wellbores.

Testing damaged wellbore samples revealed that flaws are capable of transmitting large flows. The flow rate through samples with microannuli is approximately 10^3 to 10^5 times the flow rate of intact wellbore cement. We also found that samples created with a corroded casing were comparable samples that had been thermally de-bonded.

We repaired a number of the flawed wellbore specimens. Repair with the nanocomposite epoxy base material was successful in reducing the flow through flaws of various sizes and types to that equivalent to an intact cement. The repair remained effective after cycling the confining stress. In contrast, repair of flawed samples with microfine cement was initially less effective. In addition, the hydraulic aperture of the cement repaired sample increased with cycles of confining stress, indicating that the microfine cement repair was degrading. After repair and testing, we sliced samples to allow for observations of the repair effectiveness. The nanocomposite epoxy base material appeared to fill all voids along the microannulus; in contrast, the microfine cement clearly did not.

Modeling studies

Finite element (FE) analyses of the slant shear test configuration were conducted using ABAQUS modeling software. Our objective was to use the validated FE model to realize the local shear stresses developed at failure of the slant shear test. The results indicate that while incorporating nanoparticles in Polymer Cement (PC) resulted in increasing the bond strength of PC to steel substrates, this improvement in bond strength when measured in terms of maximum local shear stresses is less significant than that measured using the apparent shear strength. Our simulations also confirmed the role of stiffness on stress development at the interface. It is apparent that improving wellbore integrity might not be accomplished through using materials with improved bond strength only, but also by engineering materials with specific stiffness that would minimize shear stresses under thermal and pressure gradients.

Numerical models were also developed of the laboratory integrated wellbore system test configuration, and included modeling flaws of varying dimensions along the casing-cement interface. A joint model was used to describe the hydraulic aperture of the microannulus region, where the mechanical stiffness is altered in response to the imposed stress state across the joint interface. The aperture-stress behavior is based upon laboratory measurements of hydraulic aperture as a function of imposed stress conditions. This investigation found that the microannulus elements reasonably reproduce laboratory behavior during loading from confining pressure increases. The calculated microannulus response to internal casing pressure changes was less stiff than measured, which may be due to hardening of the microannulus during testing.

Modeling of field scale wellbore systems involved two distinct steps. First, a field scale model was developed that uses the stratigraphy, material properties, and injection history from a pilot CO_2 injection operation to develop stress-strain histories for wellbore locations from 100 to 400 meters from an injection well. The results from these models are used as input to a more detailed model of a wellbore system. Two separate wellbore-scale models have been developed during this study. The first model includes steel casing(s); cement surrounding the casing(s); and formation rock around everything, and was designed to evaluate the stresses induced on casing materials under shear loading. The second wellbore model contains a similar steel casing and cement or nanocomposite annulus representation for an entire length of borehole that matched the 100-m-spaced borehole columns of the field-scale model.

INTRODUCTION

1.1 Project goals

The overall goal of the project was to develop and test new materials to repair flaws (voids, fractures, degraded interfaces) in seal systems in wellbores that penetrate formations used for the sequestration of CO_2. Polymers were modified with various nanomaterials to produce nanocomposites that have superior seal repair characteristics compared to conventional materials, particularly for sealing the cement-casing interface.

Specific goals are (1) develop seal repair materials suitable for the expected wellbore environments that have acceptable viscosity and pot life, high bond strength to casing and cement, low permeability, high ductility and fracture toughness (resistance to crack growth), and (2) evaluate the effectiveness of these materials to repair flaws in large, lab-scale annular seal systems (5 cm diameter steel casing set inside a sheath of cement) that are subjected to conditions expected for CO_2 storage conditions. The outcome of this study is the development of nanocomposite materials that have specific properties tailored for repairing wellbores associated with CO_2 storage, and an evaluation and understanding of the expected performance of these materials to repair flaws within sealed wellbores, focusing on the region surrounding the interface between the casing and the cement.

1.2 Project motivation

The seal integrity of abandoned wellbores is central to ensuring permanent storage of CO_2 in geologic formations. A wellbore that intersects the storage formation represents a potential leakage pathway that can lead to subsurface migration of stored CO_2 and/or subsequent venting of stored CO_2 to the surface. In terms of potential risk for leakage, wells can be broadly divided into 3 categories: 1) future wells, 2) low leakage-risk abandoned wells, and 3) high leakage-risk abandoned wells. Both geographic location and time period of abandonment -- and practices and regulations, if any, in place at the time of abandonment -- have a significant impact on whether or not an abandoned well falls into the low leakage-risk or high leakage-risk category (Watson

and Bachu 2008). Both future wells and low leakage risk abandoned wells are of lower priority with respect to preventing leakage, as best practices for well completion and abandonment implemented can greatly reduce the occurrence of factors that increase the risk of wellbore leakage (IEAGHG 2009, NETL 2011).

Since there can be thousands of wells that intersect a subsurface formation used for CO_2 storage, it can be expected that an appreciable fraction of such wells were likely drilled/completed/abandoned before current best practices were put into practice. Such wells represent an increased risk for leakage, and it is likely that at a typical storage operation, reworking or recompleting leaky or high risk of leakage wells will be an important part of ensuring permanent storage.

Well repair, as opposed to re-completion, may be both economically and technically preferable in certain contexts. Since there is heterogeneity of failure modes that can be specific to a particular well (or group of wells), a portfolio of repair techniques/options may be best suited to ensuring seal integrity in a cost effective manner. Conventional repair technology involves "squeezing" cement into the annulus. Penetration into the microannulus and small cracks can be problematic with conventional cements. Microfine cement is intended to increase penetration, however, the fundamental problem of adhesion versus cohesion bond failure of cement and steel casing in the downhole environment is not addressed by most, if not all, current repair materials. Adhesion failure is characteristically brittle and unpredictable -- classical cement-steel failure is a typical adhesion failure. When special cements that form a strong bond to steel are used, partial cohesion failure may occur. The very low fracture toughness of cement plays a significant role in cohesion failure.

The shortcomings of conventional repair materials may be overcome by the use of polymer based nanocomposite materials. The use of polymer cement repair materials prevents adhesion failure, and enables cohesion failure to govern. Tailoring the polymer properties with nanomaterials will allow us to control cohesion failure by means of improving ductility (strain to failure) and fracture toughness of polymer-cement nanocomposites. Some polymers have previously been used for annulus seal repair in large part due to their high flowability, however, their long-term performance in the environment expected for CO_2 wellbores has not been demonstrated. In particular, these materials have not been designed to have the long-term bond

characteristics and ductility required for these applications. Further, modifying and optimizing properties for repair application with nanoparticles has not been previously reported.

1.3 Report organization

The project goals and motivation are provided in the introduction provided in Chapter 1. The development and testing of the nanocomposite materials are given in Chapter 2. Chapter 3 contains the integrated seal system testing description and results. Modeling studies that supported the project are given in Chapter 4. Finally, conclusions and accomplishments are described in Chapter 5. Appendix A contains a cost analysis of the use of nanoparticles in wellbore repair applications.

2. Material Development and Characterization

2.1. Development of Polymer Nanocomposites

2.1.1. Materials

Three group of materials are used in this experimental investigation. First: Type G cement typically used in oil well operation, Second: three types of polymers including Styrene-butadiene rubber (SBR) polymer latex, low modulus polysulfide-siloxane epoxy and novolac epoxy. Third: four types of nanomaterials including: carbon nanotubes (CNTs), nanoclay, nanosilica and nanoalumina particles. Combinations of the above materials were used to produce a reference material in addition to fourteen polymer/cement nanocomposites. Five materials are selected out from as the top performing materials from all the fifteen polymer nanocomposites tested. The section below provides information of the materials used.

1. Cement

Type G (API Class G) oil well cement (OWC) was used as the reference cement material. This material was acquired from the manufacturer and is obtained by grinding clinker, consisting essentially of hydraulic calcium silicates, usually containing one or more forms of calcium sulfate as additive. Class G OWC is intended for use as a basic well cement and is available in moderate sulfate-resistant (MSR) and high sulfate-resistant (HSR) grades. Type G OWC is known for its flowability and high fineness. It is well known that type G cement is very comparable to ASTM Class II and Class V cements. The water/cement ratio for mixing Type G cement is 0.45.

2. Polymers

Three types of polymers have been used. The first polymer used is Styrene-Butadiene Rubber (SBR) polymer latex incorporating styrene, butadiene, A vinyl carboxylic acid, surfactant (nonionic and anionic), and water. The content of SBR in SBR/cement composite was guided by recommendations of the American Concrete Institute (ACI) for producing polymer concrete. The second polymer used is polysulfide epoxy including silane. This epoxy is usually used as an overlay material for repair of bridge decks. The epoxy consists of two components, epoxy resin and epoxy hardener. The resin is mixture of Bisphenol A/Epichlorohydrin Epoxy Resin

including silane. The hardener is Diethylenetriamine (DETA), Phenol, 4,4'-(1-methylethylidene)bis-, and Tetraethyllenepentamine. The third polymer used is Novolac epoxy. Novolac epoxy resins are specifically designed to provide high thermal stability and chemical resistance. This is accomplished by switching from Bisphenol A to Novolac backbones.

3. Fillers

In all mixes crystalline silica (quartz) and ceramic microspheres powder was used as mixing filler to produce the slurry to be cast and harden.

4. Nanomaterials

A group of four nanomaterials have been tested so far. This includes Multiwall carbon nanotubes (MWCNTs), Nanoclay, Nanosilica and Nanoalumina particles. The selection of the nanomaterials content was based on prior work by the research team

4.1. Multi-walled Carbon Nanotubes (MWCNTs)

Functionalized Multi-Walled Carbon Nano-Tubes (MWCNTs) were added to produce the nanocomposite. The MWCNTs are functionalized with carboxyl (COOH) groups produced using Catalysed Chemical Vapor Deposition (CCVD) technique.

4.2. Non-Functionalized Multi-walled Carbon Nanotubes (NF-MWCNTs)

Non-Functionalized Multi-Walled Carbon Nano-Tubes (MWCNTs) with similar properties to functionalized MWCNTs except the absence of the COOH functionalized group.

4.3. Graphene Nanoparticles (GNP)

Functionalized Graphene Nano particles (GNP) will be used to produce polymer nanocomposites. GNP are are functionalized with carboxyl (COOH) groups and were produced using Catalysed Chemical Vapor Deposition (CCVD) technique.

4.4. Nanosilica

The nanosilica used is AEREOSIL® 380 from manufacturer Evonik Degussa Products, which is hydrophilic fumed silica with an average BET surface area of 380 m²/g and an average particle diameter of 7 nm. AEROSIL® 380 is a chemically prepared silicon dioxide powder that is white in color and odorless, and has a melting point of 1700℃ and a density of 2.2 g/cm^3.

4.5. Nanoclay

The nanoclay used in this research is Cloisite®30B supplied by Southern Clay Products, Inc. It is an off white material consists of natural montmorillonite modified with a quaternary ammonium salt. The nanoclay consists of dry particle sizes with 10%, 50%, and 90% by volume less than 2 μ, 6 μ, and 13 μ, respectively.

4.6. Nanoalumina

The nanoalumina used is aluminium oxide (Al_2O_3) nano particles manufactured by Sigma Aldrich, Inc. and has a maximum particle size of 50 nm.

Table-2.1 presents the matrix of all polymer-cement nanocomposites synthesized and tested over the project time period. The materials tested are described in **Table-2.1**.

Table 2.1: Polymer/cement nanocomposite (*PCNC**) repair material synthesized and tested

#	Material	Base material	nanomaterial	Nano content%
1	Reference	Microfine cement	None	---
2	PCNC1	Microfine cement + 5%SBR latex	None	---
3	PCNC2	Microfine cement + 15%SBR latex	None	---
4	PCNC3	Microfine cement + 5%SBR latex	MWCNTs	0.5%
5	PCNC4	Polysulfide siloxane epoxy	None	---
6	PCNC5	Polysulfide siloxane epoxy	MWCNTs	0.5%
7	PCNC6	Polysulfide siloxane epoxy	MWCNTs	1.0%
8	PCNC7	Polysulfide siloxane epoxy	MWCNTs	1.5%
9	PCNC8	Polysulfide siloxane epoxy	Nanoclay	4%
10	PCNC9	Polysulfide siloxane epoxy	Nanosilica	1%

11	PCNC10	Polysulfide siloxane epoxy	Nanoalumina	2%
12	PCNC11	Novolac epoxy	None	---
13	PCNC12	Novolac epoxy	MWCNTs	0.5%
14	PCNC13	Novolac epoxy	Nanosilica	1%
15	PCNC14	Novolac epoxy	Nanoalumina	2%
16	PCNC15	Polysulfide siloxane epoxy	NF-MWCNTs	0.5%
17	PCNC16	Novolac epoxy	MWCNTs	1.0%
18	PCNC17	Novolac epoxy	MWCNTs	1.5%
19	PCNC18	Novolac epoxy	Nanoclay	4%
20	PCNC19	Novolac epoxy	Nanoalumina	0.5%
21	PCNC20	Novolac epoxy	Nanoalumina	1.0%
22	PCNC21	Novolac epoxy	MWCNTs	2%
23	PCNC22	Novolac epoxy	Nanosilica	0.5%
24	PCNC23	Novolac epoxy	Nanosilica	2.0%
25	PCNC24	Novolac epoxy	Nanoalumina	1.5%
26	PCNC25	Novolac epoxy	Nanoalumina	3.0%
27	PCNC26	Novolac epoxy	Nanoalumina	4.0%

**** PCNC: Acronym used for polymer-cement nanocomposite***

5. Polymer/cement nanocomposites

Material characterization included testing the flowability and bond-strength with steel overlay. In order to investigate the effect of incorporating CNTs in the repair material, four polymer nanocomposite slurry mixtures were prepared. The word slurry is used as our polymer nanocomposite mixes include crystalline silica and ceramic microspheres powder as mixing filler. Such fillers are important to reduce shrinkage and produce realistic repair material. The first cement mortar mix is reference mix (cement, filler, and water). The SBR latex/cement mortar mixes included 5 % and 15% polymer latex of the cement weight with no nano particles. One mix included 0.5% CNTs with 5% SBR and cement after Soliman et al. (2012a). **Table-2.2** presents the SBR-cement nanocomposite mixes including the reference mix by weight. The epoxy material slurries were produced with and without nanomaterials. Three contents of MWCNTs were used including 0.5, 1.0, 1.5% CNTs added by weight of the epoxy resin after

Soliman et al. (2012b). **Table-2.3** presents the mix proportions for all polysulfide siloxane epoxy nanocomposites. **Table-2.4** presents the mix proportions for all Novolac epoxy nanocomposites.

Table-2.2 Mix proportions for polymer/cement nanocomposite mixtures by weight kg/m^3 (lb/ft^3)

Mix designation	Cement	Filler	Water	Latex	Nanomaterial
Reference	530 (33.1)	1457.5 (91)	217.4 (13.6)	0.0 (0.0)	0.0 (0.00)
PCNC1	530 (33.1)	1457.5 (91)	177.6 (11.1)	79.5 (4.9)	0.0 (0.00)
PCNC2	530 (33.1)	1457.5 (91)	204.8 (12.8)	25.9 (1.6)	0.0 (0.00)
PCNC3	530 (33.1)	1457.5 (91)	204.8 (12.8)	25.9 (1.6)	0.129 (0.008)

Table 2.3 - Mix proportions for polysufide siloxane epoxy nanocomposites kg/m^3 (lb/ft^3).

Mix designation	Resin	Hardener	Filler	Nanomaterials	Nano content%
PCNC4	288 (18)	128 (8)	1570 (98)	None	0.0 (0.00)
PCNC5	288 (18)	128 (8)	1570 (98)	MWCNTs	1.44 (0.09)
PCNC6	288 (18)	128 (8)	1570 (98)	MWCNTs	2.88 (0.18)
PCNC7	288 (18)	128 (8)	1570 (98)	MWCNTs	4.32 (0.27)
PCNC8	288 (18)	128 (8)	1570 (98)	Nanoclay	11.52 (0.72)
PCNC9	288 (18)	128 (8)	1570 (98)	Nanosilica	2.88 (0.18)
PCNC10	288 (18)	128 (8)	1570 (98)	Nanoalumina	5.76 (0.36)
PCNC15	288 (18)	128 (8)	1570 (98)	NF-MWCNTs	1.44 (0.09)

Table-2.4 Mix proportions for Novolac epoxy nanocomposites kg/m^3 (lb/ft^3).

Mix designation	Resin	Hardener	Filler	Nanomaterials	Nano content%
PCNC11	288 (18)	128 (8)	1570 (98)	None	0.0 (0.00)
PCNC12	288 (18)	128 (8)	1570 (98)	MWCNTs	1.44 (0.09)
PCNC13	288 (18)	128 (8)	1570 (98)	Nanosilica	2.88 (0.18)
PCNC14	288 (18)	128 (8)	1570 (98)	Nanoalumina	5.76 (0.36)
PCNC16	288 (18)	128 (8)	1570 (98)	MWCNTs	2.88 (0.18)
PCNC17	288 (18)	128 (8)	1570 (98)	MWCNTs	4.32 (0.27)
PCNC18	288 (18)	128 (8)	1570 (98)	Nanoclay	11.52 (0.72)
PCNC19	288 (18)	128 (8)	1570 (98)	Nanoalumina	1.44 (0.09)

PCNC20	288 (18)	128 (8)	1570 (98)	Nanoalumina	2.88 (0.18)
PCNC21	288 (18)	128 (8)	1570 (98)	MWCNTs	5.76 (0.36)
PCNC22	288 (18)	128 (8)	1570 (98)	Nanosilica	1.44 (0.09)
PCNC23	288 (18)	128 (8)	1570 (98)	Nanosilica	5.76 (0.36)

6. Polymer nanocomposites (PNC)

Material characterization included testing the viscosity and the ability of polymer nanocomposites to seal cement-rock (shale) microannulus. Eleven materials including nine polymer nanocomposites were examined. The polymer nanocomposite is a mix of polymer and nanomaterials without any filler. **Table-2.5** presents the polymer nanocomposites used in the viscosity measurements. We note that we numbered the PNCs the same number used for the PCNC to enable simple reference to the original mixtures presented in **Table-2.1**. **Table-2.5** also presents corresponding reference to **Table-2.1**.

Table-2.5: Polymer nanocomposite (*PNC**) repair material synthesized and tested

#	Material	Base material	nanomaterial	Nano content%	Corresponding PC
1	Reference	Type G cement	None	---	Reference
2	MF	Microfine Cement	None	---	N/A
3	PNC4	Siloxane epoxy	None	---	PCNC4
4	PNC11	Novolac epoxy	None	---	PCNC 11
5	PNC13	Novolac epoxy	Nanosilica	1.0%	PCNC13
6	PNC14	Novolac epoxy	Nanoalumina	2.0%	PCNC14
7	PNC15	Siloxane epoxy	NF-MWCNTs	0.5%	PCNC15
8	PNC16	Novolac epoxy	MWCNTs	1.0%	PCNC16
9	PNC19	Novolac epoxy	Nanoalumina	0.5%	PCNC19
10	PNC20	Novolac epoxy	Nanoalumina	1.0%	PCNC20

11	PNC27	Siloxane epoxy	NF-MWCNTs	2.0%	N/A

**** PNC: Acronym used for polymer nanocomposite***

2.1.2. Mixing Methods

1. Procedure for mixing reference cement mixture

A customized combination of ASTM and API standards were used to produce the hydraulic OWC specimens [ASTM C305 (2005) and API, 2009]. This modified method produced the best cement samples during trial batching therefore it was further implemented. This procedure included Mixing of all dry materials at a rate of 140 ± 5 r/min for 30 seconds to incorporate cement and nanosilica together where applicable. We then placed the mix water to the bottom of a clean mixing bowl and added the dry materials to the mix water and allowing 30 seconds for absorption. The combination was mixed for 30 seconds at a rate of 140 ± 5 r/min. The mixer was stopped for 15 seconds while scraping down the sides of the bowl. Finally, the mix was mixed together for 1 minute at a speed of 285 ± 5 r/min until the slurry is formed. The required aggregate was then added and mixing continued for 2-3 additional minutes until the mixture looked uniform.

2. Procedure for synthesis and mixing of polymer nanocompsite

For the neat polymer, the required amount of resin and hardener were mixed together for 2-3 minutes using a low speed mixer, after which silica filling powder followed by the required coarse aggregate were added. Mixing continued for 2-3 minutes until the mixture was uniform. For the nanocomposite mix, the nanoparticles (e.g. MWCNTs) were added to the required amount of the resin, the mix was stirred for 2 hours at 110 ^{o}C using magnetic stirring. This relatively high mixing temperature was used to reduce the resin viscosity and improve the dispersion of MWCNTs. The mix was then sonicated for 2 additional hours at 65 ^{o}C. During the sonication, sound waves are generated from the transducer and radiate through the liquid causing high and low pressures. At the low pressure stage, millions of microscopic bubbles are formed; during the high pressure stage, the previous bubbles collapse releasing high amount of energy and improving the dispersion of the nanoparticles. **Fig. 2.1** shows the mechanical stirring and sonication process for the polymer nanocomposite. The polymer resin nanocomposite was left to

reach room temperature and then mixed with the hardener for 2-3 minutes. The required aggregate was then added and mixing continued for 2-3 additional minutes until the mixture looked uniform.

Fig.2.1: Mixing of polymer nanocomposite (left) mechanical stirring (right) sonication.

2.2. Characterization of Polymer Nanocomposites

2.2.1. Flowability of polymer cement nanocomposites

The first test was the flowability test which was performed to judge the effect of adding CNTs on the flowability of the polymer nanocomposite. The flowability test was performed according to ASTM C1437 (2007). Flow table, flow cone, and test caliper were used. The cone smaller diameter was 70 mm (2.8 in), larger diameter was 100 mm (4.0 in), and the height was 50 mm (2.0 in). Each mix was prepared and the cone was filled by fresh mix in two layers. Each layer was tamped 20 times to ensure uniform filling of the cone. The cone was then lifted in 4 seconds and 25 strikes were applied to the fresh specimen in 15 seconds. Following the measurement of the initial diameter, 25 strikes of the flow table were applied and four perpendicular readings were taken by the test caliper. The flowability is represented by the percentage change in the initial diameter due to slump flow and the final diameter after applying the 25 strikes of the flow table. The average percent change of the four diameters was used to describe the material flowability. **Fig. 2.2** shows the procedure of filling the cone and using the caliper for measurements.

Fig.2.2: Filling the flowability cone (left), and measuring caliper (right).

2.2.2. Examining polymer nanocomposite bond to steel substrates

The second test was the pull-off test to measure the bond strength between the polymer nanocomposite slurry and a steel plate. The test method is reported in a previous quarterly report (Year 1, Quarter 1 report). Failure modes of the pull-off test according to ASTM C1583, [2013] indicated that the test was measuring the cohesion strength of polymer nanocomposite more than bond strength between polymer overlay and steel. Therefore, it was decided to test the bond of the polymer nanocomposite overlay with steel using standard slant shear test following ASTM C882 [2013]. The slant shear test specimen consists of composite cylinders of steel and polymer nanocomposite overlay. The composite cylinders have diameter of 50 mm (2.0 in) and height of 100 mm (4.0 in). The bond line between the two halves of steel and polymer nanocomposite overlay was inclined by 60° with the horizontal. Composite cylinders were tested in compression until failure and load and displacement were recorded. **Fig.2.3** shows a schematic of the slant shear test. Five cylinder halves were cut from 50 x 100 mm (2.0 x 4.0 in). steel rod and sandblasted to a minimum of 4.0 Mil clean surface roughness profile in order to cast cement/polymer nanocomposite overlay on it. **Fig.2.4** shows the dimensions used to produce the steel part of the composite cylinders and a sandblasted steel part.

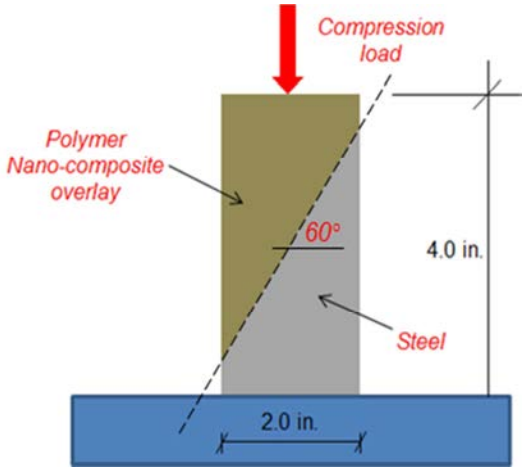

Fig.2.3: Schematic of slant shear test set-up (1 in = 25.4 mm).

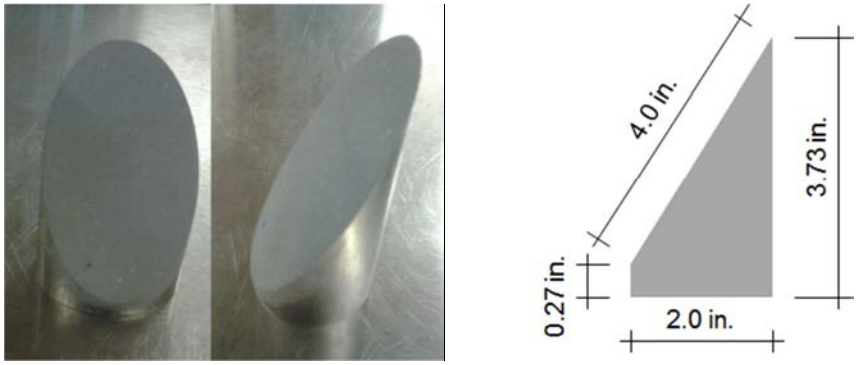

(a) (b)

Fig.2.4: Dimension of slant shear test (a) steel part (b) sandblasted steel halves (1 in = 25.4 mm).

Fig.2.5 shows a slant shear specimen after curing and demolding while ready for slant shear testing. For cement specimens, they were left to cure under water as recommended in the literature. For polymer/cement specimens, they were left to cure under water for 48 hours then left to cure in air under room temperature and 50% relative humidity. For all other polymer nanocomposites, the specimens were demoulded then left to cure to cure in air under room temperature and 50% relative humidity until 7 days of age. The slant shear test was conducted under displacement control protocol with a rate of 0.0356 mm/sec in order to save the steel parts of composite cylinders. Test load and displacement were recorded using a rate of 10 Hz. **Fig.2.6** shows the slant shear test setup and the damage occurred in the first trial specimen.

Fig.2.5: Composite cylinder of neat polymer overlay on steel

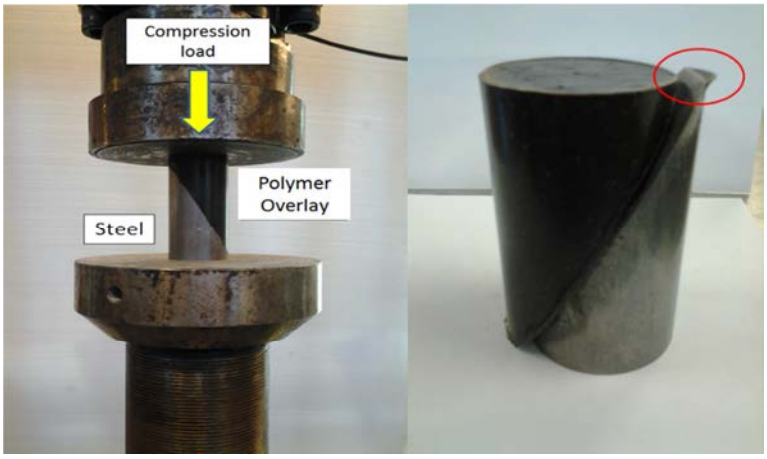

(a) (b)

Fig.2.6: (a) Slant Shear test setup, (b) damage in the steel part of the first trial specimen.

2.2.3. Microstructure characterization polymer nanocomposite-steel interface

The third test was Fourier Transform Infrared spectroscopy (FTIR). 25.4 mm x 25.4 mm steel samples coated with different polymer-cement nano composites and were analyzed using FTIR. All the samples were analyzed with biconical reflectance Nicolet Nexus 670 Micro-Fourier Transform Infrared Spectroscopy (Micro-FTIR). The FTIR has a continuum microscope with a Globar source, XT-KBr beam splitter and a MCT-A detector over a 100x100 micron area with a 4-cm-1 resolution. Spectra were background corrected using a reflective gold slide and converted to absorbance using the Kramers-Kronig equation as per standard FTIR analysis method. The objective of the FTIR method is to identify potential chemical reactions of the

nanomaterials with the polymer used forming polymer-nanomaterial-nanocomposite. Comparison between the spectrums of the original hardened polymer versus that of the hardened polymer nanocomposite shall enable us to identify if chemical reaction of the polymer and nanomaterial takes place. Furthermore, comparison of the steel plate without any coating on it versus steel with polymer shall confirm to us if chemical bond between steel and the polymer or the polymer nanocomposite took place. FTIR analysis is therefore essential to identify the role of nanomaterials in improving bond and toughness of the polymer nanocomposites.

The fourth test was X-ray photoelectron spectroscopy (XPS). 10mm x 10 mm steel samples coated with different polymer-cement nano composites were used for XPS. The high temperature catalyst reaction cell (WX-530) allows for in-situ analysis of high temperature (up to 1000 ^{o}C) catalytic reactions. Systems were investigated in the reaction cell and then transferred under UHV directly into the XPS analysis chamber thus avoiding contamination. Reactant gases such as H_2, O_2, H_2O, CO_2, CH_4 are delivered from a series of fine control needle valves into the reaction vessel via the gas entry capillary. This capillary delivers a supply of gas, which is heated to the reaction temperature as it enters the vessel. Heating/cooling stage allows temperature controlled experiments such as analysis of phase transitions or degradations studies in the range of T from -150 C° to +600 C°. The objective of XPS measurements is to identify the binding energy between the polymer/cement nanocomposite used and the steel substrate. XPS provides a measure of the binding energy. Changes in binding energy indicate strong bond to take place.

2.2.4. Extracting stress-strain relationship of polymer cement nanocomposite

The fifth test was performed to extract the stress-strain constitutive relationship of Novolac PCNCs. The selected materials include PCNC 11 (Neat Novolac), PCNC 12 (Novolac with 0.5% MWCNTs), PCNC 13 (Novolac with 1% nanosilica) and PCNC14(with 2% Nanoalumina). The tests were conducted according to ASTM C39/C39M14A. The four Novolac PCNCs were selected for being the best performing materials in slant shear testing. The test was performed under displacement control with a displacement rate of 0.02 in/min. Test samples were cast using (2 in x 4 in). The test also identifying the compressive strength, modulus of elasticity and Poisson's ratio of selected PCNCs. **Equations (2.1) and (2.2)** were used to calculate the modulus of elasticity and Poisson's ratio. These equations were obtained according to ASTM

C469/C469M [2014] while changing the strain from 0.00005 to 0.0005 to account for the use of polymeric concrete. The stress-strain curves were then used in finite element analysis. Three strain gages were placed on each specimen with two measuring vertical strain and one measuring horizontal strain as shown in **Fig.2.7**. All tests were carried with similar conditions to slant shear specimen in regards to curing, sizing and testing at 7-day age of concrete. **Fig. 2.8** shows the test setup for the scaled slant shear specimen.

$$Modulus\ of\ Elasticty = E = \frac{Stress}{Strain} = \frac{\sigma_{40} - \sigma_{0.0005}}{\varepsilon_{40} - \varepsilon_{0.0005}} \qquad \textbf{(2.1)}$$

$$Poisson's\ ratio = \rho = \frac{Vertical\ strain}{Horizontal\ strain} = \frac{(\varepsilon_{y_{40}})}{(\varepsilon_{40})} \qquad \textbf{(2.2)}$$

Where, σ_{40} is the stress corresponding to 40% of ultimate strength, ε_{40} is the longitudinal strain corresponding to σ_{40}, $\sigma_{0.0005}$ is the stress corresponding to longitudinal strain of 0.0005, ε_{y40} is the transverse strain corresponding to σ_{40} and $\sigma_{y0.0005}$ is the stress corresponding to strain of 0.0005. To investigate the effect of the curing conditions on bond development, scaled slant shear specimen with diameter of 25 mm (1 in) and height of 50 mm (2 in) were prepared as shown in **Fig. 2.9**. The high temperature and pressure conditions were only performed on Novolac being the best performing PCNCs in full scale slant shear testing. PCNC11 (neat Novolac), PCNC14 (Novolac with 2% Nanoalumina), and PCNC17 (Novolac with 1.5% MWCNTs) were used to examine the significance of elevated temperature curing on high performing PCNCs with and without nanomaterials. Six slant shear specimen were prepared following the same procedure used for the large scale slant shear specimen mentioned earlier in this section. After 24 hours, the slant shear specimens were demoulded. Three specimens were air cured and normal environmental condition (room temperature and atmospheric pressure). The other three specimens were cured under high temperature of 80 °C and pressure of 10 MPa (1500 psi) for 6 days. The high temperature and pressure curing was achieved using 450 ml Parr® pressure vessel following a set-up established by the PIs for testing OWC (Kim et al. 2013). 300 ml of water filled the vessel and specimens were cured in the water under elevated temperature and pressure. Using the heater surrounding the vessel, temperature was elevated and kept constant during the curing time period. To prevent temperature fluctuations in the vessel, a controller was used to maintain constant temperature. Pressure was applied by injecting nitrogen

gas from a compressed Nitrogen cylinder at 10 MPa. The high temperature and pressure curing reactor is shown in **Fig. 2.10**. After curing, the slant shear test was conducted under displacement control protocol with a loading rate of 0.0178 mm/sec.

Fig.2.7: Horizontal and vertical strain gages.

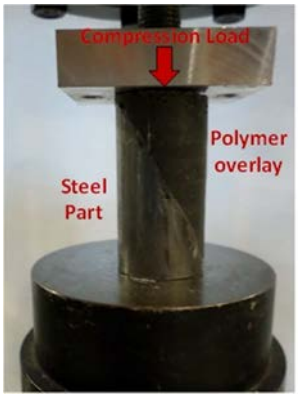

Fig.2.8: Scaled slant shear test setup.

(a)

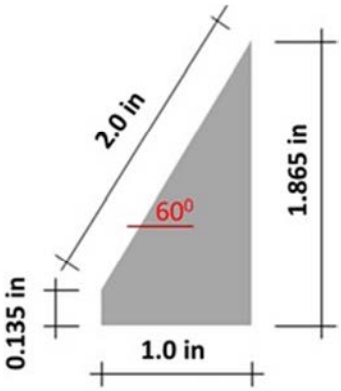

(b)

Fig.2.9: Scaled slant shear specimen (a) final specimens (b) dimensions.

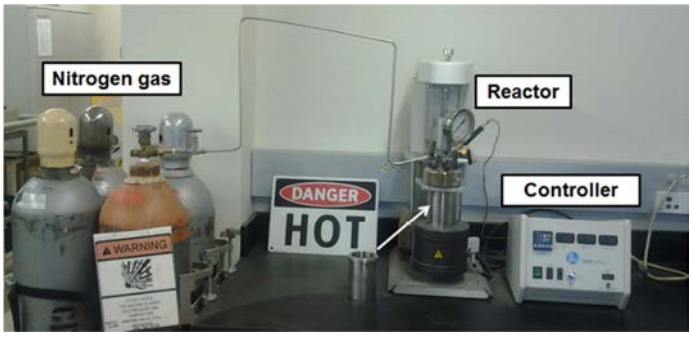

Fig.2.10: Reactor used for elevated temperature and pressure curing of PCNCs specimens

2.2.5. Examining the ability of polymer nanocomposite to seal Mancos shale-cement interface

The objective of this testing was to characterize the sealing capabilities of polymer nanocomposite to seal microannuls of Mancos shale-cement interface. The shale used in this investigation was obtained from Sandia National Laboratories. The list of polymer nanocomposites examined is presented in **Table-2.5**. In order to obtain the shale specimens, cores were drilled from the block of shale was used as shown in **Fig.2.11**. The core drill used has inner diameter of 25.4 mm (1 in) and outer diameter of 31.5 mm ($1\frac{1}{4}$ in).

Fig.2.11: Core drilling (left), and obtained shale core (right).

Push-out tests were used to investigate the bond strength of the shale with different repair materials. Two sets of specimens were prepared for push-out tests. The first set was used to measure the bond strength between the shale and the cement. Cylindrical specimens with diameter of 100 mm (4 in) and height of 50 mm (2 in) were prepared. A shale core of 25 mm (1 in) diameter and length greater than 62.5 mm (2.5 in) was fixed in the center of a plastic mold, and cement paste was then cast around the shale. The second set was prepared to investigate the bond between the repair material and the shale. Cement cylinders 100 x 50 mm (4 x 2 in) were cast with a 27 mm ($1\frac{1}{16}$ in) hole in the center. After the cement cylinder was cured, the shale core was placed in the center of the hole. Finally, the repair material was injected in the 800 μm = 0.8 mm gap between the shale and the cement. **Fig.2.12** shows a schematic of the push-out test specimens. **Fig.2.13** and **Fig.2.14** show the preparation of the push-out test specimen and push-out test specimen repaired with Novolac epoxy respectively.

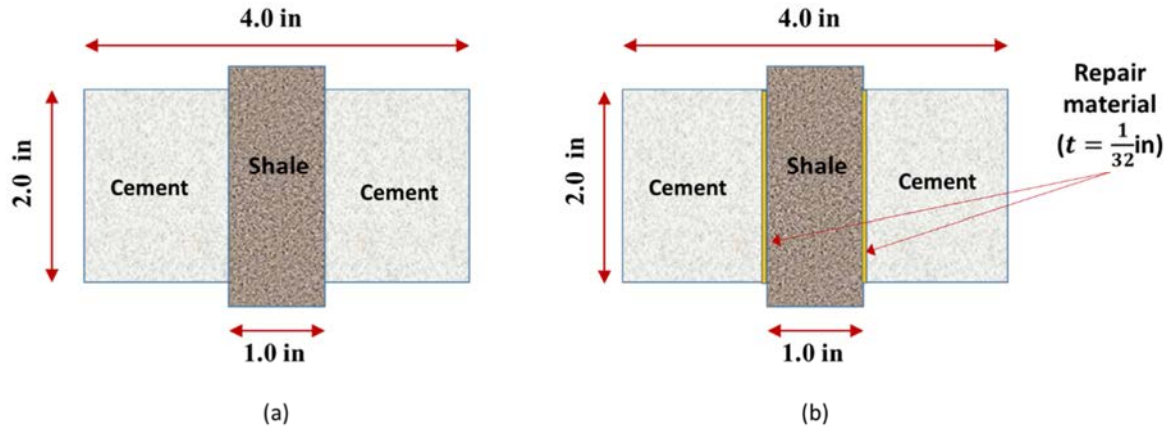

Fig.2.12: Schematic of push-out specimens (a) First set: without repair material and (b) Second set: with repair material (1 in = 25.4 mm).

Fig.2.13: Preparation of reference push-out specimen (without repair material).

Fig.2.14: Preparation of repaired push-out test specimen with Novolac epoxy.

Fig.2.15 shows a schematic of push-out test setup. **Fig.2.16** shows actual push-out setup. The push-out test was conducted under two-stage displacement control protocol. First, the test is started with a rate of 0.01 mm/min for the first 5 mm then the loading rate was increased 1.0 mm/min. Test load and displacement were recorded using a rate of 1 Hz. The change of the loading rate was attributed to enable bond failure at low strain rate. This low strain rate was not necessary to keep as friction displacement took place post the peak load. The use of higher load

rate post-peak was also necessary to enable specimen testing within reasonable time (about 1 hour).

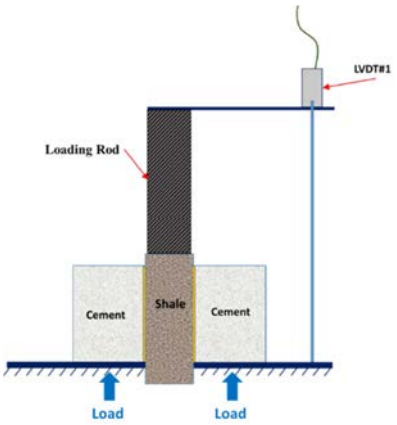

Fig.2.15: Schematic of push-out test setup showing the position of the applied load and the displacement measured by the machine.

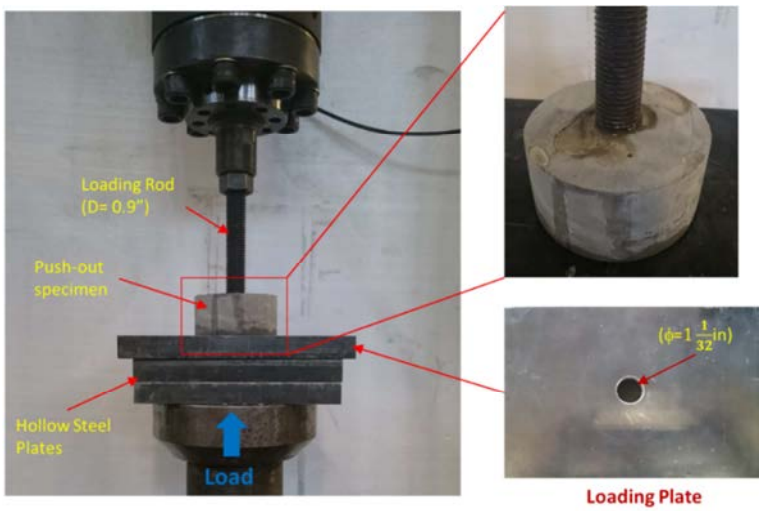

Fig.2.16: Push-out test setup.

Fig.2.17 shows the tested specimens of the first trial. Both reference and repaired specimens failed due to radial cracks in the cement cylinders not due to debonding of the shale core as expected. This failure mode is attributed to the circumferential stresses developed in the cement and the lack of confinement. In real wellbore, the cement annulus will be confined with the infinite surrounding soil. Thus, two confined sets of specimens of each reference and repaired push-out specimens were prepared. A steel pipes with outer diameter of 100 mm (4 in) and wall

thickness of 6.5 mm (0.25 in) were used in order to provide confinement of the push-out specimen. Two confined sets of specimens of each reference and repaired push-out specimens were prepared. The first set has a full embedment length of shale in the cement cylinder while the second set has a partial shale embedment length of 38 mm (1.5 in). **Fig.2.18** and **Fig.2.19** show the specimens with full embedment length and the specimens with partial embedment length respectively. The rationale behind testing two embedment lengths was to ensure bond failure rather than cement fracture at least for the shallow embedment length. It was good that both specimens showed bond failure.

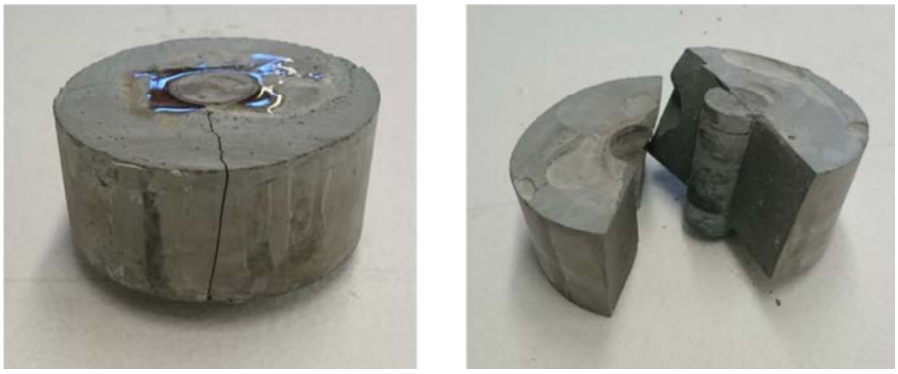

Fig.2.17: Failed specimens of the first trial test showing radial cracks of the cement due to the lack of cement confinement.

Fig.2.18: Push-out specimens with full embedment length.

Fig.2.19: Push-out specimens with partial embedment length.

2.2.6. Extracting physical characteristics of polymer nanocomposites

The effect of the nanoparticles on the glass transition temperature (T_g) of the polymers was investigated using Dynamic Mechanical Analyses (DMA) Shown on **Fig.2.20**. 20 mm x 12.5 mm x 3.0 mm specimens were tested under cyclic 3-point bending with frequency of 1 Hz and a magnitude of 0.05 N. The specimens were tested in temperature range between 40-90 ^{o}C with a temperature ramp of 3 ^{o}C/min.

Fig.2.20: Dynamic Mechanical Analyses (DMA) testing machine

Furthermore, cross-linking density determined using dynamic mechanical analysis (DMA) and the degree of chemical reactivity of the nanomaterials with the polymer matrix determined using Fourier Transform Infrared (FTIR). Viscosity test was conducted using Viscometer. The viscosity was measured for all material at room temperature (22 ºC). SC4-21 spindles rotate at a 20 rpm was used in viscosity measurements. The spindle was allowed to rotate for 1 minutes then three readings were taken at 15 seconds intervals.

Polymer crosslinking density was determined by applying the theory of rubbery elasticity using **Equation (2.3)**.

$$\upsilon_e = E`'/3RT \qquad \textbf{(2.3)}$$

υ_e is the crosslinking density, E' is storage modulus in the rubbery plateau, T is the temperature in Kelvin corresponding to the storage modulus value, and R is the Gas Constant. The rubbery plateau was considered to be at temperature 50 ºC above glass transition temperature T_g. The storage modulus at rubbery plateau was measured using DMA Q800. The molecular weight between crosslinks can be calculated using **Equation (2.4)**.

$$M_c = \rho/\upsilon_e \qquad \textbf{(2.4)}$$

where M_c is molecular weight between crosslinks and ρ is the density of the polymer nanocomposite. As the crosslinking of a polymer resin increases when the molecular weight between crosslinks decreases, a measure for the degree of crosslinking X_{link} is suggested here as an inverse for the molecular weight between crosslinks in a unit volume as in **Equation (2.5)**.

$$X_{link} = 1/M_c = \upsilon_e/\rho \qquad \textbf{(2.5)}$$

where X_{link} is a measure of the degree of crosslinking of the polymer nanocomposite.

2.2.7. Examining flow of polymer nanocomposite through microannulus

To examine the flow of polymer nanocomposites through microannulus, two tests were performed. First the cement-rock interfaces with the different repair materials were examined under light microscopes with two different levels of magnification (100X and 500X). Second, a test setup using Plexiglass sheets was used to measure the ability of the repair materials to fill micro cracks with deferent crack width. Two sheets of Plexiglas separated by the desired crack width (10-50 microns) were fixed then the repair

material was injected through the center of the top sheet. The spread distance of the repair material was then measured from the injection point and the behavior of the repair material was observed.

2.3 Test Results

2.3.1. Flowability Test Results

The flowability tests showed a significant improvement of flowability with the use of Novolac epoxy compared with all other polymer nanocomposites. Neat Novolac epoxy showed an improved flowability that is 42% higher than cement mix and very comparable to the most flowable polymer/cement mix using SBR. Addition of nanomaterials made a non-significant reduction of Novolac epoxy nanocomposite flowability. The flowability of Novolac epoxy nanocomposites were significantly higher than polysulfide siloxane epoxy nanocomposites with almost all tested nanomaterials. Summary of the flowability test results is shown in **Fig. 2.21**.

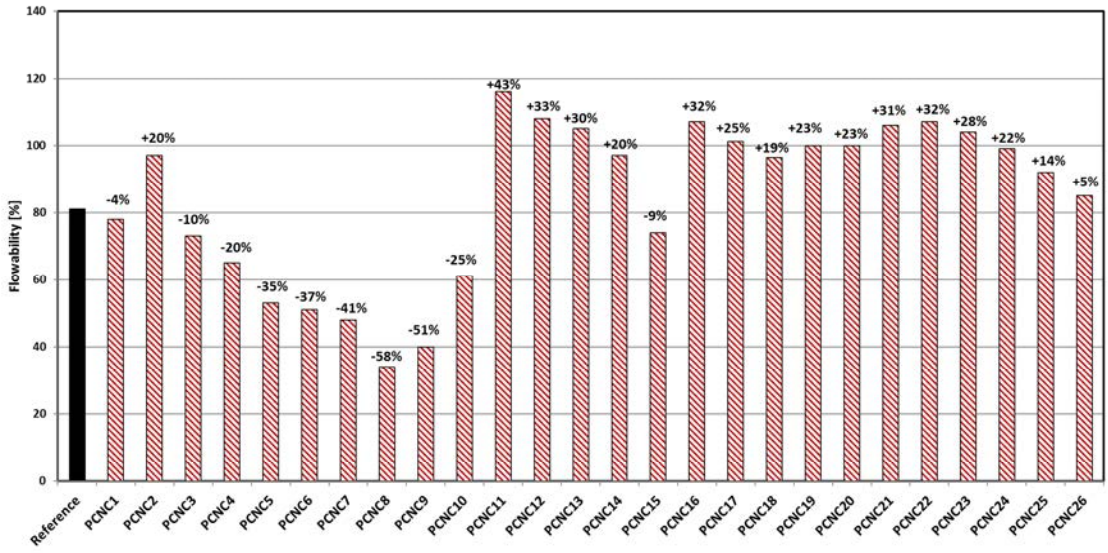

Fig.2.21: Flowability of reference cement versus all 21 tested polymer/cement nanocomposites

2.3.2. Polymer nanocomposites bond strength with steel

Example median load-displacement curves of the reference mix versus polysulfide siloxane epoxy nanocomposites incorporating 0.5% wt. MWCNTs and 0.5% wt. Non-functionalized Multi-wall Carbon Nanotubes (NF-MWCNTs) is shown in **Fig. 2.22** It is obvious that epoxy with functionalized and non-functionalized MWCNTs have a stronger bond with steel substrate much higher than the reference material and the neat epoxy. However, epoxy with NF-MWCNTs had a bond strength that is 35% higher than neat epoxy but lower than epoxy with functionalized MWCNTs which showed a bond strength that is 54% higher than neat epoxy. Statistical analysis of the bond strength test results using student t-test showed all the bond strength increases have been shown to statistically significant with 95% level of confidence. The above results showed that NF-MWCNTs do not offer any improvement in bond strength above functionalized MWCNTs. No further testing was performed using NF- MWCNTs.

Furthermore, **Fig. 2.22** shows Novolac epoxy nanocomposites incorporating 1.0% wt. Functionalized MWCNTs, 1.5% wt. Functionalized MWCNTs and 4% wt. nanoclay. It is obvious the bond strength of Novolac epoxy with steel substrate is much higher than the reference material. Epoxy with 1.5% Functionalized MWCNTs had a bond strength that is 15% higher than neat epoxy. Epoxy with nanoclay had a bond strength that is 16% higher than neat epoxy. Epoxy with 1.0% Functionalized MWCNTs had a bond strength that is 3% lower than neat epoxy. Statistical analysis of the bond strength test results using student t-test showed all the bond strength increases are statistically significant with 95% level of confidence. On the other hand, statistical analysis showed that the difference in the bond strength between the neat epoxy and the epoxy with 1.0% wt. Functionalized MWCNTs was statistically not significant.

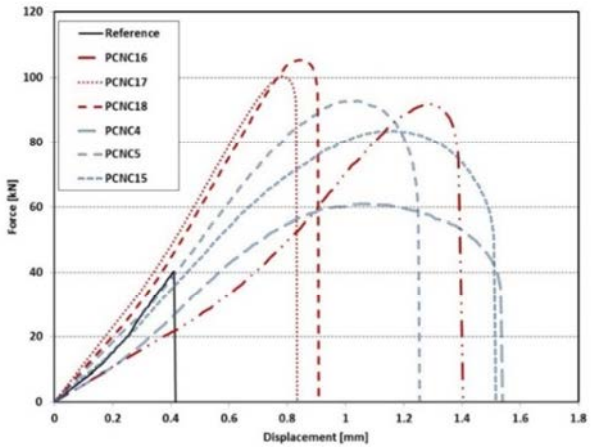

Fig. 2.22: Example median slant shear load-displacement curves of reference cement mortar (black solid curve) vs. Novolac epoxy nanocomposites incorporating PCNC16 (1.0% wt. MWCNTs), PCNC17 (1.5% wt. MWCNTs) and PCNC18 (4% wt. nanoclay) (red curves) and polysulfide siloxane epoxy nanocomposites PCNC4 (Neat), PCNC5 (0.5% wt. functionalized MWCNTs) and PCNC15 (0.5% wt. non-functionalized MWCNTs) (blue curves).

A comparison of the bond strength of the reference cement versus all 23 polymer/cement nanocomposites are shown in **Fig.2.23.** The dotted line shown represents the limit for the best five performing polymer/cement nanocomposites. The stiffness of all the 23 nanocomposites versus the reference cement mix is presented in **Fig. 2.24**. Example failure cone of the slant shear test is shown in **Fig.2.25**. Comparing the twenty one polymer/cement nanocomposites with the reference cement material, it is apparent from **Fig. 2.23** that the following polymer/cement nanocomposites have the highest bond strength compared with all other polymer/cement nanocomposites and reference cement repair material: PCNC13 (Novolac epoxy with 1% Nanosilica), PCNC14 (Novolac epoxy with 2% Nanoalumina), PCNC18 (Novolac epoxy with 4% nanoclays), PCNC19 (Novolac epoxy with 0.5% Nanoalumina), PCNC20 (Novolac epoxy with 1.0% Nanoalumina), PCNC 24 (Novolac epoxy with 1.5% Nanoalumina) and PCNC 25 (Novolac epoxy with 3.0% Nanoalumina).

Observing **Fig.2.23** and **Fig.2.24**, it seems that the bond strength between the polymer concrete nanocomposites and the steel surface is strongly correlated with the material stiffness. All the Novolac epoxy nanocomposites resulted in significantly higher stiffness than the polysulfide Siloxane spoxy nanocomposites. Moreover, incorporating nano-particles with the epoxy increased the stiffness of the slant shear specimen and therefore of the polymer concrete. The

correlation between the polymer concrete stiffness and the improved bond strength in slant shear test can be explained by the fact that the higher the stiffness of the polymer concrete section, the smaller the mismatch that section has with the steel substrate. Decreasing the mismatch between the stiffness of the two halves in the slant shear test would result in reducing the shear stresses at the interface. Novolac polymer concretes have a 147% higher stiffness than Siloxane polymer concrete and thus might observe lower shear stresses at the interface compared with Siloxane polymer concrete.

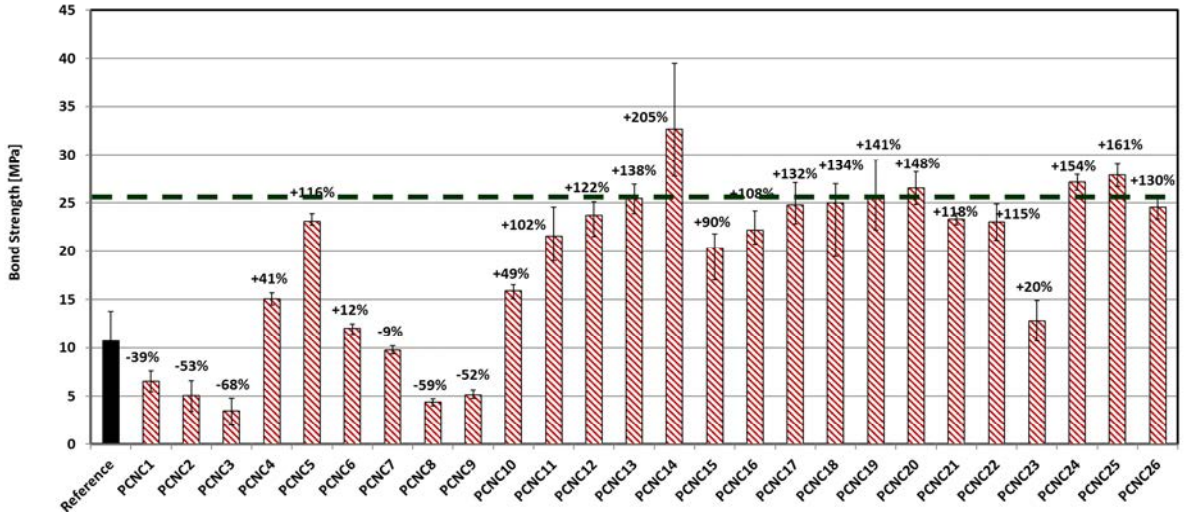

Fig.2.23: Bond strength of reference cement versus 23 nanocomposites. Dotted line represents a limit for the five top performing polymer/cement nanocomposites (1MPa=145psi).

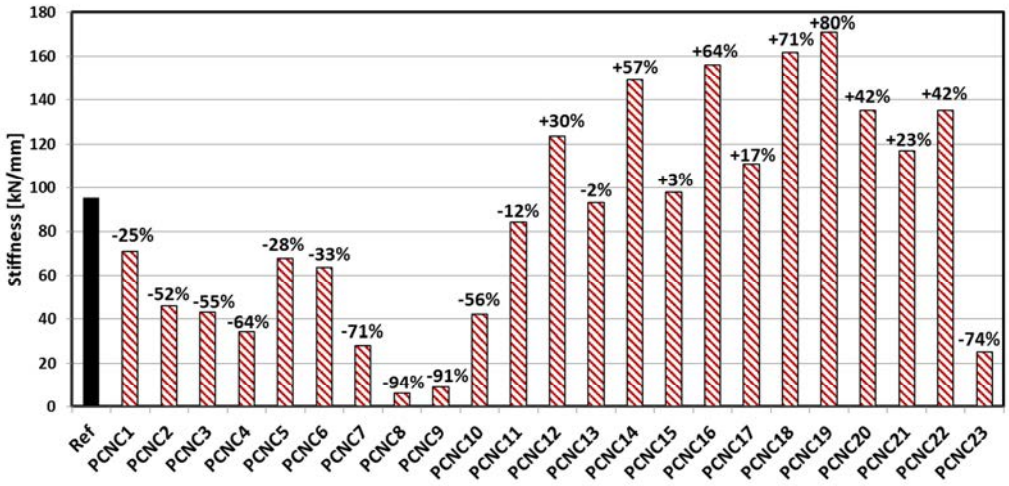

Fig.2.24: Stiffness of reference cement and 23 nanocomposites.

While the average apparent shear stresses computed above provide evidence of higher bond strength of Novolac polymer nanocomposite compared with standard repair mortar, further analysis to identify the true maximum shear stresses is necessary. We argue that the true improvement in shear strength might be higher than that deduced using the apparent shear strength. Computational modeling of the slant shear test is warranted to investigate this argument as addressed in Chapter 4 of this report.

Fig. 2.25: Example failure cones of the slant shear test.

A comparison of neat epoxy and epoxy incorporating functionalized and non-functionalized MWCNTs was conducted using FTIR and XPS. The results for PCNC4, PCNC5 and PCNC15 are shown in **Fig.2.26** and **Fig.2.27** for the FTIR and XPS methods, respectively. **Fig. 26** shows typical peaks of epoxy formed in all three materials for peaks up to 1600 cm^{-1}. No special peaks can be identified in one of the three epoxies and not identified in the other two epoxies. This might be attributed to performing analysis on the top of steel surface which might already include OH and Nitrogen. Further analysis is being conducted on the individual epoxy without steel.

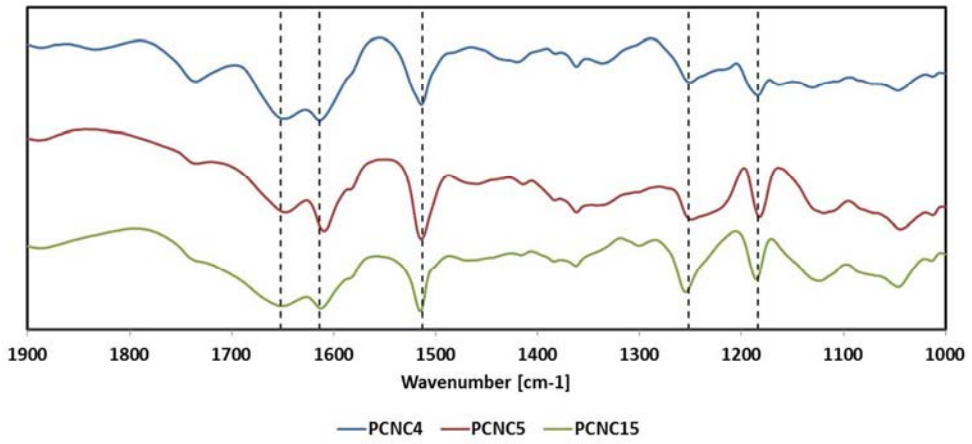

Fig. 2.26: FTIR results for PCNC4 (neat), PCNC5 (epoxy with functionalized MWCNTs) and PCNC15 (epoxy with non-functionalized MWCNTs).

Fig. 2.27 shows elemental analysis of reacted Carbon, Oxygen and Nitrogen as observed by XPS measurements. The measurements show a significant increase in carbon reaction when NF-MWCNTs were used. However, an interesting significant increase in Nitrogen reaction takes places when Functionalized MWCNTs is used which can be attributed to the formation of Amide due to reaction between the amine-based epoxy hardener and the COOH in MWCNTs. FTIR graph in **Fig. 2.26** shows the classical amide group at a peak of 1660 cm^{-1} confirming its formation.

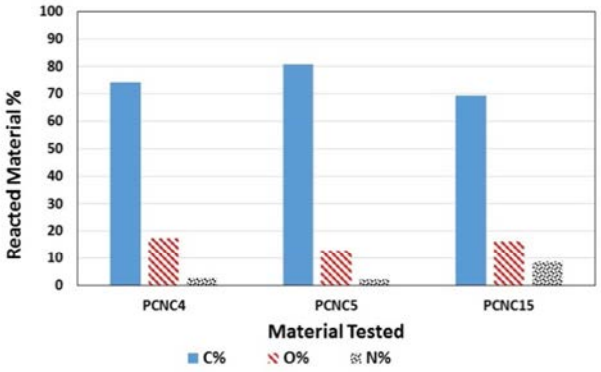

Fig. 2.27: XPS results showing elemental analysis of reacted Carbon, Oxygen and Nitrogen. PCNC4 (neat), PCNC5 (epoxy with functionalized MWCNTs) and PCNC15 (epoxy with non-functionalized MWCNTs).

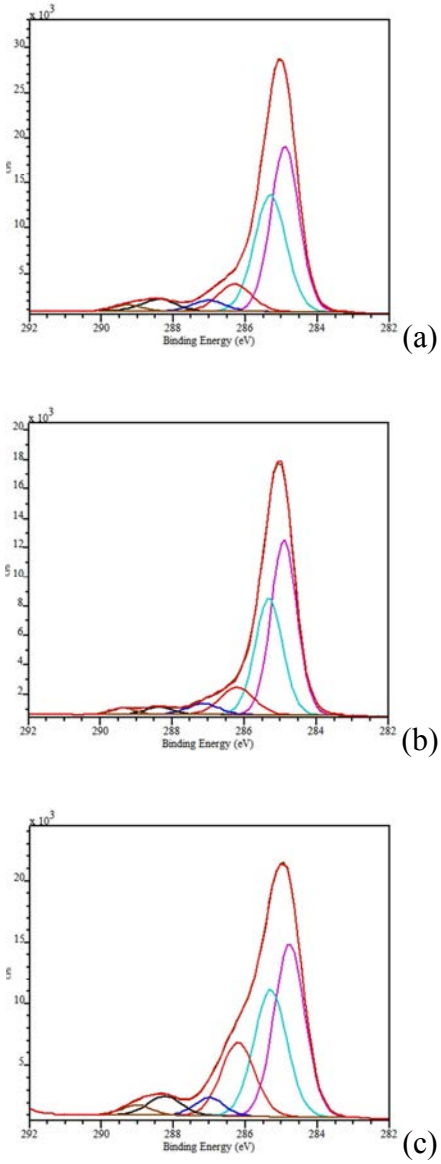

Fig. 2.28: XPS deconvoluted binding energy spectra showing binding energy for carbon bond in three materials (a) PCNC4 (neat), (b) PCNC5 (epoxy w/functionalized MWCNTs) and (c) PCNC15 (epoxy with non-functionalized MWCNTs).

Fig. 2.28 shows the deconvoluted binding energy spectra for the three materials. Of special interest is the peak at 286.3 confirming the strong Nitrogen bond of Functionalized MWCNTs. Further measurements and analysis are taking place to explain the effect of functionalization on the bond of epoxy with nanomaterials. **Fig. 2.29** shows the effect of elevated curing conditions on the bond strength between three Novolac PCNCs overlay and the steel surface. The bond strength of PCNC11 (Neat Novolac) cured under normal curing conditions (N) and cured under

high temperature of 80 °C and pressure of 10.3 MPa (H) were found to be 21.6 MPa (3133 psi) and 21.0 MPa (3046 psi) respectively. The bond strength of PCNC14 incorporating 2.0% nanoalumina was found to be 24.9 MPa (3611 psi) and 24.5 MPa (3553 psi) under normal curing and high temperature and pressure curing respectively. For PCNC 17 incorporating 1.5 wt.% MWCNTs, the bond strength under normal curing conditions and elevated temperature and pressure curing was found to be 22.3 MPa (psi) and 24.2 MPa (psi) respectively. Statistical analysis using student t-test with 95%level of confidence showed that the effect of the curing condition on the bond strength in the case of neat epoxy (PCNC11) and 2.0 wt% nanoalumina nanocompsite (PCNC14) was statistically insignificant. On the other hand, elevated temperature and pressure curing showed 7.6% increase in the bond strength for PCNC17 incorporating 1.5 wt.% MWCNTs. This increase was found to be statistically significant with 95% level of confidence.

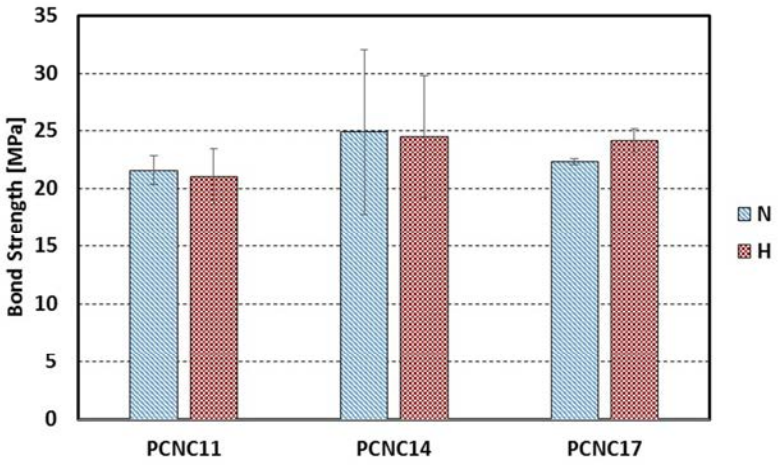

Fig. 2.29: Bond strength of Novolac PCNCs under normal curing (N) and high temperature and pressure curing (H) with PCNC11 (Neat Novolac), PCNC14 (Novolac with 2% Nanoalumina) and PCNC 17 (Novolac with 1.5% MWCNTs)

2.3.3. Stress-strain of PCNC

Fig.2.30-31 shows the results for compressive strength testing with strain gauges. **Fig.2.30** shows the stress-strain relationship of each of the best performing polymeric concretes in slant shear test for all used nanoparticles. The samples of interest are PCNC 11 (Neat Novolac), PCNC 12 (Novolac with 0.5% MWCNTs), PCNC 13 (Novolac with 1% nanosilica) and

PCNC14(with 2% Nanoalumina). From that, the modulus of elasticity was calculated using equation (1) and the compressive strength was obtained at the peak stress. Poisson's ratio as calculated by equation (2) is shown in **Fig.2.31**.

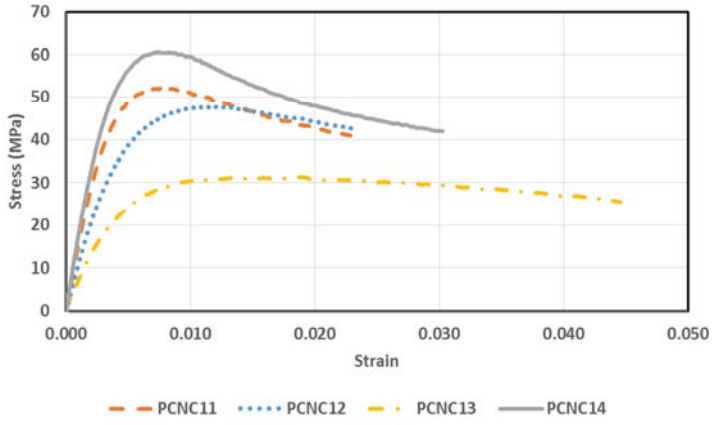

Fig.2.30: Stress-strain relationship for the best performing PCNC mixes.

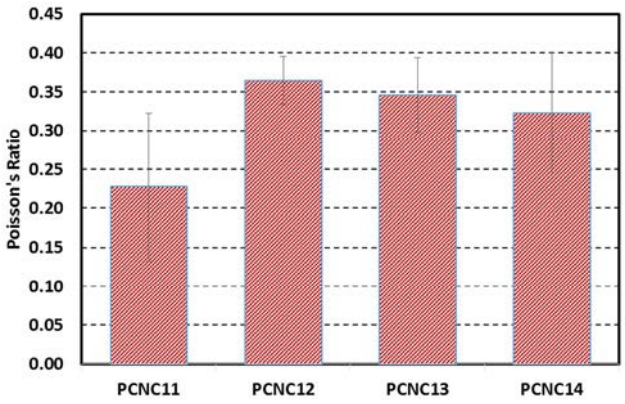

Fig.2.31: Poisson's ratio for the Novolac PCNCs with and without nanomaterials.

PCNC14 (Novolac with 2.0% nanoalumina) provided the highest modulus of elasticity while PCNC13 (Novolac with 1.0% nanosilica) provided the lowest. PCNC 12 (Novolac with 0.5% MWCNT's) provided the highest Poisson's ratio while PCNC 11 (neat Novolac) provided the lowest. This means PCNC14 will produce the lowest stiffness mismatch with the steel part in the

slant shear test. These results might be used to explain the difference in slant shear strength of the different materials as discussed below.

2.3.4. Polymer nanocomposite bond strength with shale-cement

Example load-displacement curves of Microfine cement (MF), PNC11, PNC19, PNC20, and PNC14 are shown in **Fig.2.32**. It is obvious that Novolac epoxy have a bond strength with shale much higher than the MF. Novolac epoxy shows improvement in the bond strength with shale of 174%. **Fig.2.33** shows the bond strength of different repair materials compared to reference material. Moreover, incorporating ANPs in Novolac epoxy improved its bond strength by 28.8%. **Fig.2.34** shows the bond strength of different Novolac polymer nanocomposites compared to Neat Novolac epoxy. Furthermore, Novolac bond is shown to result in a much more ductile interface that is capable of absorbing much higher energy compared with microfine cement interface. The ductility measured as the displacement at peak load and the toughness measured as the area under the load displacement curve are shown in **Fig.2.35** and **Fig.2.36,** respectively.

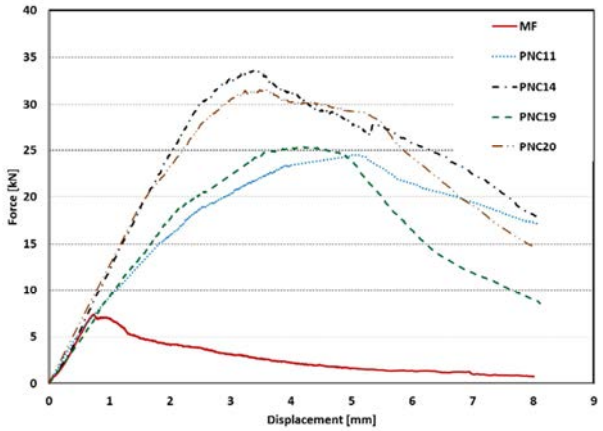

Fig. 2.32: Example push-out load-displacement curves of MF, PNC11, PNC14, PNC19, and PNC20.

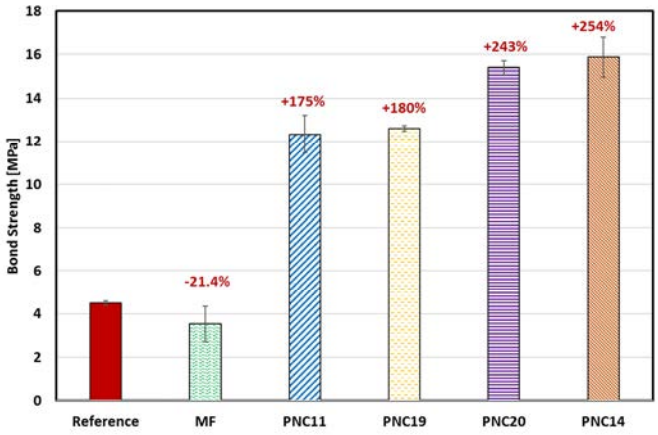

Fig.2.33: Bond strength for different Novolac epoxy-nanocomposites compared to reference cement (1MPa=145psi).

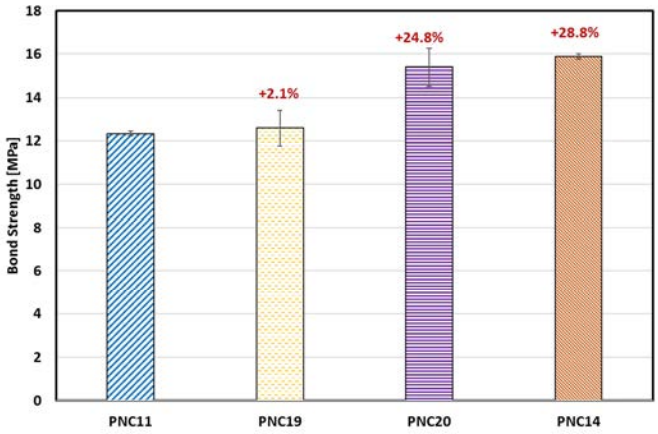

Fig.2.34: Bond strength for different Novolac epoxy-nanocomposites compared to neat Novolac epoxy (1MPa=145psi).

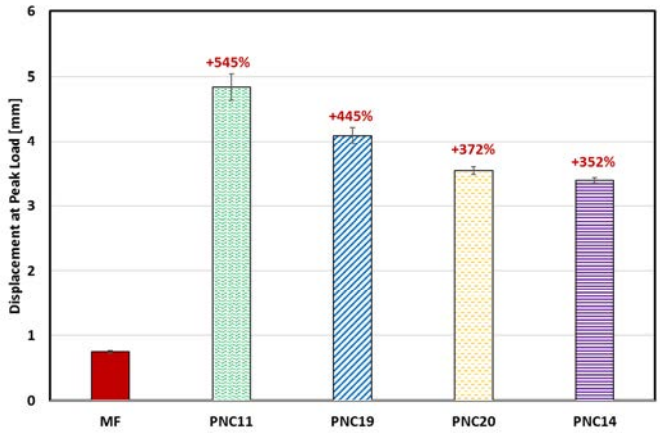

Fig.2.35: Displacement at peak load of different Novolac epoxy nanocomposites compared to microfine cement

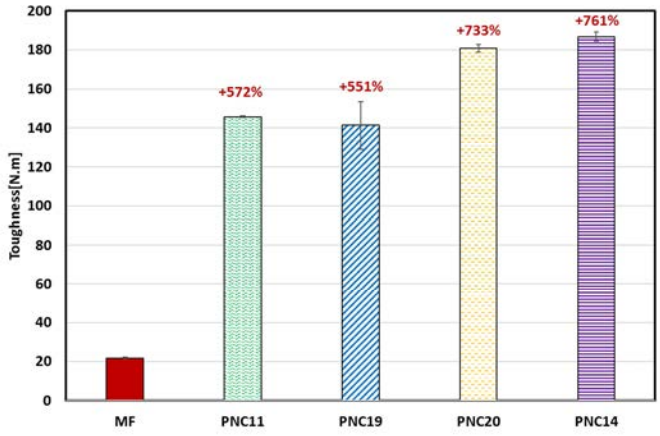

Fig.2.36: Toughness of different Novolac epoxy nanocomposites compared to microfine cement

2.3.5. Physical characteristics of polymer nanocomposites

Temperature-tan delta curve shown in **Fig. 2.37** was used to determine the Glass Transition Temperature (T_g) for the epoxy incorporating deferent ratios of nanoparticles. The T_g for Neat Novolac epoxy (The matrix of PCNC 11), Novolac epoxy incorporating 0.5% MWCNTs (The matrix of PCNC 12), and Novolac epoxy incorporating 2.0% MWCNTs (The matrix of PCNC 21) were found to be 64.2 ^oC, 64.9 ^oC, and 64.9 ^oC respectively. The results showed that the MWCNTs has no significant effect on the T_g of the Novolac epoxy.

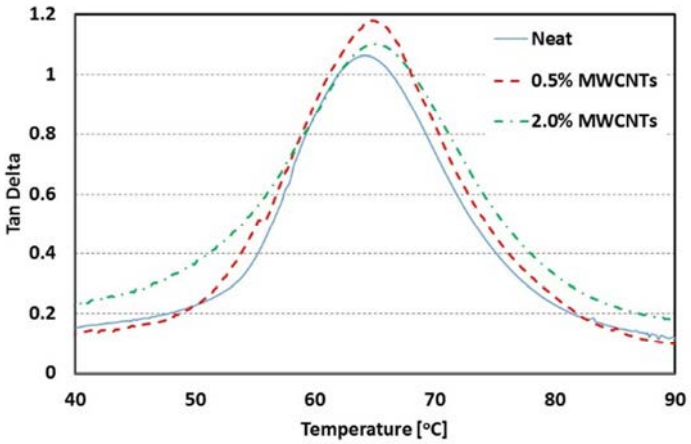

Fig.2.37: Temperature-tan delta curves for Neat Novolac epoxy, Novolac epoxy incorporating 0.5% MWCNTs, and Novolac epoxy incorporating 2.0% MWCNTs.

Fig.2.38 presents the viscosity test results for microfine cement and Novolac epoxy-polymers nanocomposites. As shown in **Fig.2.38** the viscosity of Novolac epoxy incorporating 0% (Neat), 0.25%, 0.5%, and 1.0% nanoalumina is lower than the viscosity of the microfine cement by 18.3%, 16.1%, 13.4%, and 11.7% respectively. The limited change in viscosity did not influence the ability of the polymer nanocomposite to flow

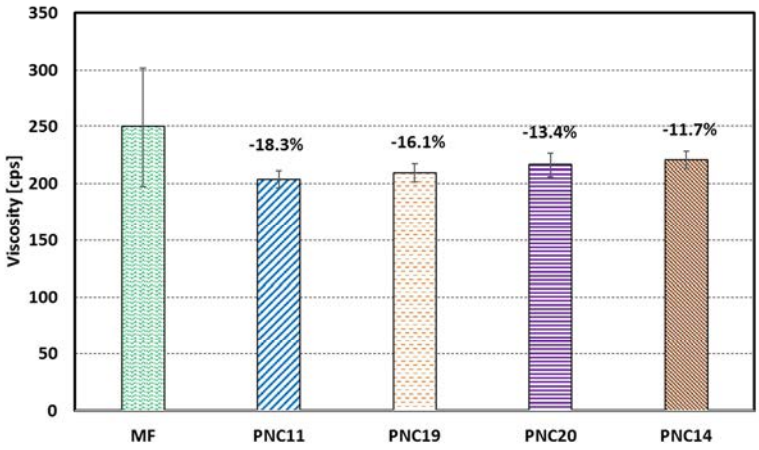

Fig.2.38: Viscosity of reference cement versus the new tested polymer nanocomposites.

FTIR spectrographs for PNC11, PNC20, PNC16, and PNC13 are shown in **Fig. 2.39**. We first note that there is very little difference between the spectra of neat Novolac epoxy (PNC1) and that of epoxy incorporating nanosilica (PNC13) and MWCNTs (PNC16). In those three spectra,

the absorption bands corresponding to C-H band (2850–2930 cm−1), epoxide ring (~830 cm−1), N-H band of primary amines (1590– 1615 cm−1), O-H groups (~3350 cm−1), C-N band (1030–1115 cm−1) and ether bands (~1230 cm−1) are all apparent and have similar relative ratios to the base spectra. However, the spectra of PNC20 look very different and the peaks have a relatively higher ratio to the base spectra. The difference in the Novolac epoxy-ANPs nanocomposite can be explained by the fact that alumina-particles are known as an amphoteric substance, meaning it can react with both acids and bases which allow it to act as an acid with a base and a base with an acid. ANPs thus reduce the epoxy curing reaction and consequently leave a relatively large amount of the epoxy resin groups (such as the epoxide ring, N-H band of primary amines, O-H groups) unreacted and available. This is represented by the significant increase in the epoxide ring, O-H and primary N-H band intensity in the FTIR spectra. This role of ANPs results in increasing the epoxy's chance to react with the sand blasted steel surface and thus improve the adhesion strength between PC and steel or shale. The increase in ANPs content would be expected to further increase the amount of unreacted epoxy groups and consequently the adhesion strength. This explains the significant increase in bond strength (+51%) observed with 2.0% ANPs compared with neat epoxy.

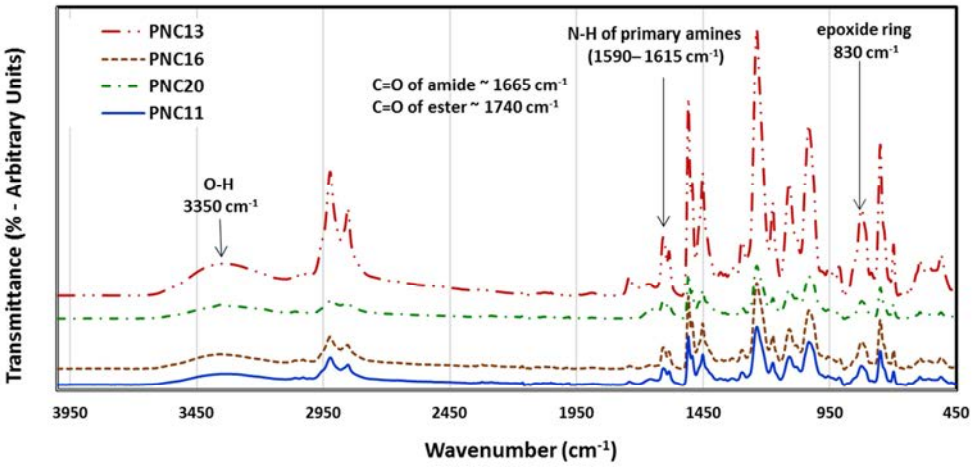

Fig.2.39: FTIR spectrographs for PNC11, PNC13, PNC16, and PNC20.

The FTIR spectra also show that MWCNTs with its COOH functionalization resulted in esterification reaction with epoxy and produced the ester and amide peaks appearing at 1740 cm-1 and 1665 cm-1, respectively. However, the low content of COOH functionalizing in MWNCTs

makes this reaction ineffective due to the fact that curing of Novolac epoxy results in similar chemical groups. This explains why the MWCNTs were not able to make significant improvement in adhesion strength between epoxy and steel. Finally, no special features can be detected due to the addition of nanosilica to epoxy. Nanosilica, therefore, seem to work as solid fillers with higher stiffness than epoxy and thus might only improve PC stiffness, but is unlikely to improve the bond strength with steel.

FTIR spectrographs of PNC4, PNC15, and PNC27 are shown in **Fig.2.40**. The characteristic peaks of the synthesized siloxane-epoxy/MWCNTs samples appeared at 3330–3500 cm−1 (O-H), 2750–2940 cm−1 (C-H), 1460 cm−1 (C-H, CH2 and CH3), 1039–1100 cm−1 (Si-O-Si and C-O-C), 1250–828 cm−1 (C-H in Si-CH3), 560 cm−1 (Si-O-Si). A peak appears near 1605 cm−1 due to Si–C6H5 vibrations. The remaining epoxy groups (oxirane ring) appeared at 940 cm−1. The spectrographs of the three MWCNTs show no difference and thus do not indicate any chemical interaction with MWCNTs because non-functionalized MWCNTs was used in the preparation of the PC composite. The ability of the relatively low content of MWCNTs (0.5 wt. %) to alter the mechanical properties might be attributed to the interaction between the nanoscale MWCNTs and epoxy. FTIR peaks in the spectrographs show that the peaks of the epoxy compounds in epoxy incorporating 0.5 wt. % MWCNTs is higher than that of the neat epoxy. More interestingly, FTIR peaks of epoxy incorporating 2.0 wt.% MWCNTs is lower than that of neat epoxy. The above observation can be explained by considering the ability of MWCNTs to hinder epoxy reaction. At a low MWCNTs content < 0.5 wt.%, it seems that MWCNTs inhibit epoxy reaction resulting in lower cross-linking than that of neat epoxy. This in its turn results in reducing PC strength and improving PC strain at failure and fracture toughness.

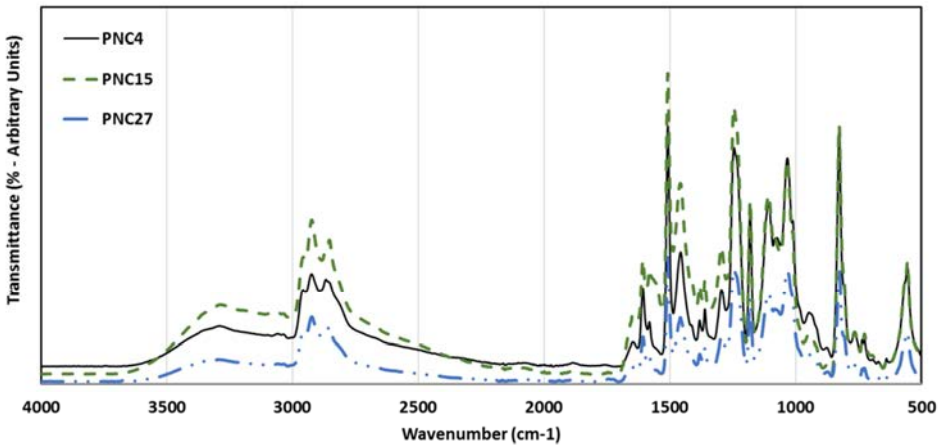

Fig.2.40: FTIR spectrographs for PNC4, PNC15, and PNC27.

On the other hand, increasing the MWCNTs content gradually results in reducing that effect of inhibiting epoxy reaction. That might be to the fact that MWCNTs will tend to agglomerate and entrap air which would reduce the strength. However, the relatively large MWCNTs content helps in maintaining the integrity of PC and allows it to slightly improve the strength and strain at failure. It is apparent that the significance of MWCNTs on strength and fracture can be explained based on its chemical effect at relatively low content< 0.5 wt.% but the explanation becomes extremely complex with many interdependent factors at high MWCNTs content. Further research is warranted to measure the cross-linking density of epoxy incorporating the different amount of MWCNTs.

To characterize the degree of cross-linking of the different polymer nanocomposites, DMA testing was conducted. The suggested degree of crosslinking measure (X_{Link}) for PCN11, PCN19, and PCN20 is calculated and shown in **Fig.2.41**. The results show that incorporating 0.5% and 1.0% ANPs reduces Novolac epoxy crosslinking by 15.8% and 16.4% respectively. The above analysis confirms the FTIR observations and is consistent with the observation that incorporating ANPs results in a more flexible epoxy nanocomposite compared with neat epoxy. Similar testing was conducted to polymer nanocomposites incorporating MWCNTs but cannot be directly inferred using the above method for the physical significance of carbon nanotubes on the mechanical modulus of PC. A composite model was implemented and used to predict the significance of NF-MWCNTs on the degree of cross-linking on polymer nanocomposite. The

results are shown in **Fig.2.42** indicating that NF-MWCNTs to have insignificant impact on polymer cross-linking compared with ANPs.

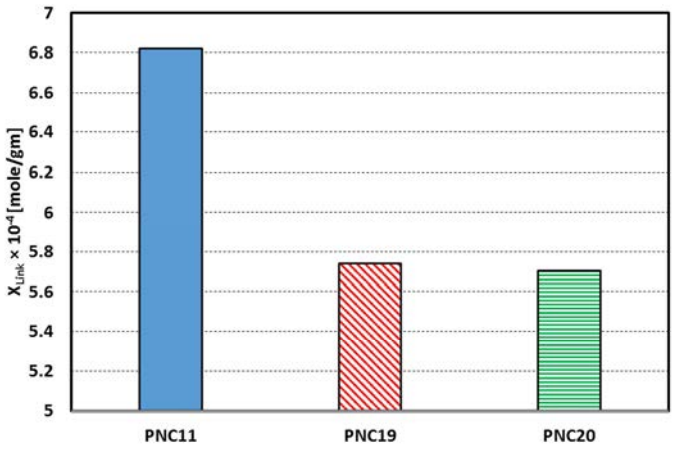

Fig.2.41: X_{link}: A measure of the degree of crosslinking for PNC11, PNC19, and PNC20.

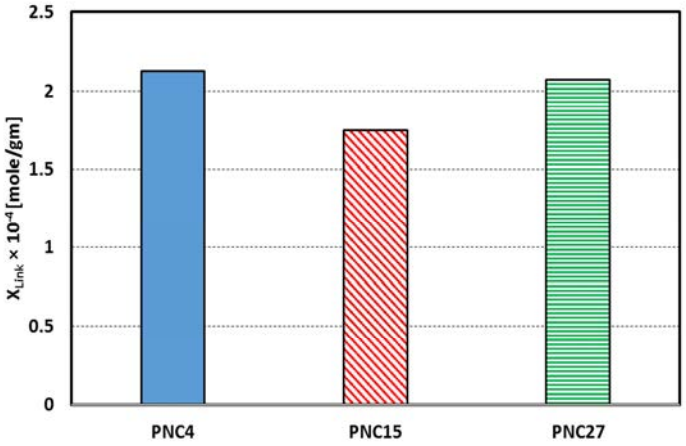

Fig.2.42: X_{link}: A measure of the degree of crosslinking for PNC4, PNC158, and PNC27.

2.3.6. Polymer nanocomposites in microannulus space

Photomicrographs of the shale-cement interface repaired with microfine cement, PNC 4 (neat Novolac epoxy) and PNC20 (Novolac epoxy incorporating 1.0% ANPs) are shown in **Fig. 2.43**, **Fig. 2.44** and **Fig. 2.45** respectively. While **Fig. 2.43** shows the existence of microcracks at the cement-shale interface repaired with microfine cement, **Fig. 2.44** and **Fig. 2.45** show no gaps and demonstrate the ability of epoxy with and without ANPs to flow and seal the shale-cement interface. A close look at **Fig. 2.44** and **Fig. 2.45** shows the ability of the ANPs-epoxy nanocomposite to infiltrate into the porous shale interface and fill the microcracks at the shale

surface. This ability of epoxy and ANPs-epoxy nanocomposite to penetrate the shale microcrack network at the interface enables creating mechanical interlocks in addition to the adhesion between epoxy and shale. These interfacial microcracks at the shale surface also provide potential leakage pathways and thus compromise wellbore seal integrity. The penetration of the epoxy nanocomposite repair material not only improves the shale-cement bond strength, but it also seals leakage pathways adjacent to the interface and thus improves wellbore seal integrity.

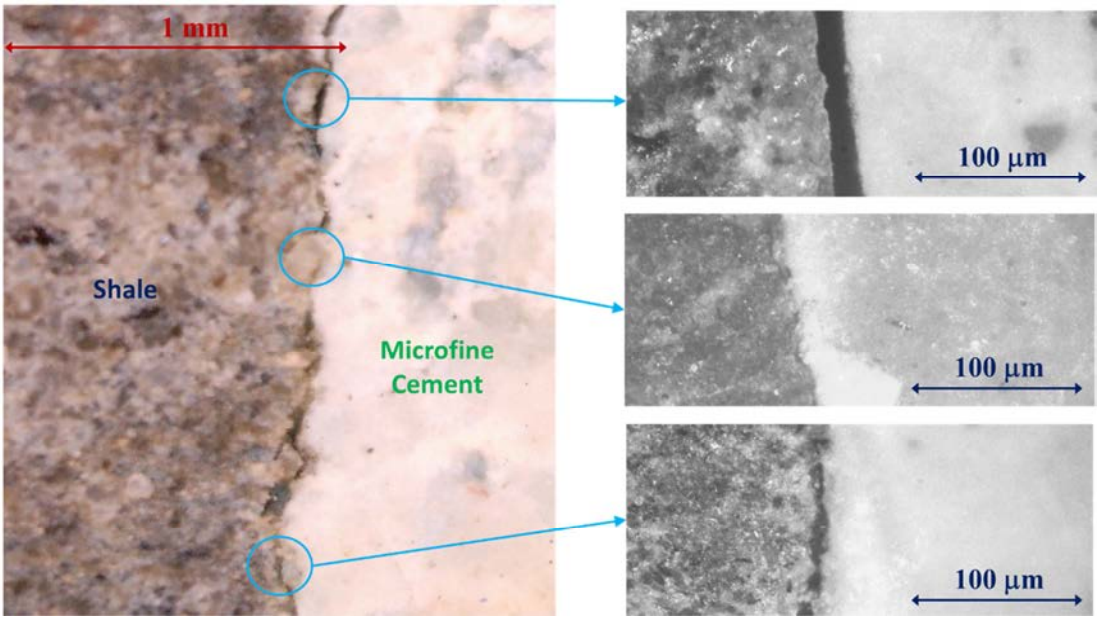

Fig. 2.43. Microscopic images of shale-microfine cement interface with two different levels of magnification showing areas with gap between microfine cement and shale.

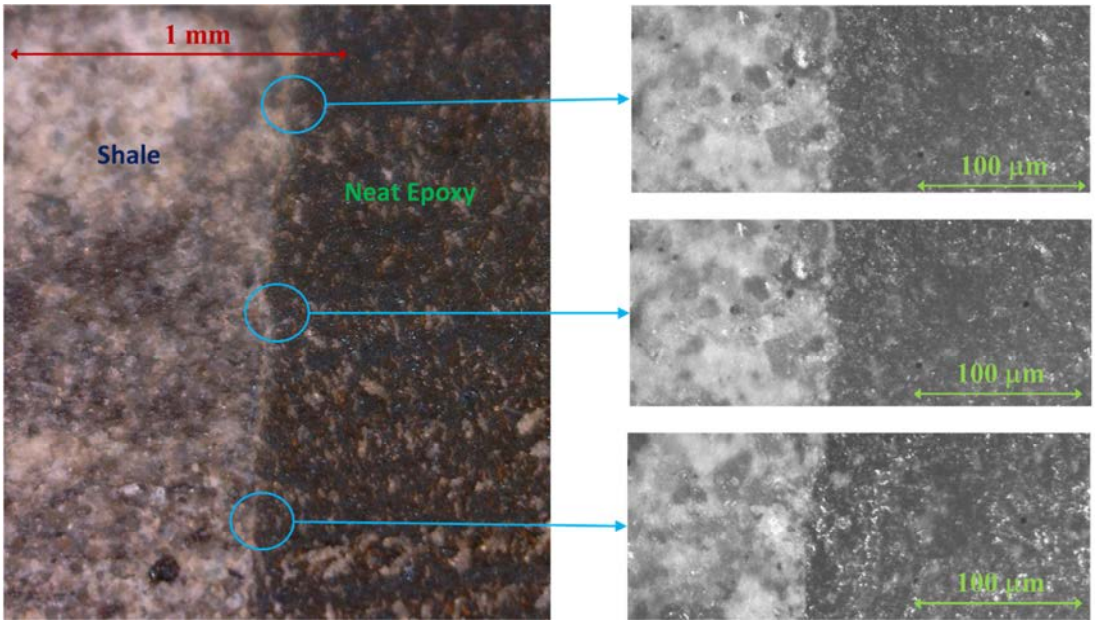

Fig. 2.44. Microscopic images of shale-neat epoxy interface with two different levels of magnification showing the ability of the neat Novolac epoxy repair material to completely fill the gap at the shale-cement interface.

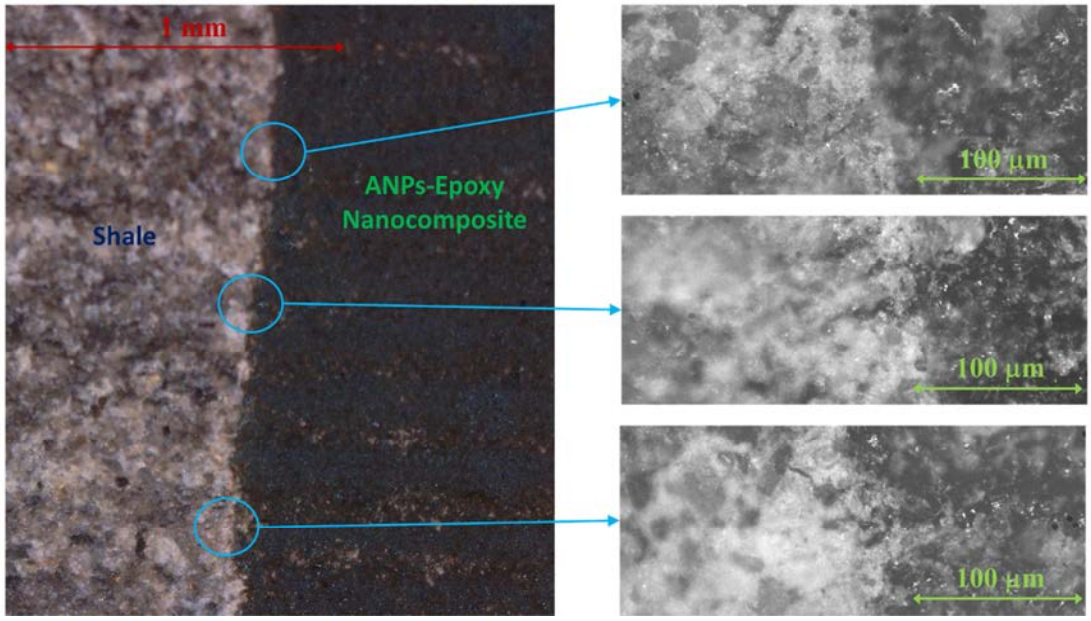

Fig. 2.45. Microscopic images of shale-1.0% ANPs-Novolac epoxy polymer nanocomposite interface with two different levels of magnification showing the ability of the Novolac epoxy incorporating ANPs repair material to completely fill the gap at the shale-cement interface.

The ability of microfine cement to fill micro cracks with crack width of 13, 25, 50, 75, and 100 microns was measured using plexiglass sheets. Microfine cement failed to fill micro cracks with

crack width lower than 50 microns. For 50, 75, and 100 microns crack width, microfine cement was able to partially fill the micro cracks. However, microfine cement was not uniformly distributed throughout the crack space. In addition, bleeding of cement was observed while injecting. **Fig.2.46**, **Fig.2.47**, **Fig.2.485**, and **Fig.2.49** show microfine cement injected in cracks with crack width of 25, 50, 75, and 100 microns respectively. On the other hand, neat Novolac epoxy and Novolac with 2% nanoalumina were able to 100% fill the crack width of 13 microns. **Fig.2.50 and Fig.2.51** show the injection of neat Novolac, Novolac with 2.0% nanoalumina, into 13 microns crack.

Fig.2.46: Microfine cement injected in 25 microns crack.

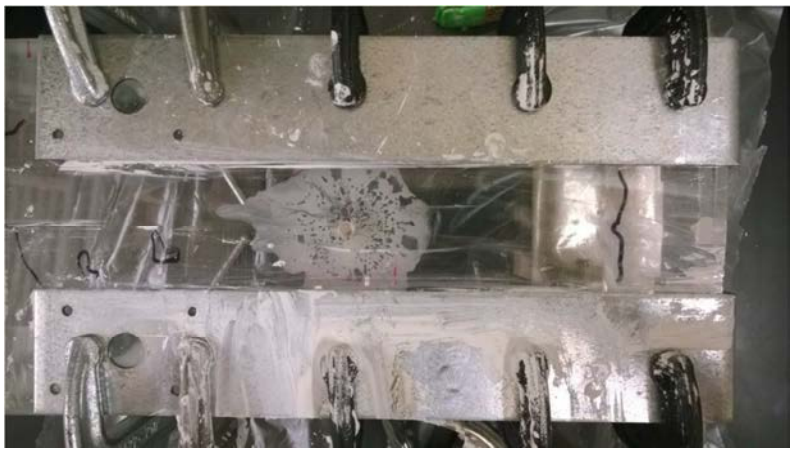

Fig.2.47: Microfine cement injected in 50 microns crack.

Fig.2.48: Microfine cement injected in 75 microns crack.

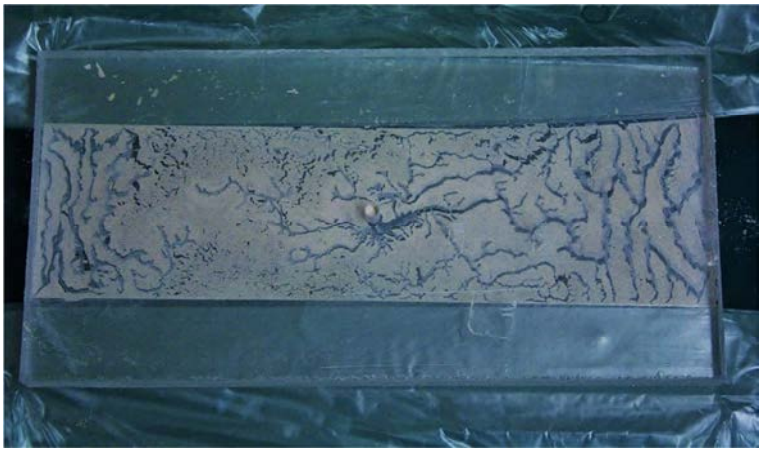

Fig.2.49: Microfine cement injected in 100 microns crack.

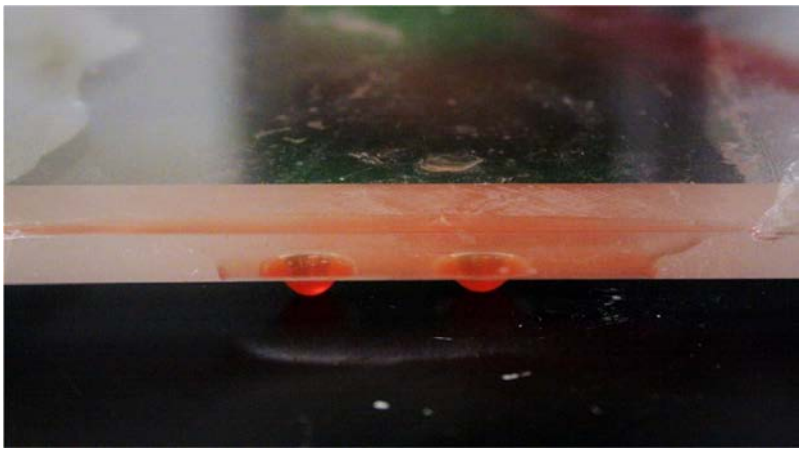

Fig.2.50: Neat Novolac epoxy injected in 13 microns crack.

Fig.2.51: Novolac epoxy with 2.0% Nanoalumina injected in 13 microns crack.

2.4. Conclusion

Twenty-six polymer-cement nanocomposites were developed and characterized specifically for their flowability and ability to improve bond between steel and cement. Furthermore, nine polymer nanocomposites were developed and their abilities to flow in microannulus below 50 microns and to seal cement-rock (shale) microannulus were examined. The experimental investigations showed that polymer cement nanocomposites have superior bond strength to steel compared with any cement and concrete. Furthermore, polymer nanocomposites specifically, Novolac epoxy reinforced with Multi-walled carbon nanotubes and/or alumina nanoparticles were shown to have superior capabilities in flowing and sealing compared with microfine cement currently used as the classical repair material of microannulus by the industry. Our investigations showed epoxy Novolac reinforced with nanomaterials produces the best performance being able to maintain low viscosity and flow at relatively small microannulus below 50 microns. On the other hand, microfine cement showed weak performance being unable to flow at any microannulus below 50 microns and showed multiple signs of segregation and relatively low bond strength as repair material with shale. Significant microcracks were observed between the microfine cement and shale interfaces due to shrinkage. Such microcracks will easily allow fluid, specifically gas, flow and will definitely undermines the well integrity. Microstructural investigations of polymer nanocomposites showed their ability to completely fill microannulus

gaps below 50 microns and to penetrate the shale layer and to seal it. The above work has been published or submitted for publication (Genedy et al. 2014, Douba et al. 2015, Genedy et al. 2016, Douba et al. 2016). Further research investigations including field trials of polymer nanocomposites in sealing microannulus in abandoned oil wells are warranted. The above research shows that polymer nanocomposites can play an important role in improving well integrity.

3. Integrated seal system testing

3.1 Introduction

The integrated seal system testing was directed at (1) characterizing flaws in wellbore systems, and (2) testing the effectiveness of select repair materials to repair the flawed wellbore systems. Wellbore system samples, comprised of a casing set in a sheath of conventional oil well cement, were created with various flaws in the cement (e.g., fractures) and at the cement-casing interface (e.g., mircroannuli, corroded casing). The 20 cm long wellbore samples had an exterior diameter of 10 cm and an interior diameter of the steel casing of 5 cm. These wellbore systems were placed in a pressure cell capable of applying independent confining pressure, internal casing pressure, and pore pressure. The pressure vessel was configured to allow permeability to be measured along the axis of the seal system (the wellbore axis). The flow or permeability of the wellbore system was measured under various confining pressure and internal pressure conditions, both before and after repair. A number of different methods were used to introduce the repair materials into the flawed wellbore systems. Repair materials were polymer-based composites developed in this project as well as a "conventional material" - microfine cement – for comparison to the polymer-based materials. Post-test visual observations were made of repair effectiveness.

3.2 Methods and specimen preparation

3.2.1 Pressure vessel

The pressure vessel is shown in **Fig 3.1**. The pressure vessel was designed and constructed specifically for this project. The end caps included ported bosses that were designed to fit inside the casing of the test samples. In this way, the casing can be isolated and accessed so that it can be pressurized. Before sample construction, the casings were machined to provide an exact and tight fit in the pressure vessel. Removable bladders were used to develop confining pressure between the sample and the pressure vessel. These bladders were fabricated with molding rubber. One set of ports on both ends of the pressure vessel access the casing. Another set of ports on both ends of the pressure vessel access the ends of the sample, and are connected to the permeameter. A hydraulic pump is connected to a port in the sidewall of the vessel to introduce

and control the confining pressure. The connections to the pressure vessel are shown in the schematic in **Fig.3.2**. The assembled pressure vessel is shown in **Fig.3.3.**

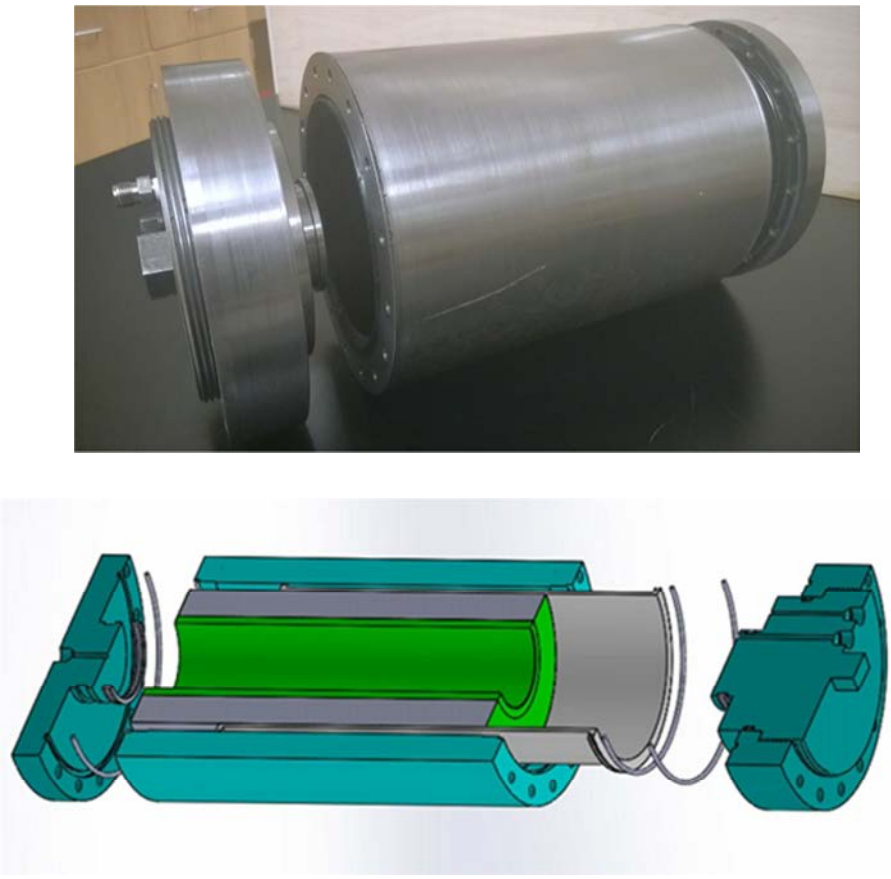

Fig.3.1: (a) Top: photograph of pressure vessel with end caps unattached; (b) Bottom: cut-away schematic of pressure vessel.

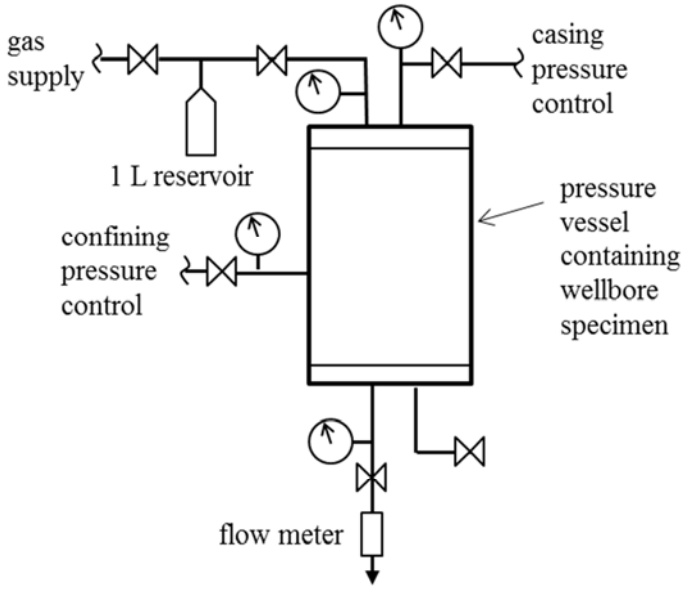

Fig.3.2: Schematic of experimental configuration used to measure gas flow through cement-casing specimens under variable confining pressure and casing pressure.

Fig.3.3: Assembled pressure vessel connected to permeameter.

3.2.2 Permeameter

The permeameter system is the series of valves, tubing and measurement devices used to supply and measure gas flow through the wellbore samples while under confining pressure and casing pressures. The valves and measurement devices were mounted on a panel as shown in **Fig.3.4.** The system can provide gas pressure upstream and downstream of the samples up to 14 MPa.

The design of the permeameter is such that it allows three types of gas permeability measurements to be conducted: constant pressure steady-state (high flow rate measured using a flowmeter), quasi-steady-state (lower flow rate interpreted from the pressure changes in upstream gas volume, so-called pressure fall-off (PFO) tests), and transient pulse methods. The "upstream" volume can include a 1 L reservoir during the quasi-steady-state PFO tests or transient tests.

A pressure gauge measures the pressure in the upstream portion of the permeameter. For steady-state flow tests, the regulator is adjusted to provide a constant supply of pressure to the upstream at the desired pressure. A flow meter can be connected to either the upstream or downstream side of the sample to measure the flow that passes through the sample. Most tests vented the downstream to atmosphere.

For lower flow rates, PFO measurements are made. These tests by-pass the flowmeter, and an additional reservoir volume of 1 L is often included in the system. The flowrate from the upstream volume, Q, can be found from the rate of change of the pressure in the upstream volume (dP/dt) for an isothermal process from

$$Q = \frac{V}{P}\frac{dP}{dt} \qquad \textbf{(3.1)}$$

where V and P are the volume and pressure of the upstream, respectively.

A soap-film flowmeter was used to calibrate the pressure fall-off method for flows less than 0.3 L/min. The pressure fall-off method was found to be within 2% of the measurements taken with the soap-film flowmeter.

For very low permeability specimens, transient/pulse test can be done. In this test the pressure decay in the upstream side is measured. No transient tests were conducted on wellbore samples.

The system was tested with an empty pressure vessel to test for the effective upper bound of permeability that the system can measure. At 14 kPa (2 psi) inlet pressure, the flow rate was 7.5 liters per minute (125 cm^3/s). The equivalent system permeability for this flowrate is 15 darcy ($1.5 * 10^{-11}$ m^2).

Fig.3.4: Permeameter for gas permeability measurements through cement-casing systems.

The plumbing of the pressure vessel was modified to allow for a "back-pressure" during some gas flow testing. The backpressure system consists of a valve and pressure gage (**Fig.3.5**). A constant pressure is established in the system (sample, upstream, and downstream), then upstream pressure is increased to do a fall off test. Using the valve, downstream pressure is maintained at the initial downstream pressure (typically within +/- 7 kPa). A flowmeter was connected on the atmospheric side of the valve to measure the flow.

Fig. 3.5: Control valve at downstream to maintain back-pressure

3.2.3 Sample preparation

The samples are hollow cylinders comprised of cement and steel to represent a wellbore system (casing and cement). A thin steel cylinder (casing) with an inner diameter of 52.8 mm is surrounded with 35.5 mm of cement paste. To create the sample, the steel cylinder is fixed in the center of the mold with a cap and plug, and cement is poured into the mold (**Fig.3.6a**). The specimens had nominal cured dimensions of 20.3 cm length, outer diameter of 9.6 cm, and inner diameter of 5.3 cm (**Fig. 3.6b**). Steel casings of various thicknesses were used, including 0.380, 0.235, 0.175, and 0.150 cm.

In some of the casings, a 0.12 cm diameter hole was drilled into the steel cylinder halfway along its length. A plastic tube was inserted into the hole to allow for injection of repair material into the fault between the cement and steel (**Fig.3.6a**). A fastener keeps the tube intact, and a small piece of Styrofoam inside the cylinder keeps any cement going into the tube during sample curing. Acetone was poured into the tube to dissolve the foam when needed. A few samples were also created with an injection tube fixed to the outside of the casing and cement cast over it.

The following mix design was used to for the cement paste:

- Type H Cement 1000 grams
- fly ash 100 grams
- plasticizer 3 grams
- water 330 grams

Samples were cured in a 55°C hot water bath for 7 days, and stored in a 100% humidity concrete curing room until tested. After removal from casting molds, samples are kept at 55 C for 14 days. Then they are moved to a humid curing room and kept there for a day. After that and in between tests, they are kept in the lab at room temperature. A cured sample is shown in **Fig.3.6b**.

Fig. 3.6: a) Steel centered in mold ready for cement to be poured in annulus. The tube connected to the hole in the steel is visible inside the steel casing. B) Cured sample.

There are three general types of flaws that were induced in the specimens: slot flaw, microannulus, and/or a radial cement fracture. To create the slot flaw, a 0.45 mm thick and 50 mm wide steel sheet is attached along the steel cylinder to create a fault between the cement and steel (**Fig.3.7a**). An example of a sample with a slot flaw is shown in **Fig.3.7b**.

Fig. 3.7: a)Steel sheet attached to the cylinder prior to casting cement annulus to create a 'slot flaw' in the specimen, and b) Cured sample with slot flaw visible at contact between cement and steel casing.

Initial trials were attempted with a number of methods to create microannuli, including:

- Using release film during the sample pour between the interface and removing when partially cured.
- "Knocking" or pressing the pipe loose. This tends to damage the specimen and was not pursued.
- Cooling the sample with liquid nitrogen or dry ice.
- Heating with a gas torch.

Radial cement fractures were created by both the cooling and heating methods, depending on the temperature difference created.

From the initial trials, two methods were pursued to create microannuli. One method involves first wrapping the casing with release film – this method produces a large microannulus. The initial method we developed for using release film was to allow the samples to first fully cure after casting cement. After curing, liquid nitrogen is added to the casing so that the casing could be pulled out for removal of the release film. After the film is removed the casing is pushed back into the cement sheath. This method produces a microannulus with a relatively large gap. This procedure is shown in **Fig. 3.8**. Subsequently, we developed a method where after 24 hours of curing, the release film is removed and the sample is allowed to continue to cure.

Fig. 3.8 – A sample with a microannulus created by the release film method. From left to right: sample at end of curing showing release film (plastic) on top of sample; cooling casing with liquid nitrogen; removing release film and casing; casing removed from cement sheath.

The other method is to cast and cure an "intact" sample. After curing, the casing is cooled by dry ice (**Fig.3.9**). In some cases, the casing was subsequently pressed axially to ensure debonding of the interface. This method produces a relatively tight, frictional microannulus. Using liquid nitrogen to cool the casing tended to produce radial fractures in the cement.

Fig. 3.9: Using dry ice to cool the casing and de-bond the steel casing and cement sheath

We produced samples with a range of different casing thicknesses. The original casing thickness of 3.8 mm is so thick that it is difficult to reach internal pressures that can induce significant deformation. Consequently, we have prepared and tested samples with 2.35, 1.8 and 1.5 mm thick casing as well. Samples were also produced with corroded casing (**Fig. 3.10**). The casing was corroded by simply wetting the casing and exposing it to atmospheric conditions.

Fig. 3.10 – Casing with (left) and without (right) corrosion.

3.2.4 Repair methods

Prior to repair, all samples were tested in the pressure vessel to measure the pre-repair flow. We used three different methods to introduce repair material. The first was to remove the sample from the pressure vessel, pool the repair material on top of the sample and allow it to flow into the flaw by gravity. This method works with flaws on the order of 100 microns or larger. With smaller flaws, the repair material may not enter the flaw.

The second method was to use the so-called "epoxy capsule" to inject repair material into the microannulus (**Fig. 3.11**). After removing the sample from the pressure vessel, the sample is placed inside a thick-walled PVC pipe with a fixed bottom cap. Epoxy is placed on top of the sample, and an upper cap is placed on top of the PVC pipe. The headspace is pressurized to 0.7 MPa, thereby forcing the repair material into a flaw.

Fig. 3.11 – Figure showing the "epoxy capsule" method for injecting repair material into sample with flaws.

The final method for repair material injection involved use of the port (hole) in the middle of some of the casings used to create samples. After opening one end of the pressure vessel, the tube coming out of the port inside the casing was filled with epoxy and shut (**Fig. 3.12**). After putting end cap back on and applying a confining pressure, the casing pressure could be increased. The intent was for the casing pressure to squeeze the tube and push epoxy into the microannulus through the port.

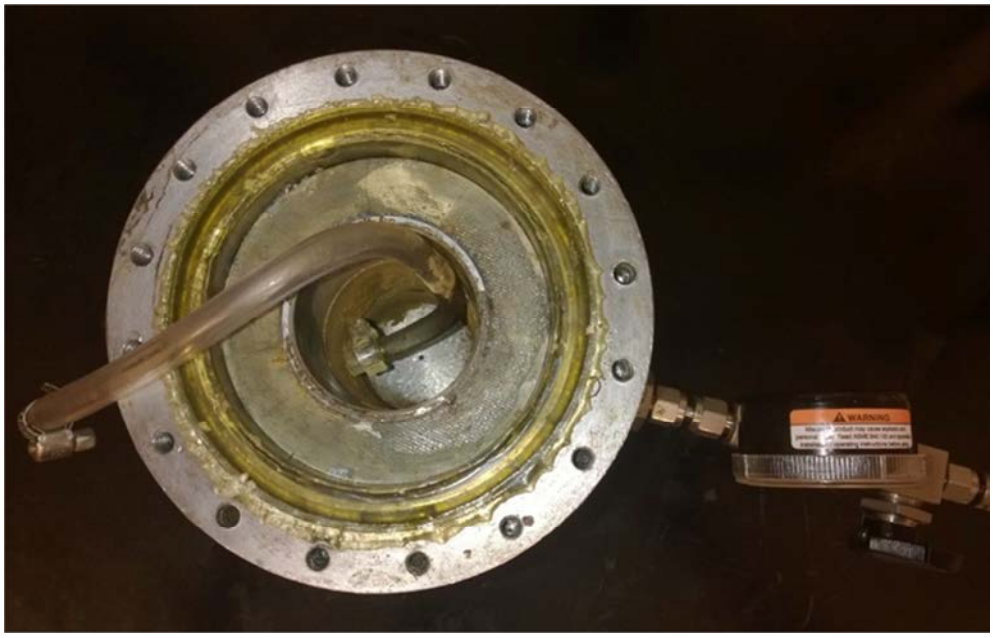

Fig. 3.12 – Sample 24 in pressure vessel with tube with epoxy. End cap was replaced and casing was pressurized in an attempt to inject epoxy into microannulus.

3.2.5 Interpretation of flow measurements

Axial flow through the wellbore sample was interpreted as permeability using Darcy's law. The permeability, in turn, was frequently expressed as the hydraulic aperture of the flaw. At high flow rates, the flow may include both "Darcy" type flow as well as non-linear flow. When the flow rate was more than about 0.5 L/min, measurements of flow are made at a series of different pressures. These data allow the linear flow and the non-linear flow components to be decoupled, and the permeability can be obtained from the data as described below. At flows smaller than about 0.1 L/min, the contribution of the non-linear component appears to be negligible and the measured flowrates are used directly in Darcy's law to interpret permeability

$$k = \frac{Q\mu}{A}\nabla P \qquad \textbf{(3.2)}$$

where ∇P is the gradient, Q is the volumetric flowrate, k is the permeability, A is the cross sectional area involved in the flow, and μ is viscosity.

Flow that includes both linear and non-linear flow contributions can be represented by Forchheimer's equation

$$-\nabla P = \frac{\mu}{kA}Q + \frac{\beta\rho}{A^2}Q^2 \qquad \textbf{(3.3)}$$

where ∇P is the gradient, Q is the volumetric flowrate, k is the permeability, β is the inertial coefficient, A is the cross sectional area involved in the flow, μ is viscosity, and ρ is density. Eqn (3) can be rewritten as

$$-\frac{\nabla P}{Q} = \frac{\mu}{kA} + \frac{\beta\rho}{A^2}Q \qquad \textbf{(3.4)}$$

Plotting the left-hand side of (4) vs. the flowrate yields a straight line with a slope that is a function of the inertial coefficient and an intercept proportional to permeability (**Fig.3.13**). In the absence of non-linear flow, the slope will be zero and Eqn (1) reduces to Darcy's Law.

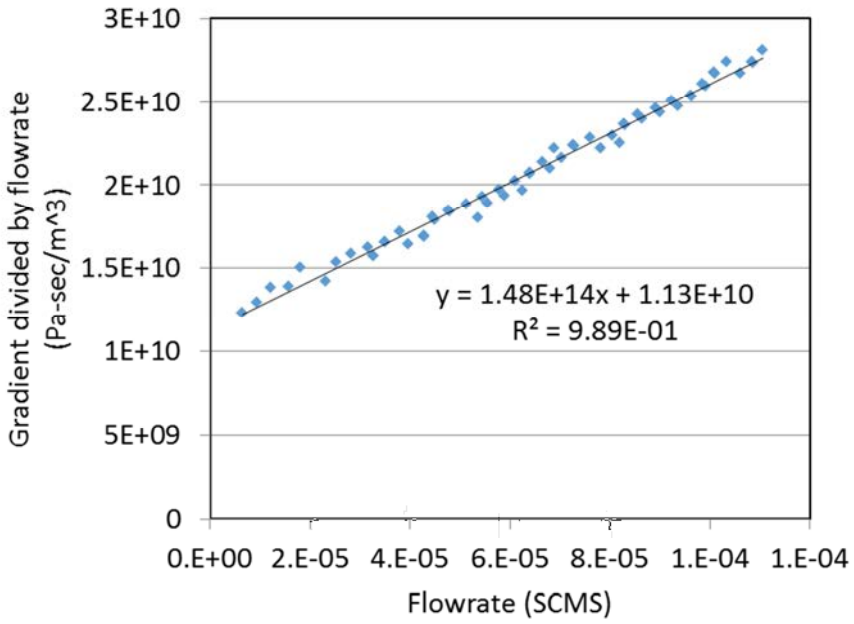

Fig. 3.13 – Analysis of non-linear flow for test on Sample 29 under 20.7 MPa confining pressure.

The specimens with flaws yielded flow rates that were more than 3 orders of magnitude greater than that for intact specimens (i.e., cement sheath on casing with no flaws) under comparable conditions. Interpreted as permeability, the intact specimen's permeabilities were on the order of 10^{-18} m^2 while permeabilities for specimens with microannuli were mostly in the range of 10^{-12} to 10^{-15} m^2. Flow was therefore assumed to occur only through the flaws, and the calculated permeability was interpreted as a hydraulic aperture (h) using the so-called cubic law

$$h^3 = \frac{12kA}{w} \qquad \textbf{(3.5)}$$

where w is the flaw width which for these tests is the outer circumference of the casing.

Gas slip effects were evaluated from data collected at different mean gas pressures and from data collected with different gases. In the tests reported here, the flow paths were sufficiently large that gas slip effects were not observed.

3.3 Testing results

3.3.1 Samples tested

A table of samples that have been tested are given in **Table 3.1** below. The designation LMA refers to a large microannulus, SMA refers to a small microannulus, and RF refers to radial fracture. These specimens were subjected to various values of confining and internal pressures while axial flow was measured. In some instances, the samples have been repaired and retested.

Numerous samples failed during curing, handling or testing and consequently are not included in this table. Early in the test program, some samples developed cracks at room conditions. Consequently, samples were subsequently kept in a humid environment except when tested. Samples failed for other reasons as well. If the samples were even slightly longer than the space between the two end-caps in the pressure vessel, they cracked due to the axial pressure of the end-caps on the sample. In addition, stress on the sample during installation or removal from the pressure vessel can cause cracks.

Table 3.1 – Samples tested with microannuli.

Sample number	Casing thickness (mm)	Microannulus type	Comments
1	3.75	LMA	
2	3.75	LMA	
6	3.75	RF	
15	3.75	LMA	Repaired with epoxy and retested
21	2.35	SMA	
22	3.75	SMA	
23	2.35	SMA	Repaired with epoxy and retested
24	3.75	SMA	Repaired epoxy and retested
29	2.35	LMA	
30	2.35	SMA	Corroded casing
33	3.75	SMA	
36	1.8	SMA	
38	1.5	LMA	
40	1.5	LMA	
41	1.5	LMA	
42	1.5	LMA	

43	1.5	LMA	
44	1.5	LMA	
48	2.35	LMA	Repaired with microfine and retested
49	2.35	LMA	Repaired with nanocomposite and retested
50	2.35	LMA	
51	2.35	LMA	
52	2.35	SMA	
55	2.35	LMA	Corroded casing
57	2.35	Intact	Corroded casing
58	2.35	LMA	
59	2.35	LMA	
60	2.35	LMA	
66	2.35	LMA	Low pressure testing and repair with nanocomposite

3.3.2 Testing of flaws

In this section, a description is given of tests that characterize the behavior of flaws that were induced in samples.

A summary of the relative performance of flawed samples is given in **Fig.3.14**. The two types of microannulus show a significant difference in flow rate; the large microannulus (formed by release film) has a flow rate that is orders of magnitude greater than that for the small microannulus (formed by cooling casing to cause it to debond from the cement). The flow through a slot flaw is given along with flow through a radial fracture in the wellbore cement. Also shown in this figure is the flow rate expected for an intact sample where flow is through the intact cement.

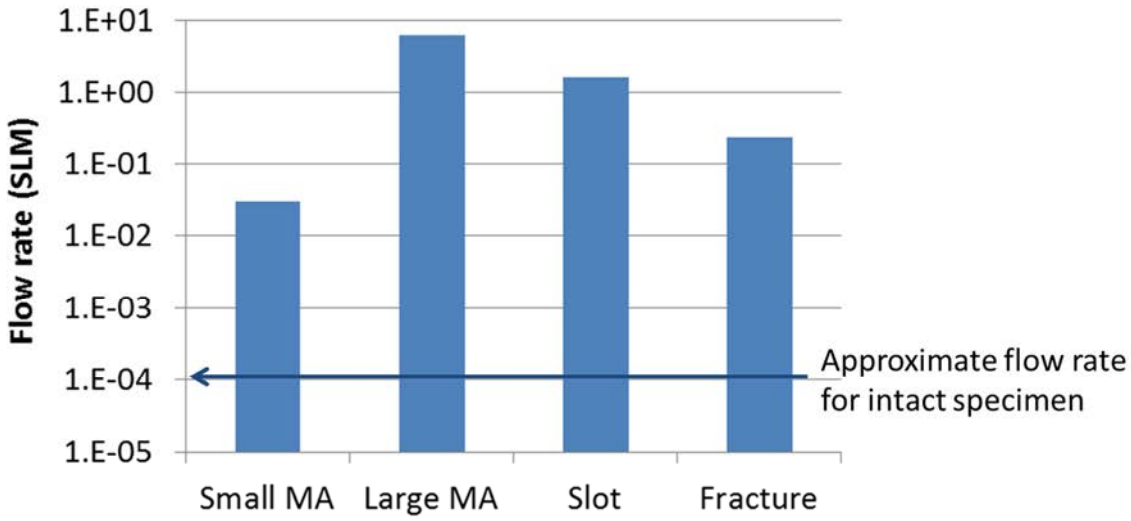

Fig. 3.14 – Flow rate through samples with representative seal system flaws. MA denotes microannulus. Microannulus is sample 11, large microannulus is sample 15, slot is sample 8, and cement fracture is sample 6.

Representative data and summaries of the performance of flawed samples are given in the remainder of this section.

3.3.2.1 Testing of radial flaw in sample

A number of specimens developed radial fractures in the cement sheath. The majority of the fractures were inadvertently produced while attempting to create a microannulus (by heating or cooling) or from not fitting perfectly within the pressure vessel.

Sample 6 – This sample was heat treated (casing was heated) and a visible radial cement fracture developed. The apparent permeability of the fractured system was measured as a function of confining pressure (**Fig. 3.15**). These results reveal the fracture deformability and corresponding permeability changes of the fracture as a function of the confining stress. The hydraulic aperture was largely insensitive to changes in the casing pressure.

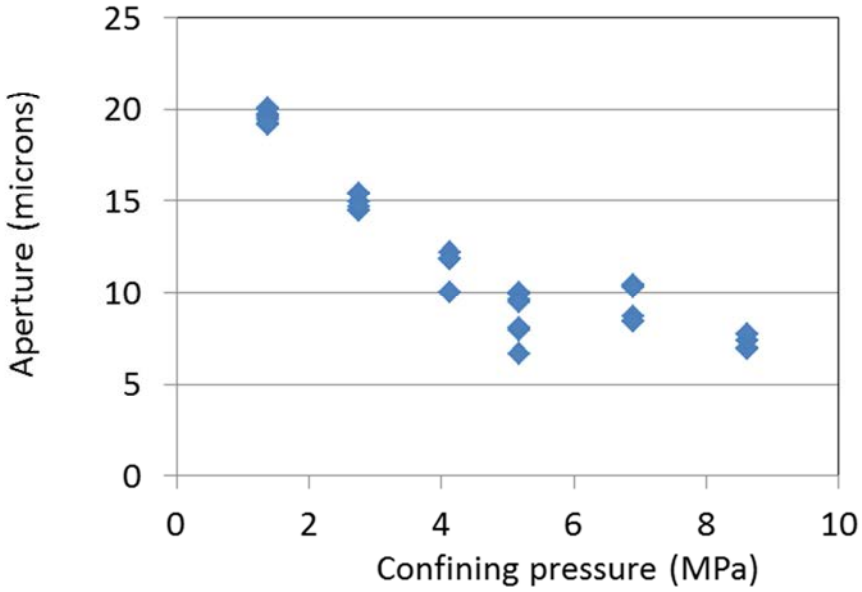

Fig. 3.15 – Hydraulic aperture of sample 6 as a function of confining pressure.

3.3.2.2 Slot flow

Sample 8 was the single sample that was tested with a slot flaw. We did not test additional slot samples because the flaws were so large that they did not challenge the ability of the repair material to penetrate the slot. In this test, a flow rate of 1.63 L/min was measured at 0.17 MPa gas driving pressure, 0.69 MPa confining pressure, and 0.69 MPa internal casing pressure.

3.3.2.3 Small microannulus

Hydraulic apertures as a function of confining pressure for tests on a number of samples with small microannuli are shown in **Fig.3.16**. **Sample 30** was a sample that had a corroded casing.

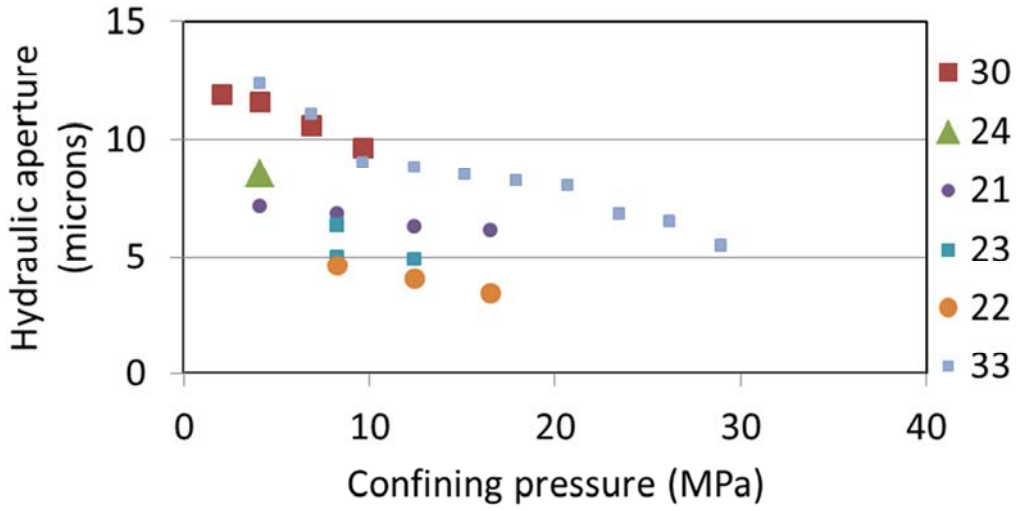

Fig. 3.16 – Hydraulic aperture interpreted from flow measurements as a function of confining pressure for samples with small microannuli.

Sample 52 was tested with more loading and unloading cycles compared to previous samples. In response to the application of large confining pressures, the hydraulic aperture decreases and does not recover (**Fig.3.17)** upon unloading. In fact, the interpreted hydraulic radii are about equivalent to the flow expected for intact cement. This result suggests that the microannulus has completely shut down.

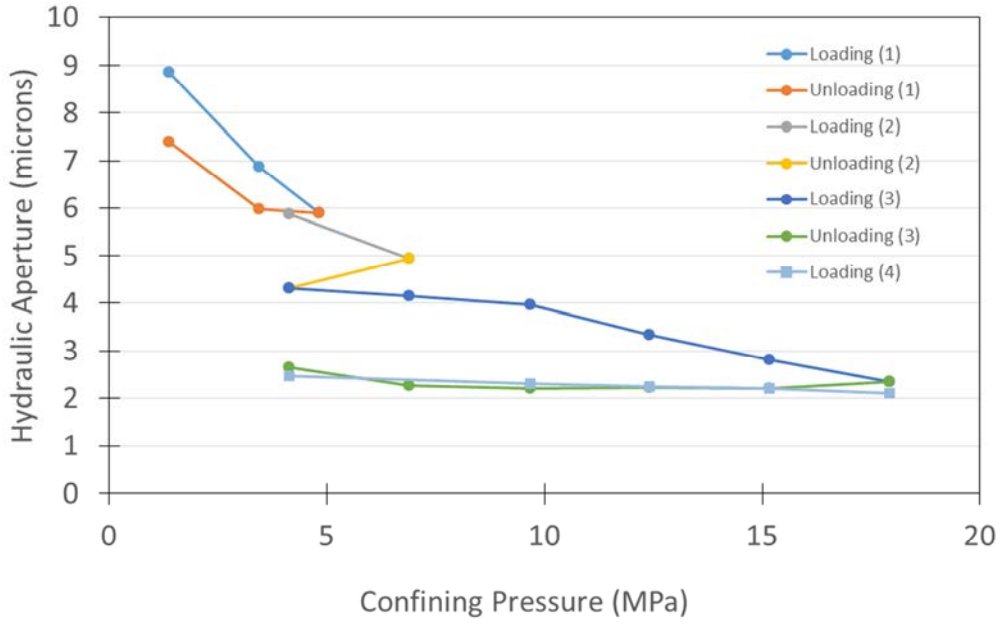

Fig. 3.17 – Hydraulic aperture vs. confining pressure on sample 52 (small microannulus).

3.3.2.4 Large microannulus

Hydraulic apertures as a function of confining pressure are shown in **Fig. 3.18** for **Sample 48**. This sample had a large microannulus, and the computed hydraulic aperture is large. To further investigate the response of the microannulus to cyclic stresses, sample 48 was subjected to confining pressures which were cycled 30 times between 6.9 to 20.7 MPa (**Fig. 3.19**). Very little change was seen in the hydraulic aperture after 30 cycles suggesting little additional damage or degradation occurred.

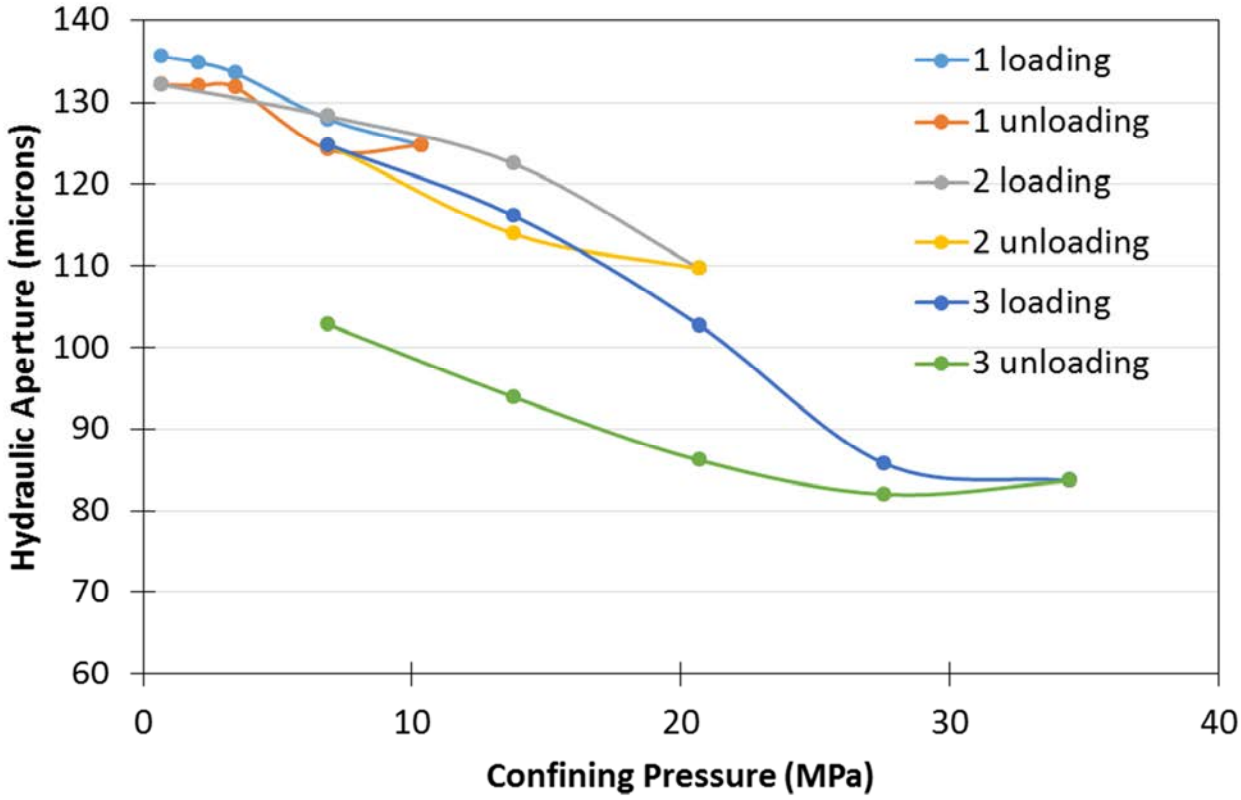

Fig. 3.18 – Hydraulic aperture interpreted from flow measurements as a function of confining pressure for Sample 48.

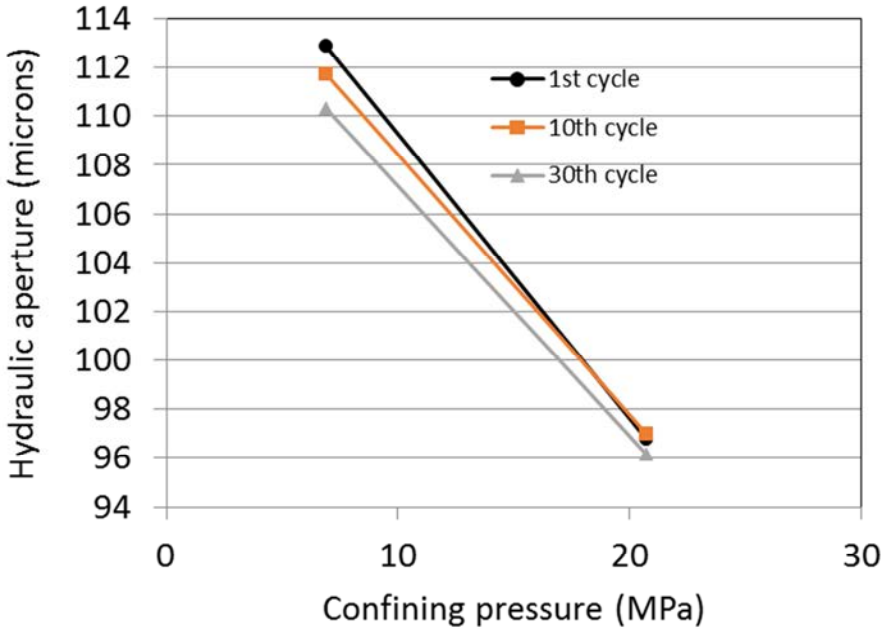

Fig. 3.19 - Hydraulic aperture as a function of confining pressure for 1st, 10th, and 30th cycle of stress varying from 6.9 to 20.7 MPa (sample 48).

Sample 51 was subjected to 9 confining pressure cycles up to 35 MPa with concurrent flow measurements. In **Fig. 3.20**, hydraulic aperture data are given for every other loading-unloading cycle. These results are consistent with other results on large microannulus samples; namely, that the hydraulic aperture largely recovers when confining stress is reduced, and the response is repeatable over numerous stress cycles. In addition, there is often some hysteresis in the hydraulic aperture for a particular loading-unloading cycle.

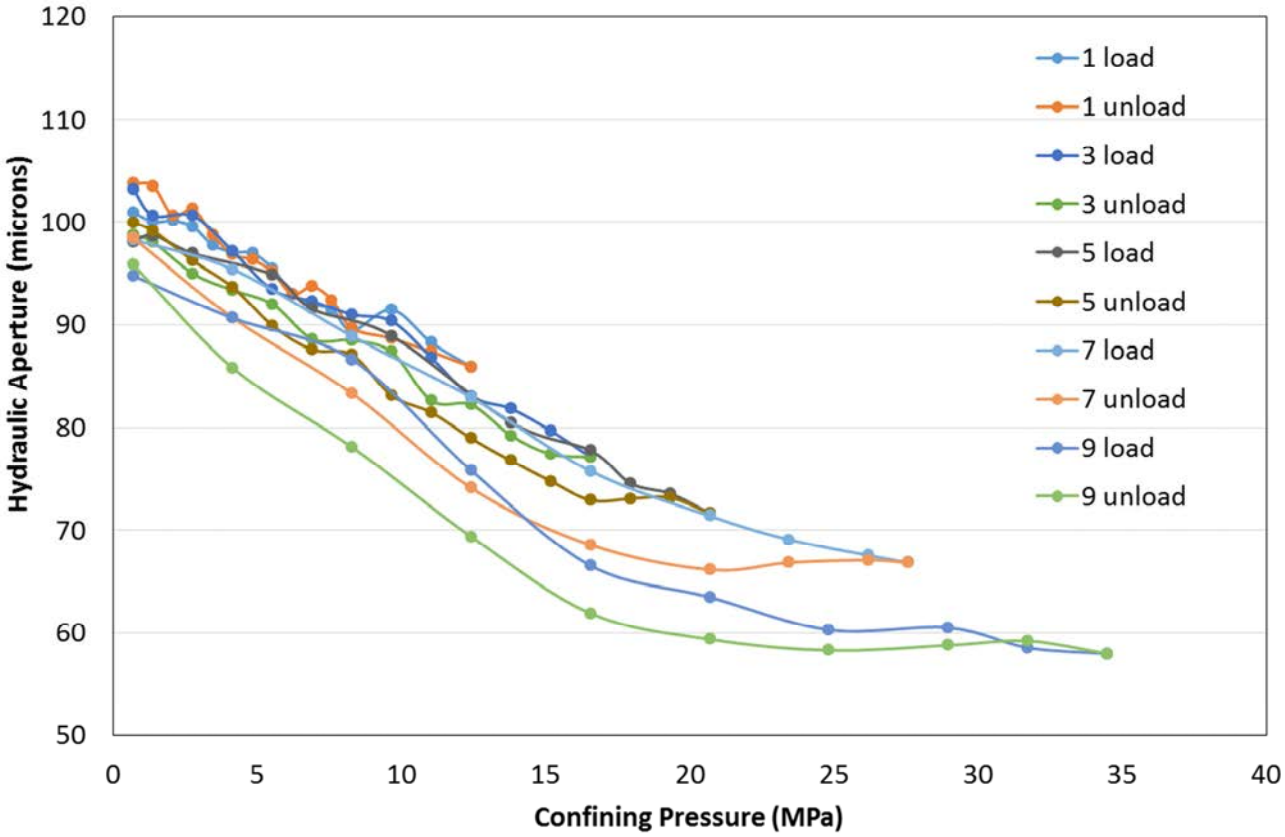

Fig. 3.20 – Hydraulic aperture interpreted from flow measurements as a function of confining pressure for Sample 51.

Hydraulic apertures as a function of confining pressure are shown in **Fig. 3.21** for Sample 29. This sample was tested two separate times. Results from the initial testing are shown in **Fig.3.21** with solid circles and connected by solid lines. After the initial testing, the sample was removed from the pressure vessel; the casing could still be easily removed and replaced. The specimen was placed back in the pressure vessel and retested. These results are shown in figure with open squares connected with a dashed line. The initial hydraulic aperture was somewhat larger than during the initial test. With increasing confining pressure and during unloading, the hydraulic apertures are similar to those from the initial testing.

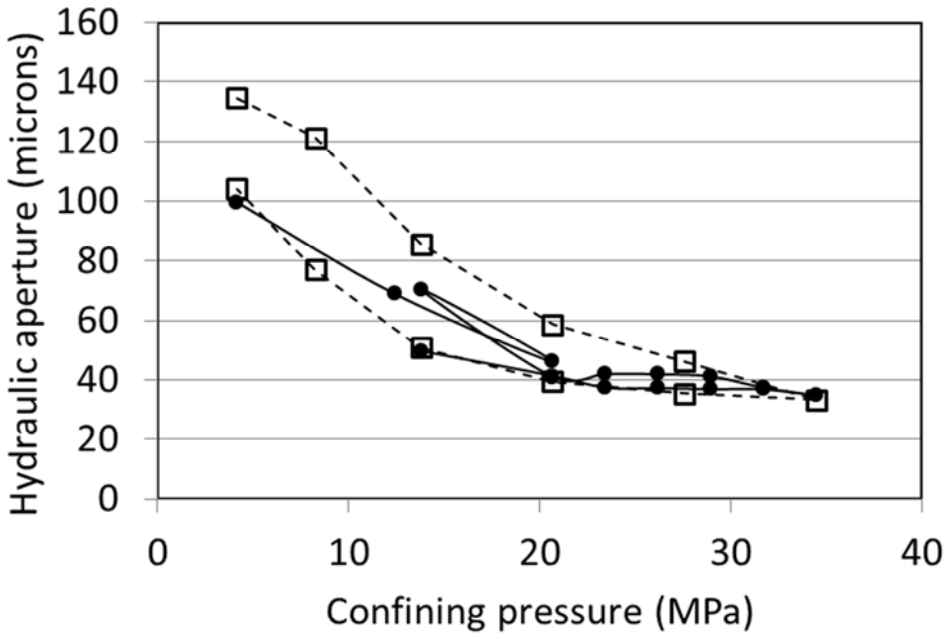

Fig. 3.21 – Hydraulic aperture interpreted from flow measurements as a function of confining pressure for Sample 29.

3.3.2.5 Testing focused on response to casing pressure

The hydraulic aperture as a function of internal pressure changes in **Sample 29** (large microannulus) is shown in **Fig. 3.22**. The first episode of internal casing pressure changes happened after the sample had experienced confining pressures as great as 20 MPa. The second episode occurred after the confining pressure had been as great as 35 MPa. In both cases, the confining pressure was 13.8 MPa during the conduct of the test with varying internal pressure.

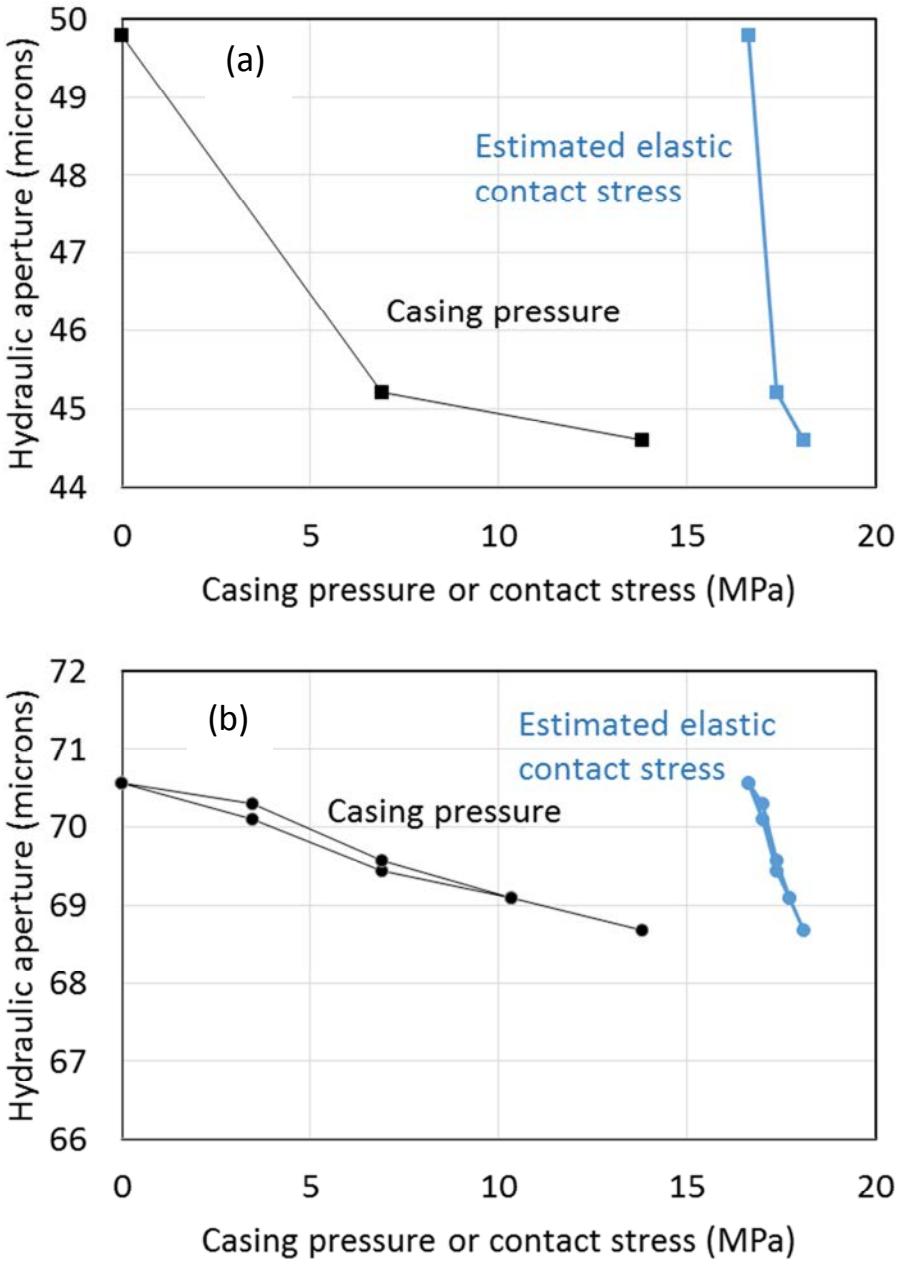

Fig. 3.22 - Hydraulic aperture as a function of casing pressure (black symbols) and calculated elastic contact stress (blue symbols) for test conducted at confining pressure of 14 MPa during (a) initial loading, and (b) unloading path.

The change in hydraulic aperture in response to the change in casing pressure is shown in **Fig. 3.22**. Compared to changes in confining pressure, the hydraulic aperture is much less sensitive to changes in casing pressure largely because of the relative stiffness of the steel compared to that of the cement. An alternative way to present these results is in terms of the elastic contact

stress, which is the radial stress at the cement-casing interface calculated from an elastic solution for a bi-material hollow cylinder (Ugwu, 2008). While the elastic solution assumes the cement and steel are bonded and thus does not explicitly account for a discrete microannulus, it provides a first-order estimate of stresses that develop in the vicinity of the microannulus for the wellbore configuration. The contact stress was calculated for the geometry and material properties for the specimen as a function of the applied confining and internal casing pressures. When the hydraulic aperture results are given in this form, they reveal that the casing pressure changes produce relatively small changes in the calculated elastic stress across the cement-casing interface compared to those produced from comparable confining pressure changes. While insightful, the elastic solution is limited in terms of describing microannulus behavior: even when results are presented in terms of elastic contact stress, the rate of change of the hydraulic aperture in response to casing pressure changes is less than that for confining pressure changes.

The results above indicate that tests performed at high confining pressures (>10 MPa) and casing pressures lower than the confining pressure produce little effect of casing pressure on flow. **Sample 60** was a sample with a large microannulus that was tested at lower confining pressures (5.5 MPa) and higher confining pressures (13.8 MPa). Results from these tests are shown in **Fig.3.23**. At a lower confining pressure, the hydraulic aperture changes significantly more as the internal casing pressure varies.

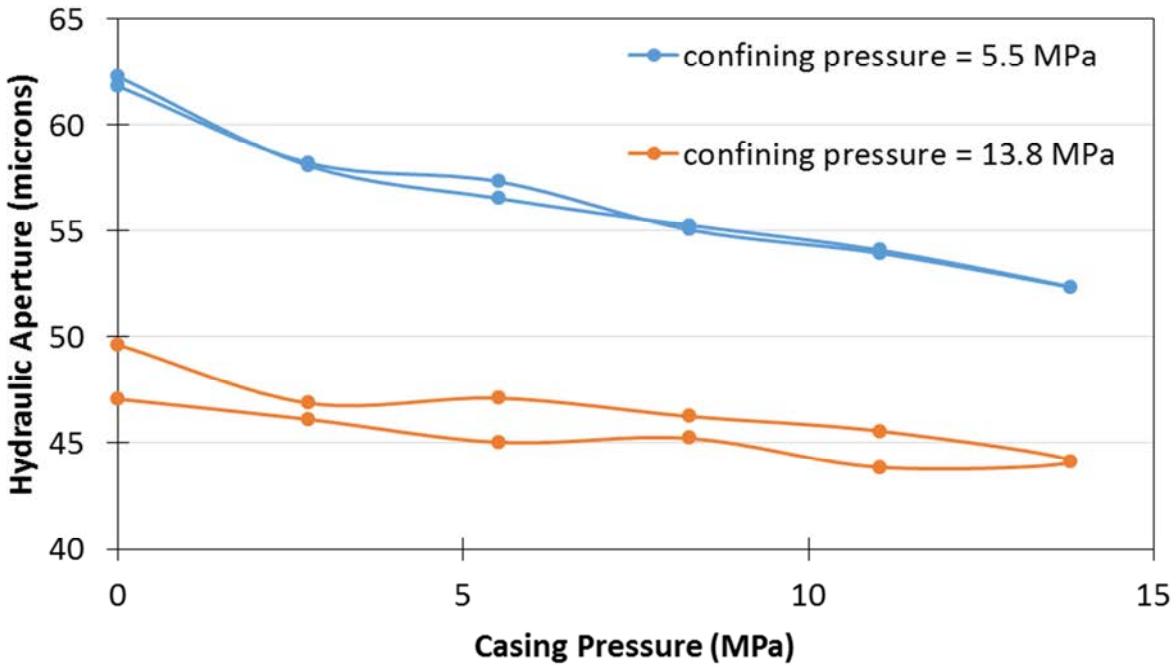

Fig.3.23 – Hydraulic aperture vs. casing pressure for large microannulus at different confining pressures (sample 60).

It is possible to damage the cement sheath with an excessive internal casing pressure. In **Fig. 3.24**, the response of the hydraulic aperture interpreted from flow data is shown during tests on **Sample 23** where the internal casing pressure was changed at two different values of confining pressure. The results are given in terms of the elastic circumferential stress, which is the circumferential stress in the cement adjacent to the cement – casing interface calculated using the bi-material hollow cylinder elastic solution (Ugwu, 2008). For the tests at both confining pressures, the casing pressure was increased above the confining pressure. The significant increase in hydraulic aperture for the specimen tested at a confining pressure of 4.1 MPa coincides with the calculated elastic circumferential stress becoming negative, suggesting that the cement may have failed in tension. A fracture in the cement was observed upon removing the specimen from the pressure vessel.

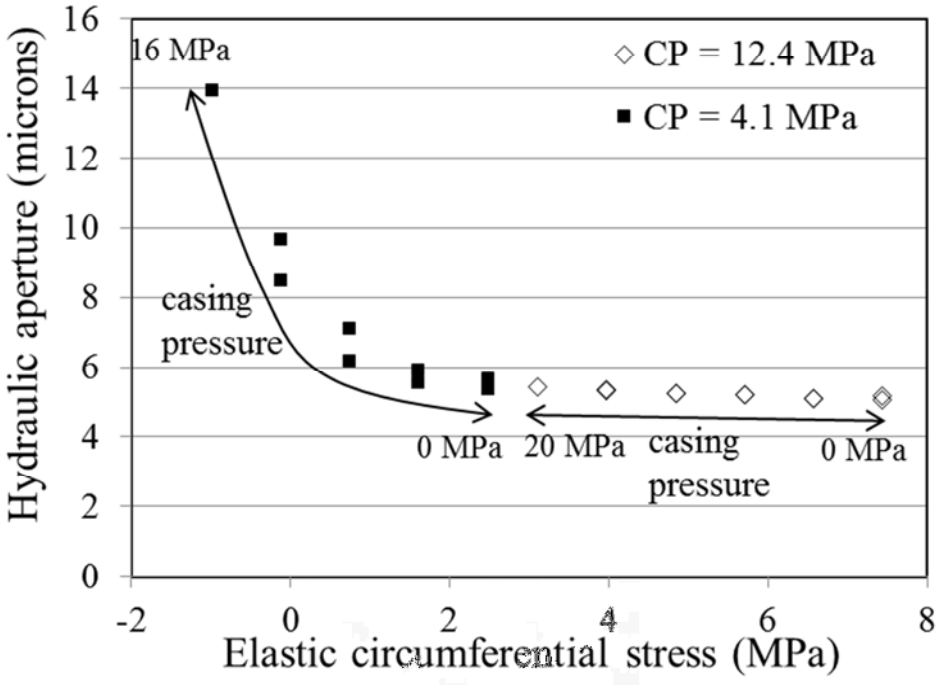

Fig. 3.24– Hydraulic aperture as a function of calculated elastic circumferential stress. Confining pressure (CP) was held constant and casing pressure varied during these tests.

3.3.2.6 Testing focused on response to pore pressure

The impact of pore pressure on flow through the microannulus has largely been inconclusive in part due to the accuracy and resolution of the flow meters that are used. Since the flows are high (non-Darcy), multiple measurements are taken for Forchheimer analysis for each permeability value. At higher pore pressures, the rotameters used may not have the resolution for accurate calculation. One test that produced reasonable results in shown in **Fig.3.25.** In this figure, the hydraulic aperture is given as a function of effective pressure (defined here as confining pressure - pore pressure) from the test on **Sample 58**. Confining pressure was first increased to 3.4 MPa with a pore pressure near zero (blue line). Confining pressure and pore pressure were then simultaneously increased to 6.9 MPa and 3.5 MPa, respectively, to keep an effective stress of 3.5 MPa (first orange point). Pore pressure was then progressively decreased to 0 MPa which results in a final effective stress of 6.9 MPa. On this stress path (the orange line), the hydraulic aperture is seen to decrease in a response to a decrease in the pore pressure. The final series of measurements (gray line) were made at a zero pore pressure. Taken together, these results indicated that the changes in hydraulic aperture caused by varying the pore pressure are consistent with those induced by changes in confining pressure.

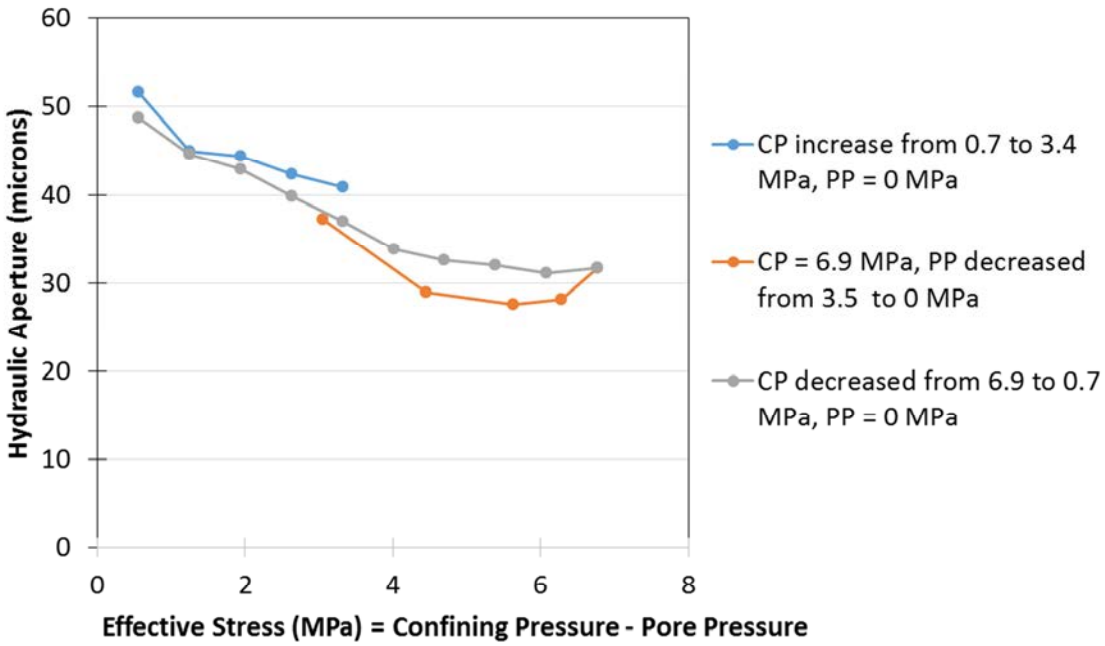

Fig.3.25 – Hydraulic aperture vs. effective stress for test on sample with large microannulus (sample 58).

3.3.2.7 Testing on a sample with corroded casing

Some samples were made with corroded steel casings. Results from **Sample 55** are shown in **Fig.3.26**. Flow through this sample corresponded to a hydraulic aperture of more than 20 microns, even after loading and unloading the sample. These results are of the same magnitude as **Sample 30** which is included in **Fig.3.16**.

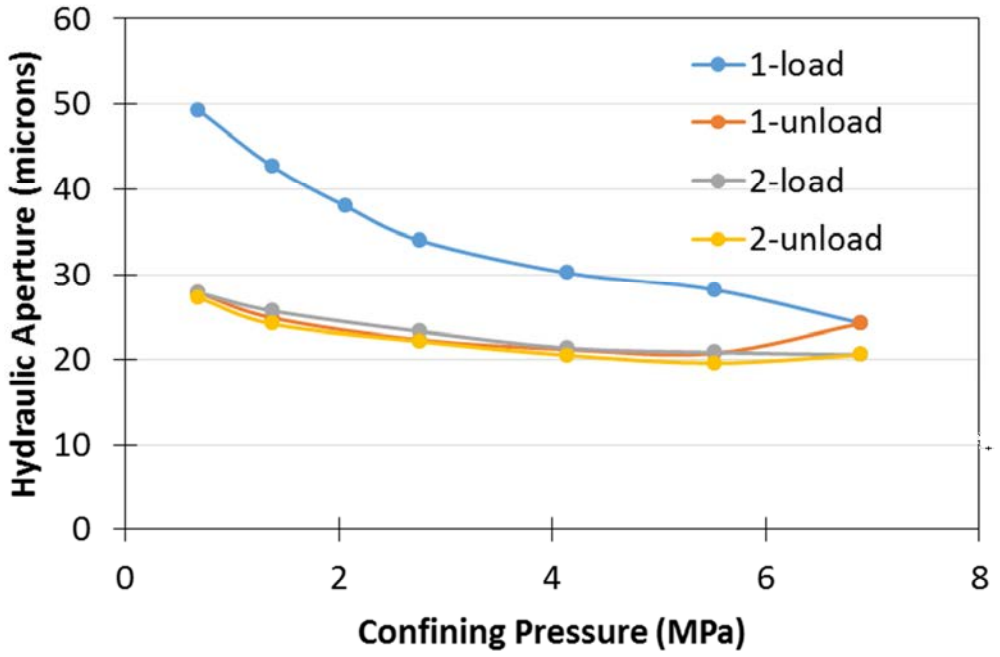

Fig.3.26 – Hydraulic aperture vs. confining pressure for test on sample with corroded casing (sample 55).

Different results were obtained from **Sample 57** which was also constructed with a corroded casing. Results from testing are shown in **Fig.3.27.** At lower confining pressure (0.7 MPa), the sample had an interpreted hydraulic aperture that is greater than that of an intact cement sample. The hydraulic aperture decreased to that of an intact non-corroded sample when confining pressure was taken to 20 MPa. The hydraulic aperture did not significantly change after confining pressure was lowered to 0.7 MPa and subsequently increased back to 20 MPa.

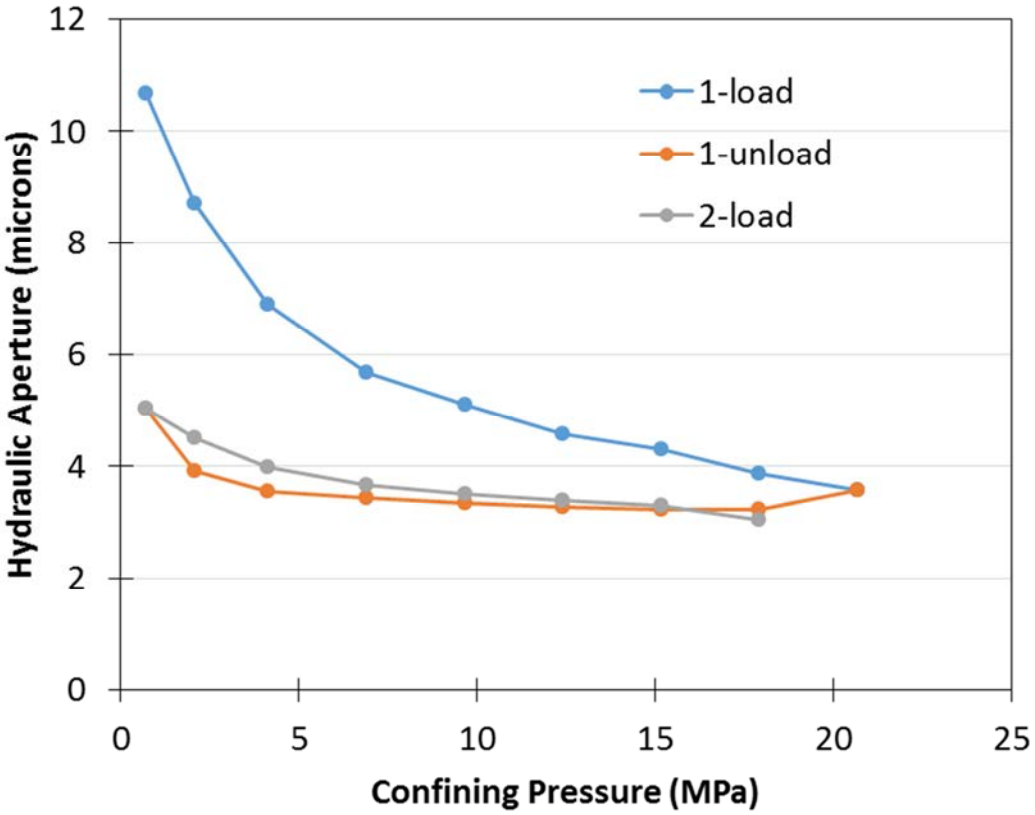

Fig.3.27 – Hydraulic aperture vs. confining pressure for test on sample with corroded casing (sample 57).

3.3.3 Testing of repaired wellbore seal systems

3.3.3.1 Testing of repaired sample with radial fracture

Sample 7 included a radial fracture. After the flow through the seal system was initially tested, the fracture was repaired with the nanocomposite base epoxy (novolac) on two separate occasions. Results are summarized in **Fig. 3.28** and **Fig. 3.29** in terms of hydraulic aperture and the permeability, respectively. Recall that hydraulic aperture and permeability are simply different ways of expressing the flow through the wellbore sample, and are related to one another by Equation 5. Initially, the flow through the system corresponds to a large hydraulic aperture and permeability. The first repair effort substantially reduced flow through the system; the hydraulic aperture decreased by a factor of about 7 and the permeability decreased by more than two orders of magnitude. The second repair results in a hydraulic aperture and permeability that are close to that of intact cement.

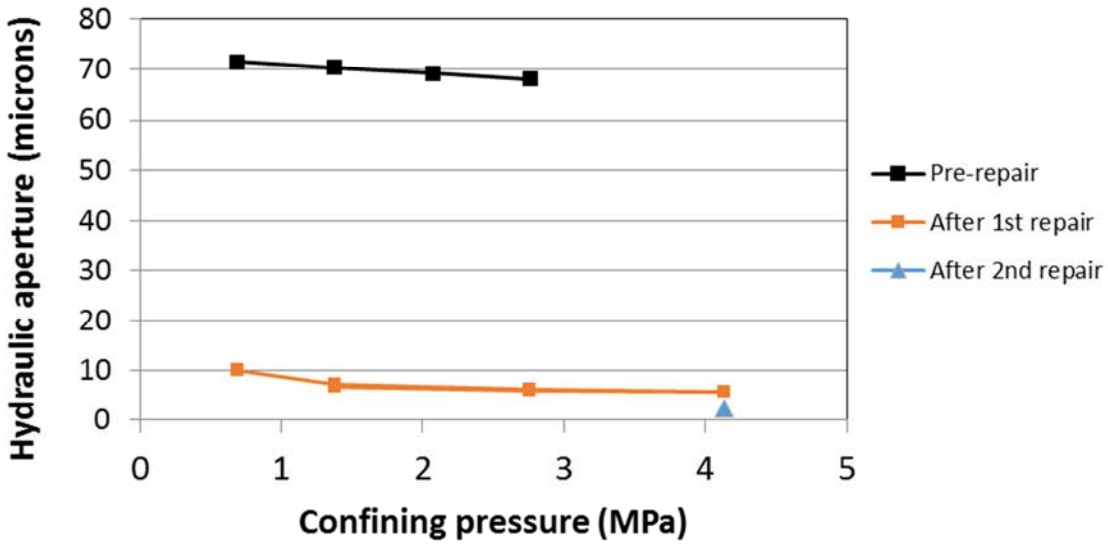

Fig. 3.28 – Hydraulic aperture as a function of confining pressure for sample 7 (radial fracture) before and after repair.

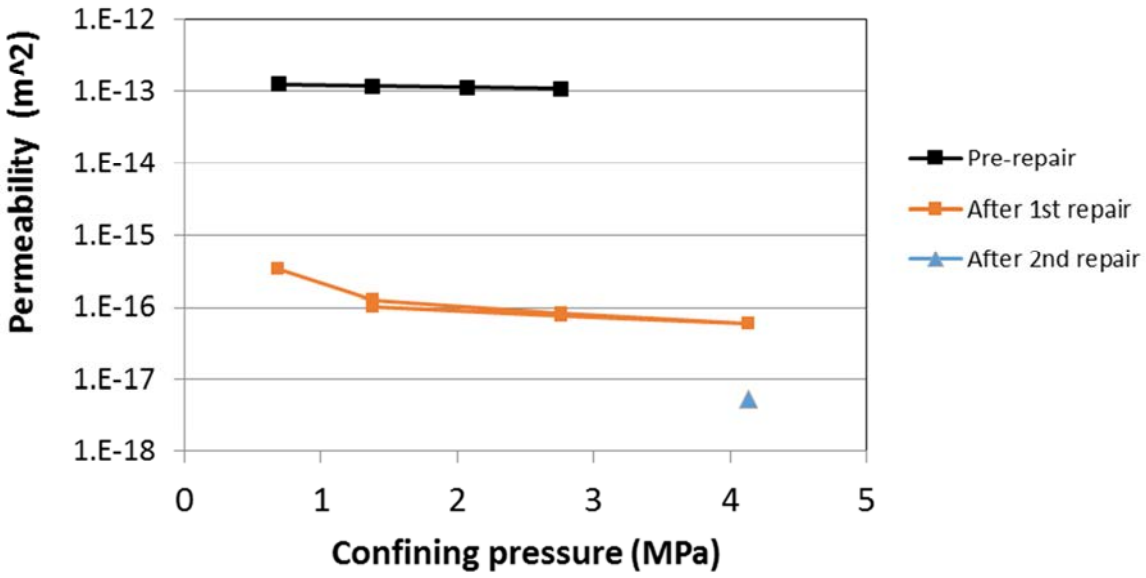

Fig. 3.29 – Permeability vs. confining pressure for sample 7 (radial fracture) before and after repair.

3.3.3.2 Testing of repaired sample with small microannulus

Sample 23, which had a small microannulus, utilized the "epoxy capsule" to inject repair material into the microannulus (**Fig. 3.11**). After removing the sample from the pressure vessel, the nanocomposite base epoxy was placed on top of the sample which was then pressurized to 70 kPa. Note: the epoxy did not apparently penetrate into the microannulus prior to pressurization. Pre- and post-repair testing was conducted with a confining pressure of 4.1 MPa and a pore pressure of 0.7 MPa; after repair, the permeability of the repaired system was reduced by more than 3 orders of magnitude as shown in **Fig. 3.30**.

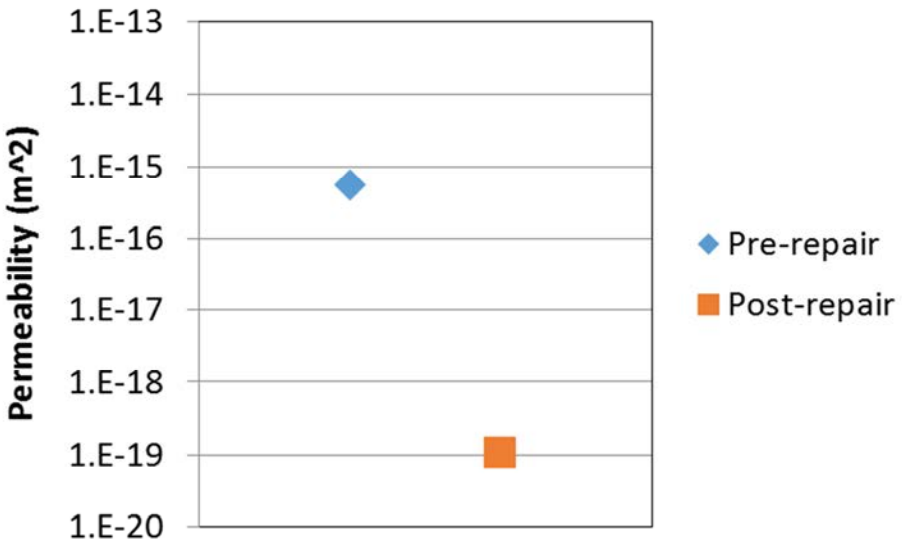

Fig. 3.30 – Permeability reduction due to repair for sample 23.

Sample 24 had a port inside the casing (**Fig. 3.12**) the purpose of the port was to allow injection of the epoxy into the microannulus while the sample was under confining pressure. The sample was first tested to obtain a baseline permeability. After opening one end of the vessel, the tube coming out of the port inside the casing was filled with epoxy and shut. After putting end cap back on, a confining pressure of 4.1 MPa was applied and casing pressure was increased to 1 MPa to allow the casing pressure to squeeze the tube and push epoxy into the microannulus through the port. After 12 minutes, the pressure was released and the vessel opened. When the sample was tested again after 24 hours, no reduction in permeability was seen, indicating little or no injection of epoxy into the microannulus. This method of injecting repair material was not pursued further.

3.3.3.3 Testing of repaired sample with large microannulus

Sample 15 was produced with a large microannulus. After initial flow testing, it was repaired with the nanocomposite base epoxy (novolac). The repair was accomplished by removing the sample from the vessel, and the epoxy was simply applied to the top of the sample and allowed to flow by gravity into the microannulus. The large microannulus readily accepted the epoxy. The sample was placed back in the pressure vessel and retested. The before and after flow rates were measured under comparable conditions - a confining pressure of 1.4 MPa, an internal

pressure of 1.4 MPa and a gas pressure of 0.7 MPa. Results are shown in **Fig. 3.31** in terms of permeability. A dramatic decrease in flow through the seal system is achieved by the repair, corresponding to a decrease of permeability of 7 orders of magnitude. The final condition after repair had a non-detectable flow rate under the experimental condition, and the given value represents the maximum possible value.

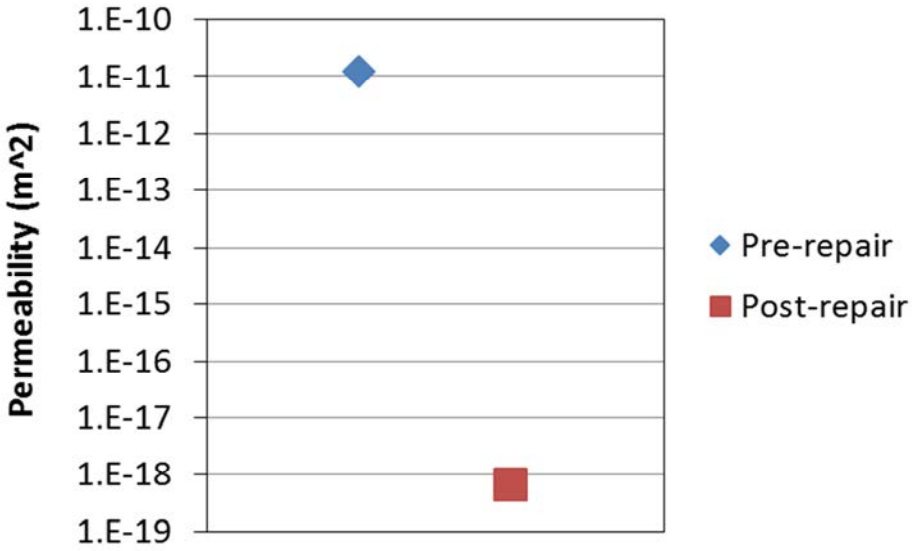

Fig. 3.31– Permeabilities of sample 15 before and after repair.

Sample 48 was repaired with microfine cement using MC-500 Microfine cement mixed with a 0.7 water/cement ratio and 1% superplasticizer. The mix was chosen to obtain the highest strength but still keep it inviscid enough to inject in to the fracture. It was injected into the microannulus with a syringe. After 7 days, the sample was re-tested. Results are summarized in **Fig. 3.32**. Prior to repair, the sample had a hydraulic aperture on the order of 120 microns. Post-repair, the calculated hydraulic aperture of the system initially decreased by approximately 50%. The sample was then loaded to 16.6 MPa confining pressure, and the hydraulic aperture decreased to less than 30 microns. Upon unloading the pressure, the hydraulic aperture increased above that measured before loading, and despite re-loading, it remained at an increased hydraulic aperture of about 80 microns. These results suggest a degradation of the repair by de-bonding between the steel casing, microfine cement, and the cement sheath. When the sample was removed from the pressure vessel, it was seen that the steel casing had completely de-bonded

from the cement sheath and was loose in the sample. In addition, some cement powder was produced from the sample.

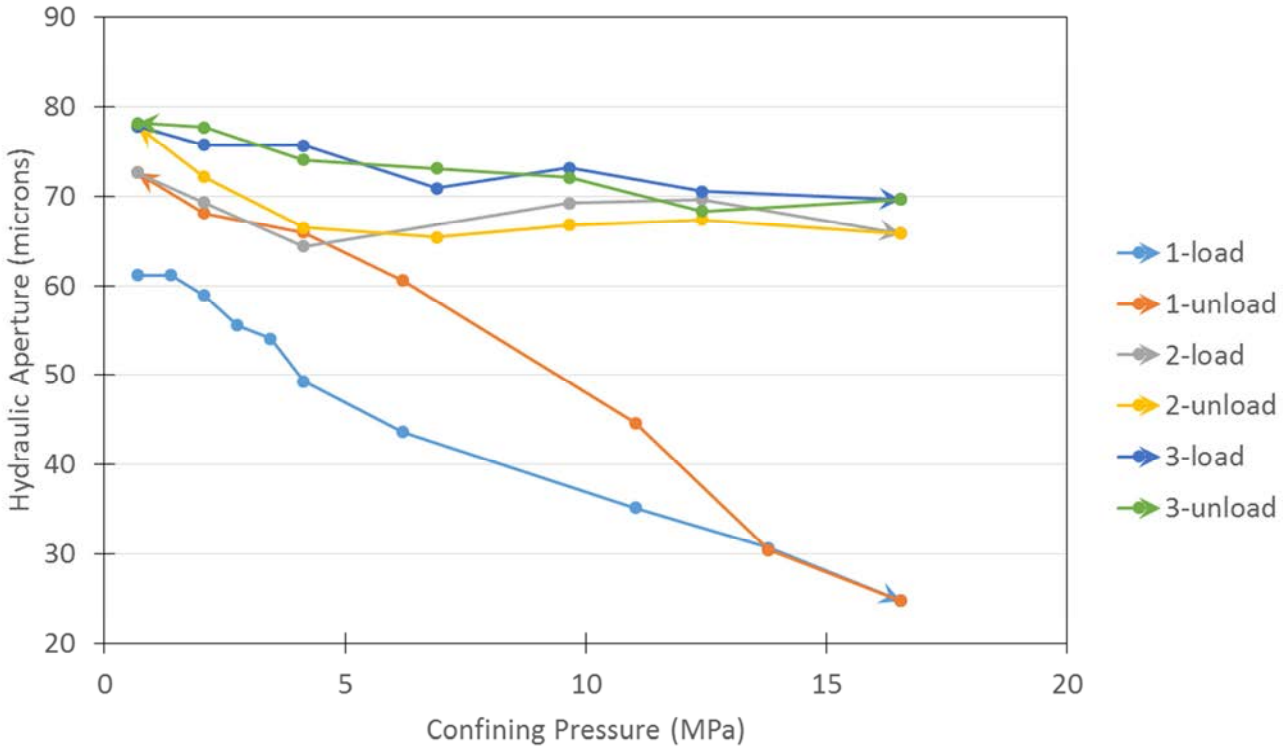

Fig. 3.32– Post-repair hydraulic aperture on sample 48 which was repaired with microfine cement.

Sample 49 was repaired with the nanocomposite base epoxy. Prior to repair, the sample had a hydraulic aperture on the order of 200 microns. After repair, the hydraulic aperture was dramatically reduced (**Fig. 3.33**). After the initial loading, the hydraulic aperture remained very low and consistent with the value for an intact sample.

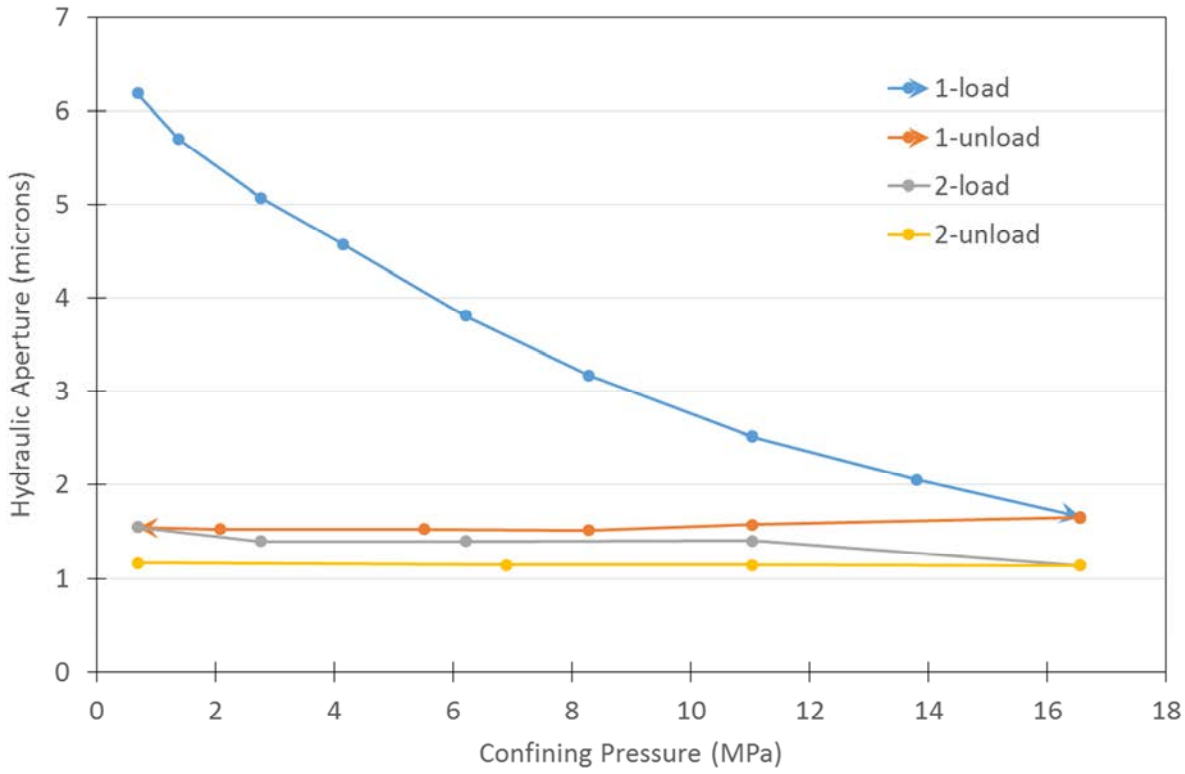

Fig. 3.33 – Post-repair hydraulic aperture on sample 49 which was repaired with nanocomposite base epoxy.

The data from the two tests are combined in **Fig. 3.34**. Here, the data are given in terms of permeability for the pre-repair, post-repair, and after one and two stress cycles. This figure reveals the dramatic difference in performance of the samples repaired with nanocomposite base epoxy and microfine cement.

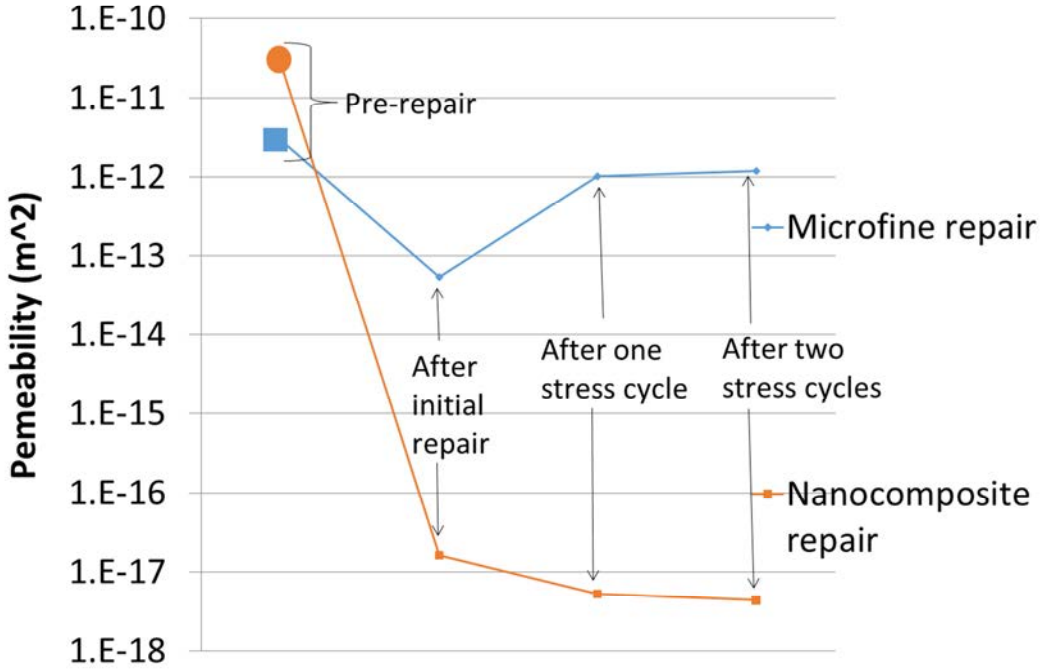

Fig.3.34 – Summary of tests on comparable samples repair with microfine (blue) and nanocomposite base epoxy (orange).

Sample 48 and 49 were cut to see how far along the length of the sample the epoxy or microfine cement had flowed in. Each sample was cut into 6 sections or disks. Images of the sections were taken under an optical microscope. **Fig. 3.35** is a photomicrograph of the middle section of the sample and **Fig. 3.36** is of the bottom section of the sample. It can be seen that the epoxy has flowed through to the other end of the sample and filled most of the microannulus. In contrast, the sample repaired with microfine cement repair (**Fig. 3.37**) indicates incomplete filling of the microannulus.

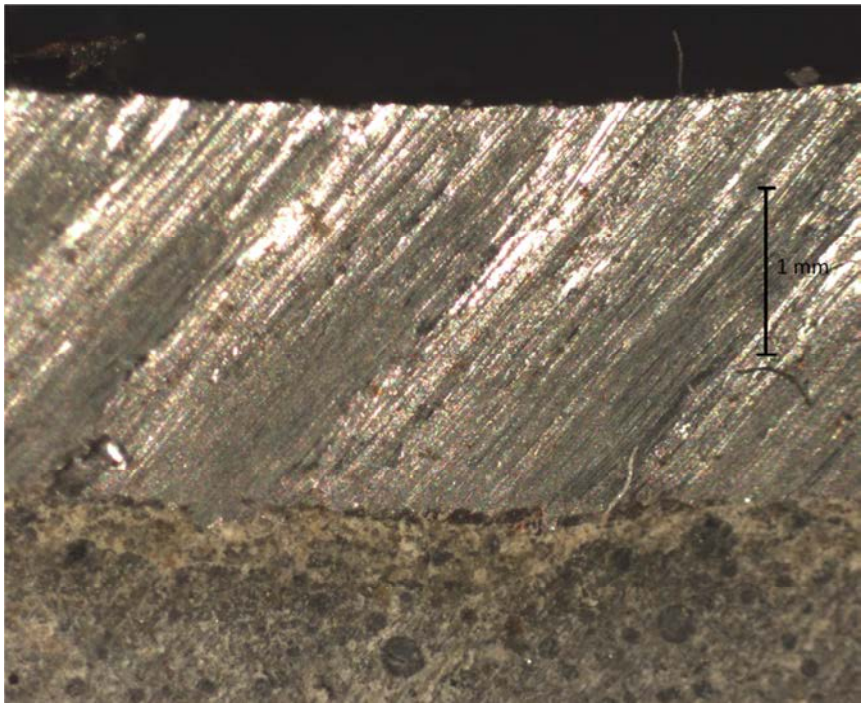

Fig. 3.35 - Microphotograph of casing – cement contact in middle of sample repaired with epoxy.

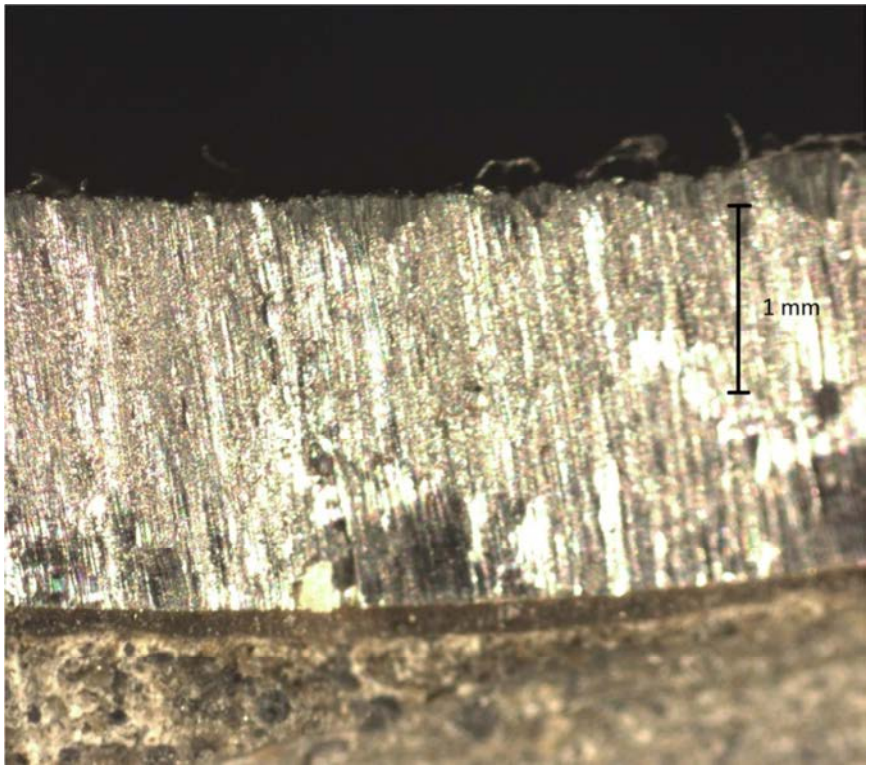

Fig. 3.36 - Microphotograph of casing – cement contact near bottom of sample repaired with epoxy.

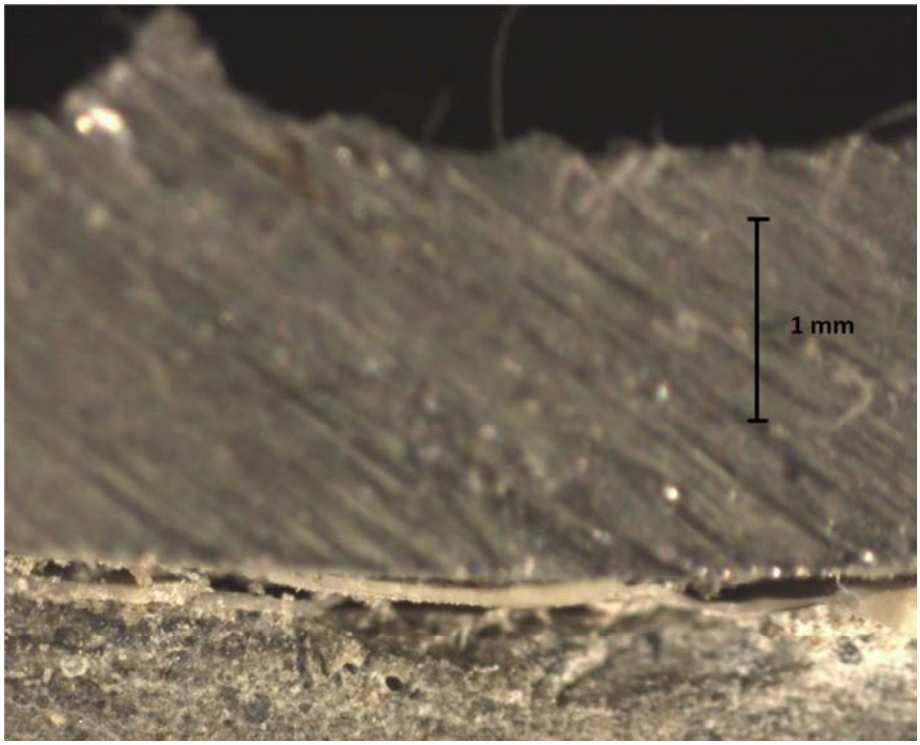

Fig. 3.37 - Microphotograph of casing – cement contact of sample repaired with microfine cement.

Sample 66 was a large microannulus sample that had a pre-repair hydraulic aperture of 175 microns when tested at a minimal confining pressure of 0.1 MPa. This sample was repaired using a nanocomposite base epoxy in which Rhodamine B was added. Rhodamine B is a bright pink dye that also is fluorescent, which provides contrasts in both visible and UV light. The post-repair hydraulic aperture was consistent with an intact sample, indicating complete repair.

We developed a procedure to measure the epoxy-filled aperture using image processing methods. Post-repair, the sample was sectioned (**Fig. 3.38**) and the mechanical aperture as a function of the circumferential length was measured on each section using microphotographs such as shown in **Fig 3.39**. This figure reveals the striking effect of using this dye in the epoxy.

Fig.3.38: Sample 66 after repair with dyed epoxy and sectioning.

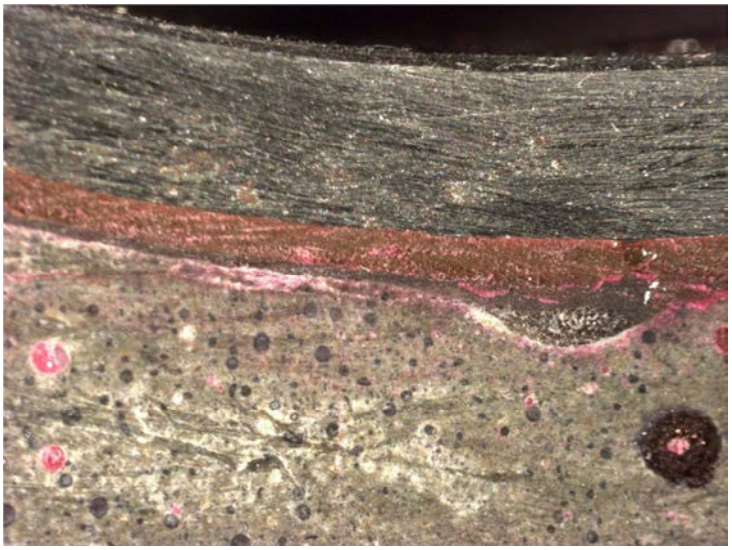

Fig.3.39: Sample 66 repaired with Epoxy and Rhodamine B

For each section, a complete description of the aperture vs. circumferential distance is obtained. An example is given in **Fig. 3.40** below.

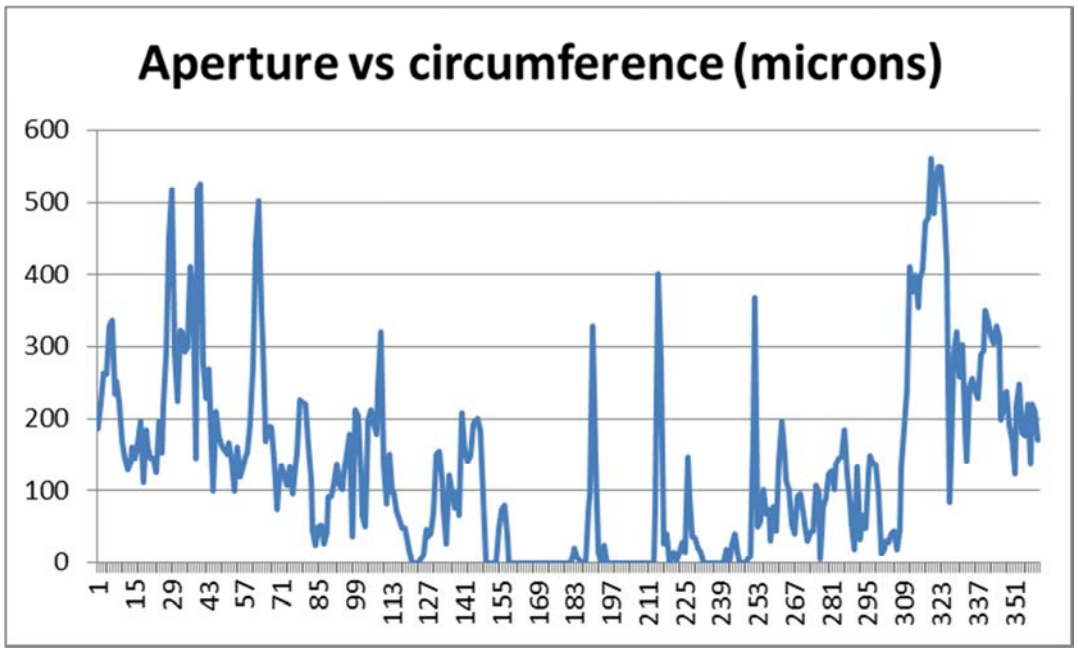

Fig. 3.40 – Aperture vs. circumference distance expressed as arc angle on the bottom of section 2 from Sample 66.

These images and data reveal that the repair epoxy completely penetrates a wide range of aperture sizes, from 100's to a few microns. The data also reveal that the casing and cement are in contact over a portion of the circumference.

In **Table 3.2** below, the data are summarized for 7 sections. The mechanical aperture is the arithmetic average value for each section. The hydraulic aperture h for each section is found from applying the cubic law incrementally around the circumference.

$$h = \sqrt[3]{\sum(h_i^3)} \qquad \textbf{(3.6)}$$

The average value of the hydraulic radius for the entire sample is found by using an averaging approach for series flow, and assuming each has equal weight yields an average value of 252 microns.

The hydraulic apertures interpreted from the image analysis are consistent with the value interpreted from the flow test. That value, 180 microns, assumes that the aperture is extends along the entire circumference. The imaging data indicate that about 20% of the circumference is not involved in the flow as the cement and steel are in full contact over that amount of the circumference. If we interpreted the flow data as occurring over 80% of the circumference, the hydraulic aperture from the flow data would be around 220 microns, which compares well with the average value of 252 microns from the image analysis.

Table 3.2 – Summary of image analyses of sample 66.

Slice	% Contact	Mechanical Aperture (microns)	Hydraulic Aperture (microns)
66.1.b	1.4	256.83	355.58
66.2.a	16.4	229.04	329.27
66.2.b	18.61	162.78	225.10
66.3a	16.94	200.50	257.79
66.3.b	22.22	153.32	201.20
66.4.a	21.39	195.24	244.75
66.4.b	18.61	175.65	244.18

3.4 Discussion and Summary

We have developed an experimental system to test wellbore specimens which are comprised of a cement sheath cast on a steel casing. The system allows independent application of confining pressures to 35 MPa and casing pressures to 20 MPa while gas flow is measured through the specimens along the wellbore axis.

Wellbore specimens were created with various flaws, including cement fractures and microannuli between the steel casing and the cement. We interpreted the hydraulic aperture of the flaws from gas flow measurements; we found from post-test measurements that the hydraulic aperture compares well with the average actual (mechanical) aperture. The size (hydraulic aperture) of the microannuli ranged from less than 10 μm to more than 100 μm. This range is relevant to the range of concern for wellbores; Seidel and Greene (1985) state that a microannulus of 25 μm is sufficient to problematic for gas flow along a well. Checkai et al. (2013) interpreted permeabilities from gas leakage and pressure build up records for over 200 leaky wellbores. Most of leaky wellbores had permeabilities that were on the order of 2 orders of magnitude greater than intact cement – this would correspond to microannuli of up to approximately 200 μm.

We used thermal transients induced by cooling and heating the casing to produce flaws in the wellbore samples. This result is consistent with suggestion that temperature changes within a casing can affect the integrity of a wellbore (e.g., Lavrov et al., 2015). Samples with small microannuli were generated by cooling the central casing with dry ice – the contraction of the casing was sufficient to de-bond the cement-steel interface. In some cases, the cement would develop fractures from cooling of the interior of the casing. Heating the casing generally fractured the cement sheath.

Testing wellbore samples with flaws revealed that flaws are capable of transmitting large amounts of flow. The flow rate through samples with microannuli is approximately 10^3 to 10^5 times the flow rate of intact wellbore cement. We also found that samples created with a corroded casing were comparable to samples that had been thermally de-bonded.

We found that microannuli are fracture-like in how they deform in response to stress changes. With an increase in confining pressure, the hydraulic aperture of the microannulus decreases in a

non-linear manner. Unloading after the first increase in confining pressure often results in a smaller hydraulic aperture than during the original loading path. The hydraulic aperture changes from subsequent loading and unloading tend to be recoverable. In a few samples with small initial microannuli, the initial loading reduced the hydraulic aperture to that of intact cement and effectively healed the sample.

With an increase in casing pressure, the hydraulic aperture decreases; upon reducing the casing pressure, the hydraulic aperture tends to completely recover. The lower the confining pressure, the more affect a casing pressure change has on the hydraulic aperture of the microannulus. The microannuli response is less sensitive to casing pressure changes compared to confining pressure changes even when accounting for stiffness and geometric differences between loading the exterior of the cement sheath and loading the interior of the casing.

In one instance, the cement sheath was failed when the casing pressure was increased significantly above the confining pressure. This confirms another mechanism by which wellbores may become damaged.

The response of the hydraulic aperture to the pore pressure was only clear on tests conducted on one sample. In that case, we observed the hydraulic aperture increase as the pore pressure was decreased in a manner consistent with a conventional effective stress relationship between confining pressure and pore pressure.

We repaired a number of the flawed wellbore specimens. For samples with large flaws, we could simply introduce the repair material on the top of the sample and allow gravity to move it into the flaw. This method does not work if the flaw is less than nominally 50 μm; in these cases, we repaired samples by injecting repair material under a nominal pressure of 0.7 MPa.

Repair with the nanocomposite epoxy base material was successful in dramatically reducing the flow through flaws of various sizes and types. Flow through samples repaired with this material was comparable to an intact sample, and the repair remained effective after cycling the confining stress. In contrast, repair of flawed samples with microfine cement was initially less effective. In addition, the hydraulic aperture of the cement repaired sample increased with cycles of confining stress, indicating that the microfine cement repair was degrading.

After repair and testing, we sliced samples to allow for observations of the repair effectiveness. The nanocomposite epoxy base material appeared to fill all voids along the microannulus; in contrast, the microfine cement clearly did not. Image analysis of microphotographs of the cement-casing interface at a number of locations in a sample with a large microannulus were used to provide measurements of the actual (mechanical) aperture around the entire circumference. These data reveal that the actual aperture is highly variable along the circumference of the cement-casing interface. Over some portion of the circumference there is a tight contact between the cement and casing; that is, at that location there is no microannulus. These results suggest that it is necessary for a repair material to penetrate sizes smaller than the average hydraulic aperture to effectively seal a microannulus.

4 Modeling

4.1 Summary of Modeling

Three modeling capabilities were developed over the course of this project and are described in detail within this chapter. A finite element model was developed to complement bench-scale slant shear testing experiments of nanocomposite/steel interfacial bond strength (see Chapter 2). A second finite-element modeling capability was developed to complement the seal system testing (see Chapter 3). Lastly, field scale and wellbore scale models were developed to predict *in situ* stresses and strains in the wellbore during CO_2 injection.

4. 2 Finite Element Analysis of Slant-Shear Testing

Finite element analyses of the slant shear test configuration (see Figure 4-1) was conducted using ABAQUS modeling software. PCN was defined as a nonlinear elastic-plastic material using the constitutive stress-strain response measured in the uniaxial compression tests. The steel was assumed to be elastic perfectly plastic material. Convergence studies used two different types of built-in elements: 8-node linear hexagonal and 6-node linear triangular. These element types are capable of producing computationally inexpensive solutions for stress calculations. For each element type, different mesh sizes were used varying from 9,480 elements to 74,524 elements. Boundary conditions fixed the steel part from the bottom and prevented lateral deformation of the assembly.

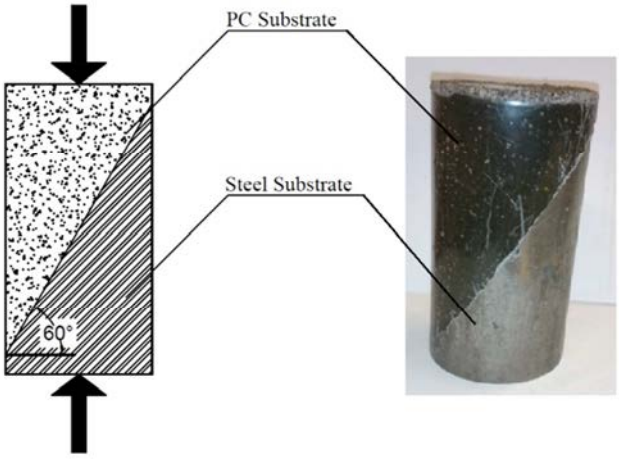

Fig 4-1: Slant shear test (left) schematics showing slant shear angle (right) actual specimen showing steel substrate and PC.

Figure 4-2 (a) shows the boundary conditions as applied on the model. **Figure 4-2 (c)** shows the meshed model using 6-node linear triangular elements. Displacement was applied to the top of PC to simulate slant shear tests. Load-displacement curves were extracted from the simulations and compared to those observed in the slant shear tests. In order to define contact between PC and steel, a zero-thickness cohesive contact element was defined. Bilinear shear stress-slippage relationship was used to describe the contact element as shown in **Figure 4-2 (b)** (Meo et al. 2005, Khokar et al. 2011). Damage and cohesive behavior conditions were used to define the contact element. Damage parameters, including initiation, evolution, and stabilization of damage, are used in ABAQUS to define contact mechanics (ABAQUS).

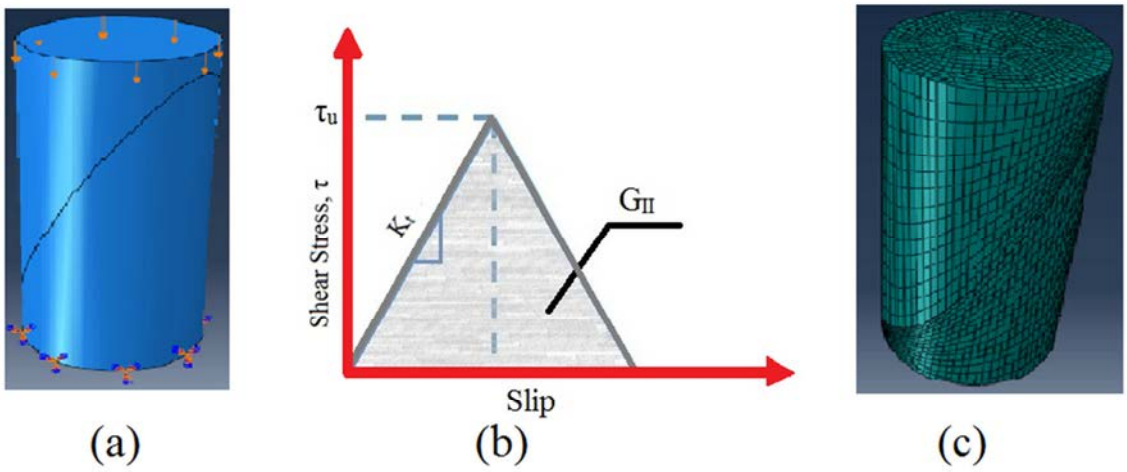

Fig4-2: FE model using ABAQUS simulation environment: (a) Boundary conditions (b) Bilinear shear stress-slip relation where K_t is shear contact stiffness, G_{II} is mode II fracture energy and τ_u is maximum shear stress (c) Meshed model using 74,524 elements.

Maximum shear stress τ_u, mode II fracture energy G_{II}, and viscosity coefficient, V, were used to define the damage parameters. Interfacial stiffness representing the stiffness of PCN-steel interface was defined using shear contact stiffness K_t. The values of τ_u, G_{II}, V and K_t were determined through experimental validation of the FE simulation and back-solving for those parameters (Abdel Wahab 2014). Our objective is to use the validated FE model to realize the local shear stresses developed at failure of the slant shear test. **Table 4-1** summarizes the contact interaction properties.

Figure 4-3 shows load-displacement curves for both FE model and slant shear test for the selected mixes namely PC-Neat, PCNC-0.5, PCNA-0.5, PCNA-2.0, PCNS-0.5 and PCNS-2.0.

Table 4-1: Interface interaction properties as defined in ABAQUS.

Contact Property / Mix	Damage			Cohesive Behavior
	Initiation	Evolution	Stabilization	Shear contact stiffness (K_t), MPa/mm
	Maximum shear stress (τ_u), MPa	Fracture energy (G_{II}), N/mm	Viscosity Coefficient (V)	
PC-Neat	43	19	0.001	56
PCNC-0.5	45	29		46
PCNA-0.5	42	17		75
PCNA-2.0	61	24		92
PCNS-0.5	53	21		90
PCNS-2.0	23	37		12

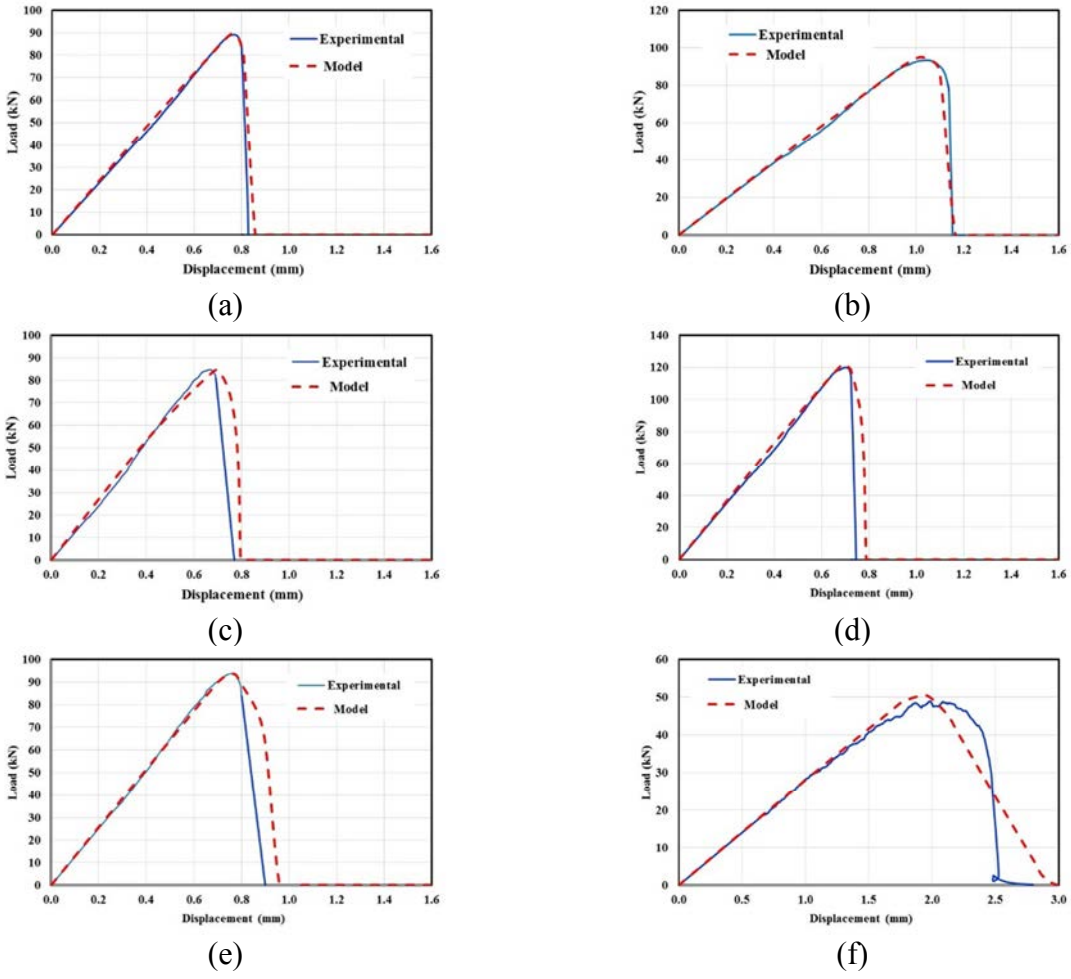

Fig4-3: Load-displacement curves of PC with different nanomaterials as measured experimentally during slant shear test and extracted using the finite element method for (a) PC-Neat, (b) PCNC-0.5, (c) PCNA-0.5, (d) PCNA-2.0, (e) PCNS-0.5, and (f) PCNS-2.0.

Further analysis of the FE simulation results shows strong correlation between Poisson's ratio and the shear modulus G described as $G = \frac{E}{2(1+\nu)}$ and the maximum local shear stresses at the interface. Since all nanomaterials caused an increase in Poisson's ratio, the maximum local shear stress is decreased by the increase in Poisson's ratio. This analysis supports the results for PCNC-0.5 and PCNA-0.5 in comparison with neat PC. Furthermore, another important factor controlling the maximum local shear stresses is the shear contact stiffness K_t. The shear contact stiffness controls the slippage occurring at the interface (see **Figure 4-2)** and may correspond to the friction between the contact surfaces**.** The effect of the shear contact stiffness on local shear stresses is apparent in the case of SNPs. FTIR analysis, discussed below, confirms that SNPs acted as an inert filler. This might explain its ability to increase interface friction compared with MWCNTs or ANPs, which apparently have the ability to chemically react with the epoxy matrix and/or the steel surface.

Finally, FE analysis results were also used to examine the interfacial shear stress contours at the PC-steel interface. **Figure 4-4** shows the load-displacement of neat PC extracted from the FE model with magnified slippage in the assembly at vertical displacements of 0.720 mm, 0.802 mm, and 0.837 mm.

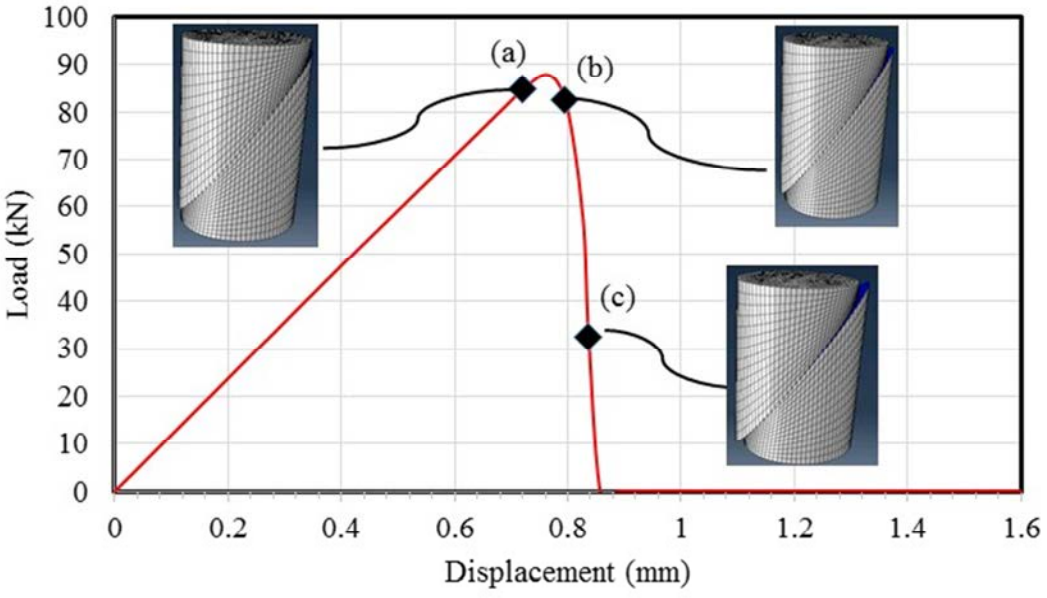

Fig 4-4: Load-displacement extract from finite element analysis of neat PC showing magnified slippage at 0.720mm, 0.802mm, and 0.837mm.

At each of these points, shear contours on the interface were plotted showing the maximum local shear stress to reach 40 MPa. Locations of maximum local shear stress concentration on the interface are shown in **Figure 4-5**.

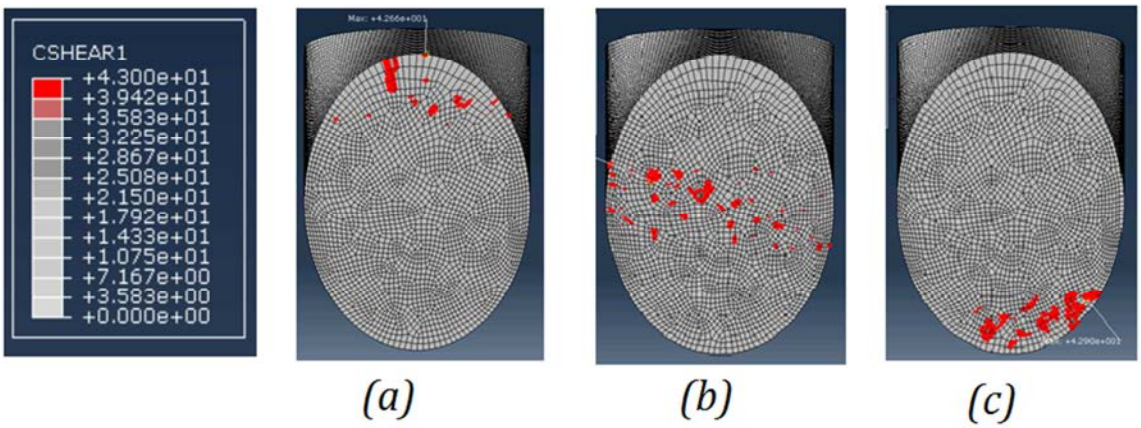

Fig4-5: Shear contours showing locations of maximum local shear stress during slippage at vertical slip of (a) 0.720 mm (b) 0.802 mm and (c) 0.837 mm

Maximum local shear stress only develops at the location of minimum height of PC before reaching ultimate load as shown in **Figure 4-4** and **Figure 4-5 (a)**. As slippage occurs, the maximum local shear stress moves along the interface. The maximum local shear stress path follows the height of PC from minimum to maximum as shown in transition in **Figure 4-5** from **(a)**, **(b)** and **(c)**. Slant shear tests show that complete slippage occurs after the ultimate load due to release of energy as a result of bond failure.

Nonetheless, incorporating nanoparticles in PC resulted in increasing the bond strength of PC to steel substrates. This improvement in bond strength when measured in terms of maximum local shear stresses is less significant than that measured using the apparent shear strength. FE analysis showed that the increase of bond strength in terms of maximum local shear stress is 5, 23 and 42% for PCNC-0.5, PCNS-0.5, and PCNA-2.0 respectively and a decrease of 2 and 47% for PCNA-0.5 PCNS-2.0 when compared with neat PC. These values are lower than those improvement depicted by the apparent/average shear strength shown in **Chapter 2 (Figure 2.23)**. The analysis demonstrates that the simplistic approach of averaging the shear stress is insufficient to compare materials with significant different mechanical properties (e.g. elastic modulus and Poisson's ratio). It is obvious that using slant shear test results to compare bond

strength of materials with significantly different mechanical properties should be done with care and its results might better be interpreted using the finite element method.

A more complete analysis and discussion of the slant-shear test can be found in Chapter 2 (section 2.3.2).

4.3 Finite element modeling of wellbore microannulus permeability

4.3.1 Summary

This research aims to describe the microannulus region of the cement sheath-steel casing interface in terms of its compressibility and permeability. A mock-up of a wellbore system was used for lab-scale testing. Specimens, consisting of a cement sheath cast on a steel casing with microannuli, were subjected to confining pressures and casing pressures in a pressure vessel that allows simultaneous measurement of gas flow along the axis of the specimen. The flow was interpreted as the hydraulic aperture of the microannuli. Numerical models are used to analyze stress and displacement conditions along the casing-cement interface. These numerical results provide good agreement with closed-form elastic solutions. Numerical models incorporating flaws of varying dimensions along the casing-cement interface were then developed to describe the microannulus region. A joint model is used to describe the hydraulic aperture of the microannulus region, where the mechanical stiffness is altered in response to the imposed stress state across the joint interface. The aperture-stress behavior is based upon laboratory measurements of hydraulic aperture as a function of imposed stress conditions.

This investigation found that microannulus permeability can satisfactorily be described by a joint model and that the constitutive model imposed in a numerical simulation can play a significant role in the solution behavior and agreement to experimental data. Recommendations for future work include an application of the joint model with a thermally active large-scale reservoir coupled with pore pressure caused by dynamic CO_2 injection and subsequent microannulus region affects.

4.3.2 Background

Wellbore integrity is compromised by flaws that arise from a number of different causes, including inadequate cement-formation and cement-casing bonds, cement shrinkage, formation of a microannulus at the casing-cement interface, fracture formation within the cement, poorly

emplaced cement, incomplete removal of drilling mud from casing prior to cementing, clay washouts at caprock interfaces, and others (Bois et al., 2012; Carey et al., 2013). The cement sheath is also potentially susceptible to acid degradation introduced by carbonated brine flowing from the formation and either onto the bottom of the cement plug or into the annular space of the cement sheath-steel casing interface (Matteo and Scherer, 2012; Kutchko et al., 2007).

The cement-casing interface, herein referred to as the microannulus, has been identified as a common leakage pathway (Bachu and Bennion, 2009; Bellabara, 2008; Zhang and Bachu, 2011). Once a microannulus is formed, its permeability is expected to be a function of stresses that would have tendency to either to further open the micorannulus or close it. These stresses include internal pressures in the casing as well as the external, as well as confining stresses from the host formation(s) surrounding the wellbore system. The external stresses that act on the cement sheath are a function of many factors, including the overburden pressure, the tendency of the rock to creep, deformations in the overburden and wellbore systems due to reservoir compaction or expansion, changes in formation pore pressure, expansion/contraction of the cement, and pressures and temperatures in the casing (Hawkes et al., 2005; Orlic, 2008). The pressure within a casing can also vary, depending on the condition and use of the wellbore. In an abandoned well, the casing pressure will depend on what material (water, mud, cement), if any, remains in the casing. While in operation, an injection well will have a casing pressure in excess of the formation pore pressure, but less than the overburden pressure to prevent formation failure. The contact stress across the cement-casing interface depends in part on the casing pressure. Temperature changes in the casing fluids may also induce casing expansion and contraction, imposing stresses on the cement-casing interface (Lavrov et al., 2015).

Understanding of microannulus flow as a function of stress is critical to a number of applications. Estimates of flow through a leaky wellbore with a microannulus will be improved if the stress conditions that are possible for a particular well are taken into account. The impact of well operations on wellbore integrity could be better understood and perhaps managed if the microannulus response to stress was understood. This knowledge would also inform efforts to repair leaky wellbores that often involve attempts to “squeeze” repair materials into the microannulus in order to restore the functionality of the wellbore. Small wellbore microannuli on

the order of 25 microns have shown to be a sufficient size to permit a gaseous flow path (Seidel and Greene 1985).

Numerical modelers are endeavoring to represent more complex constitutive laws that have been used to simulate viscoplastic rate dependence and non-linear hardening effects of geological rocks, cement, and other brittle materials (Martinez et al., 2013; Brannon et al., 2009) as well as cement slurry hardening, shrinkage, pore pressure effects on dynamic CO_2 injection process and subsequent rock fracture (Martinez et al., 2013; Carey et al., 2013; Gray et al., 2009). Cement sheath behavior has been modeled using Finite Element Analysis (FEA) which includes formation imposed far field stresses, cement shrinkage and expansion, hardening, interfacial debonding, and wellbore life time-history characterstics that give insight to cumulative effects on prospective damage and fracture (Gray et al., 2009; Ravi et al., 2002). Gray et al. (2009) allow for interfacial debonding along the contact interface of the casing and cement based on bond strength, however physical characteristics for the microannulis region are not directly accounted for.

Carey et al. (2013) modeled elevated pore pressure via CO_2 injection in computational simulations. These simulations were focused on damage and permeability increases from over-pressurization of the reservoir, including the propagation of damage along the wellbore annulus. A Mohr-Coulomb slip criterion is used to represent shear strength; excess shear stresses beyond the strength are assumed to result in damage which increases the material's permeability. Shear damage was assumed to increase the permeability of the wellbore cement from an initial intact value of 10^{-17} m^2 to a maximum of 10^{-15} m^2. For simulations with an overburden pressure 25 MPa and formation confining stresses of 13 MPa, an over-pressurization of the injection reservoir of about 6 MPa was sufficient to induce damage in the wellbore cement. The failure propagated along the wellbore and into the adjacent caprock in some simulations, and resulted in significant CO_2 flow away from the reservoir. An important limitation of this study is that the permeability-stress relationship for the wellbore system was assumed and not based on measured values.

Schreppers (2015) studied the sealing properties of cement by analyzing the lifetime loading history a wellbore experiences from formation, cement and casing initialization, completion and

operational phases, and cement-plugging and abandonment. This analysis includes transient thermal analysis during the drilling phase of the mud, hydrostatic slurry pressure, transient effects of cement shrinkage, formation pore pressure, and stress assumptions experienced by the cement, as well as other boundary conditions. Interface models between the steel casing and cement sheath, as well as the cement sheath and rock formation, are defined by interfacial elements. These elements are defined by a crack model and Coulomb friction model, where the interface fails by exceeding a tensile strength and shear stress along the interface respectively (Schreppers, 2015). This study did not estimate the permeability increases in response to predicted displacement or failure in the wellbore cement or along the cement-steel interface.

The models presented by Carey (2013), Schreppers (2015), and Gray (2009) present insight into stress conditions a wellbore system can experience and suggest possible failure modes that could affect the wellbore system's performance. However, these studies do not include an experimentally based model of wellbore microannulus permeability as a function of stress changes. In this paper, we present such a model.

This study describes measurements and subsequent modeling of the cement-casing microannulus. Measurements of flow through microannuli under varying confining pressures and internal casing pressures can be used to measure hydraulic aperture as a function of stress. These measurements are then used to fit a model for the compressibility and permeability of wellbore microannuli, which is implemented into a finite element simulation of the experimental set up.

4.3.3 Experimental Set-up

A mock-up of a wellbore system was used for lab-scale testing as described in Chapter 3. The experimental specimens consisted of a cement sheath cast on a steel casing with microannuli. Specimens were then tested in the configuration showed in **Figure 4-6**, which allowed measurement of gas flow along the axis of the specimen. Confining pressures and casing pressures in the pressure vessel could be independently controlled.

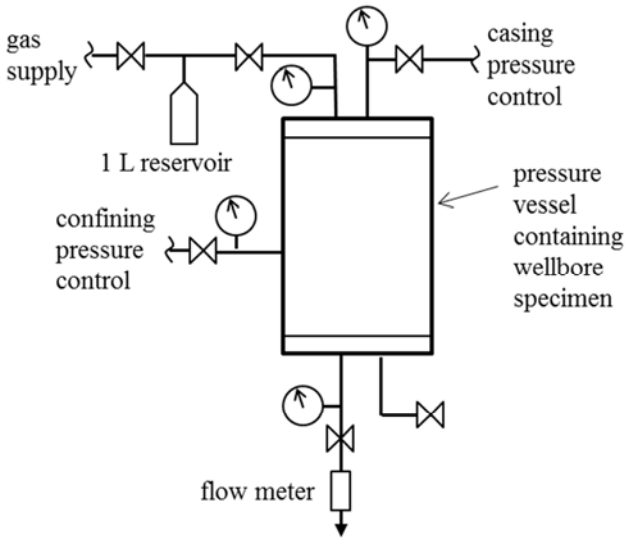

Fig 4-6: Schematic of experimental configuration used to measure gas flow through cement-casing specimens under variable confining pressure and casing pressure.

4.3.4 Setup for Finite Element Model of the Wellbore

Finite element models were created of the wellbore systems tested in the laboratory (as described in Section 2.1). The models include a cement sheath surrounding a steel casing; dimensions are consistent with the experimental system. The cement was modeled with the Kayenta plasticity model and the steel was assumed to behave elastically. Separate models were created to represent the interface between the cement and steel in different ways. A convergence study to determine the necessary number of elements used a full three dimensional model with a perfectly bonded interface between the steel and cement. Results from this model were compared to an analytical solution for an elastic bi-material hollow cylinder.

Subsequent three-dimensional quarter-symmetric models were created using the same meshing technique, but included additional elements to explicitly represent the microannulus at the interface between the steel casing and cement sheath. The microannulus elements could be assigned as open (gap) or as a separate microannulus material. Dimensions of the two models of the laboratory wellbore configuration are illustrated by **Figure 4-7** and **Table 4-2**. In this study the microannulus region was defined with the Kayenta constitutive model.

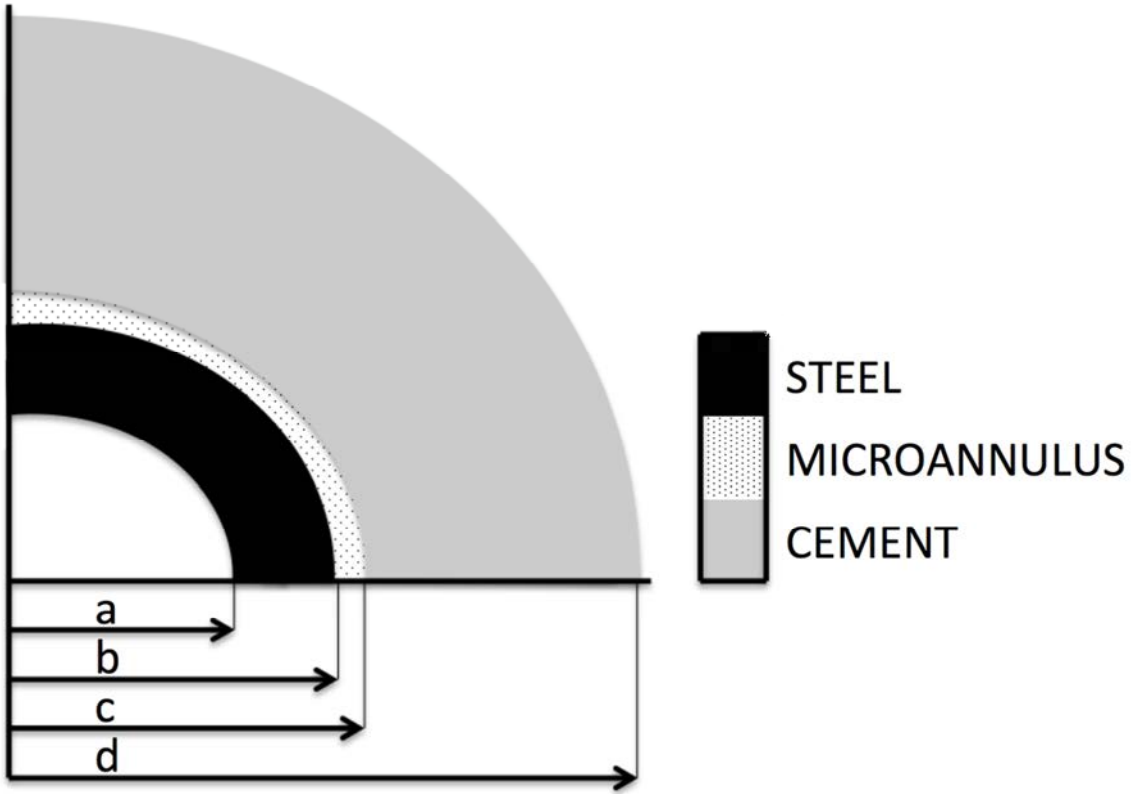

Fig 4-7: An exploded view of the laboratory wellbore model used for the parametric study.

Dimensions for model utilizing this configuration are shown in **Table 4-2**.

Table 4-2: Laboratory wellbore radial dimensions (mm) shown for a 2.35 mm casing with a small and large microannulus and tags referencing **Figure 4-7.**

Location	**Tag**	**Small Microannulus (19 μm)**	**Large Microannulus (136 μm)**
Internal Steel Casing	a	26.475	26.475
External Steel Casing/ Internal Microannulus	b	28.825	28.825
External Microannulus/ Internal Cement Sheath	c	28.844	28.961
Outer Cement Sheath	d	50.8	50.8

4.3.4.1 - Material Parameters

The properties used for the modeling of the elastic laboratory wellbore systems are given in **Table 4-3**.

Table 4-3: Laboratory wellbore elastic properties used in numerical convergence simulations.

Parameter	Symbol	Unit	Value
Young's Modulus: Cement	E_C	Pa	$4.00\ x\ 10^9$
Young's Modulus: Steel	E_S	Pa	$2.00\ x\ 10^{11}$
Poisson's Ratio: Cement	ν_C	Dimensionless	0.19
Poisson's Ratio: Steel	ν_S	Dimensionless	0.30

4.3.4.2 - Loading and Boundary Conditions

Boundary conditions included the externally applied confining pressure and the internal casing pressure. These pressures were applied at a linear ramp rate over a short period of pseudo-time, starting at a zero pressure state and increasing to the desired internal and/or external pressure load. Because the model response is time-independent, intermediate boundary conditions can be interpolated from these conditions; i.e. over a 0.5 second simulation with a desired internal and external pressure of 20 MPa and 30 MPa respectively, the state of pressure at 0.25 seconds can be inferred at 10 MPa and 15 MPa respectively. The loading rate applied to the FEA implementation of the laboratory wellbore was modeled with implicit quasi-static capabilities and therefore it was not intended to simulate the loading rate in the laboratory

4.3.4.3 - Wellbore model with microannulus

Stiffness elements (i.e. interfacial elements) are assigned to the microannulus regions, which are intended to capture the change in aperture of the microannulus as a function of normal stress across the microannulus using the joint stiffness model of Bandis et al (1983). These elements are shown as the region of annular joint spacing in **Figure 4-8**. Interfacial elements span the circumference between the steel casing and cement sheath, where a local coordinate system (x',y',z')belonging to the Kayenta material model defines a unique orthogonal system for each interfacial block; including a normal joint direction, orientation along the joint, and direction perpendicular to both of these. These joint directions are obtained from translations on the x, y,

and z coordinates, respectively. This method was used to calculate unique normal directions for joints spanning along the circumference of the microannulus region

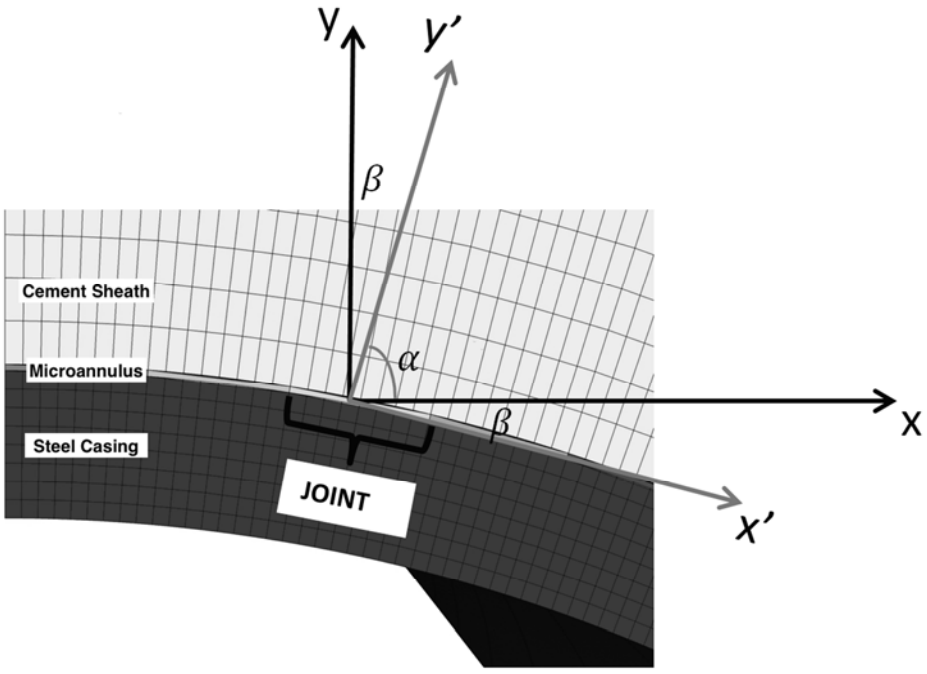

Fig 4-8: Coordinate systems used to determine stress acting across curved surface of microannulus joint.

4.3.5 - Results

4.3.5.1 - Experimental Results

Hydraulic aperture as a function of confining pressure for a specimen with a large microannulus is shown in **Figure 4-9**. The initial hydraulic aperture was 100 microns at a confining pressure of 4 MPa. With increasing confining pressure, the hydraulic aperture decreases non-linearly with increasing rate of confinement, averaging at a rate of approximately 4 micron per MPa, until a confining pressure of 20 MPa is reached. With continued increase in confining pressure above 20 MPa, the aperture decreases only slightly.

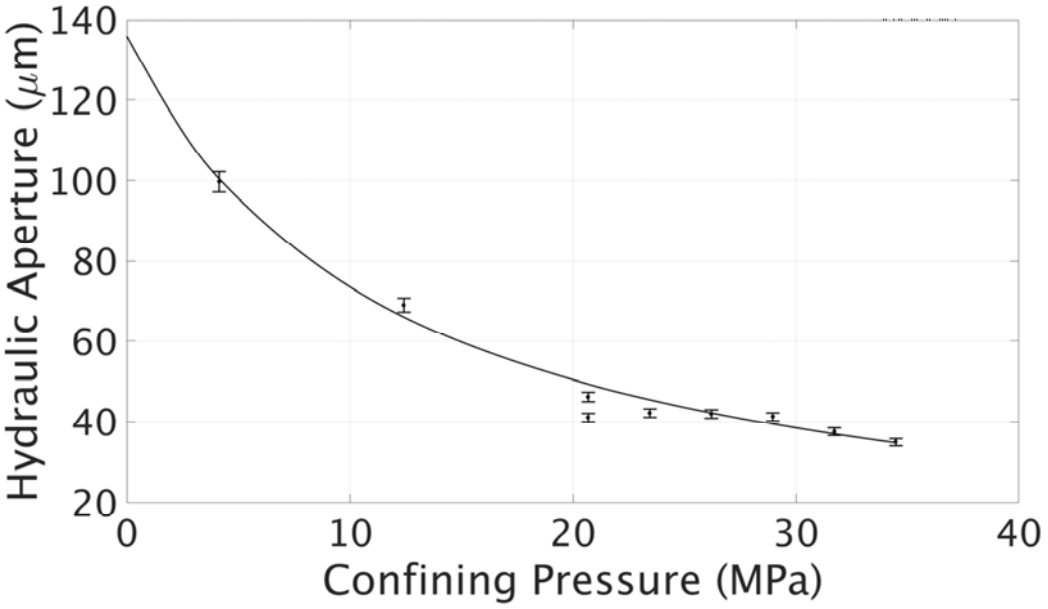

Fig 4-9: Hydraulic aperture as a function of confining pressure for specimen with large microannulus. The line is the best fit line to the hyperbolic model for these data (5% experimental error bars are shown for laboratory measured data).

In **Figure 4-10**, hydraulic apertures as a function of confining pressure for specimens with small microannuli are shown. With increasing confining pressure, the hydraulic aperture decreases. These hydraulic apertures are about one order of magnitude smaller than that for the specimens with a large microannulus.

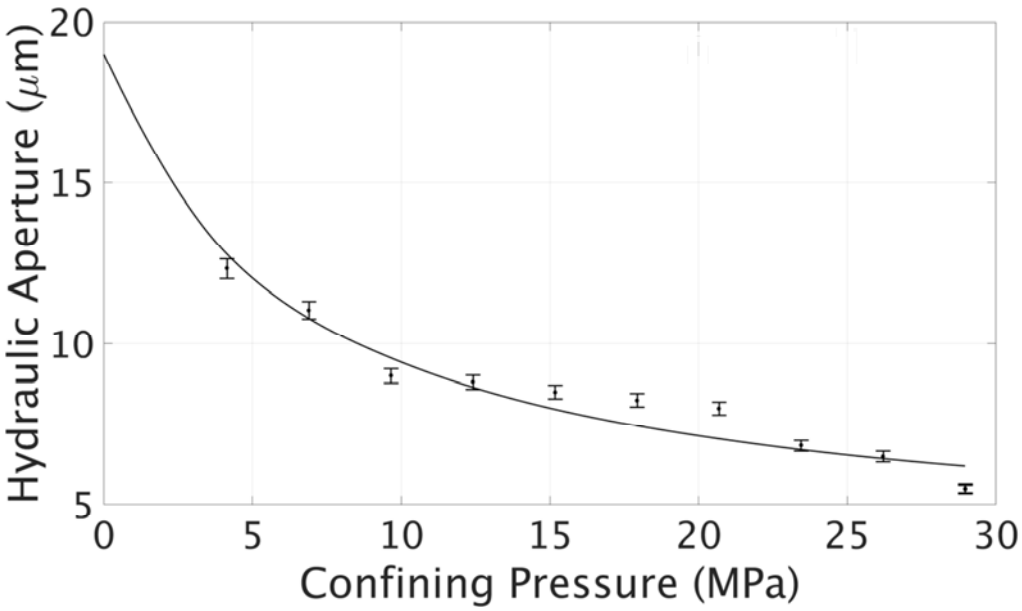

Fig 4-10: Hydraulic aperture as a function of confining pressure for specimens with small microannuli. The line is the best fit to the hyperbolic model for these data (5% experimental error bars are shown for laboratory measured data).

4.3.5.2 - Fitting Laboratory Data to Model

The hydraulic aperture change with applied stress data given in **Figures 4-9** and **Figure 4-10** are used to parameterize the hyperbolic model for a large and small microannulus. The hyperbolic model can be given in the linear form (Bandis et al., 1983)

$$\frac{\Delta V_j}{\sigma_n} = a - b\Delta V_j \qquad \textbf{(4.1)}$$

where $\frac{1}{a} = K_{ni}$, $\frac{a}{b} = V_m$ or the maximum closure, and ΔV_j is the closure of a joint under σ_n . Plotting $\frac{\Delta V}{\sigma_n}$ vs. ΔV yields a straight line with an intercept of a and a slope of $-b$. The hydraulic aperture data were interpreted as closure by subtracting the current aperture from the previous aperture. Because the test was conducted by controlling the confining pressure, the model is given in terms of confining pressure and not normal stress across the interface. In **Figures 4-11** and **4-12**, the best-fit straight line to Equation 4.1 is given for the experimental data measured for the large aperture and small aperture microannuli. Initial apertures (with no confining pressure)

for both data sets were found by extrapolating the model response to zero normal stress; these apertures were 136 μm and 19 μm for the large and small microannuli, respectively.

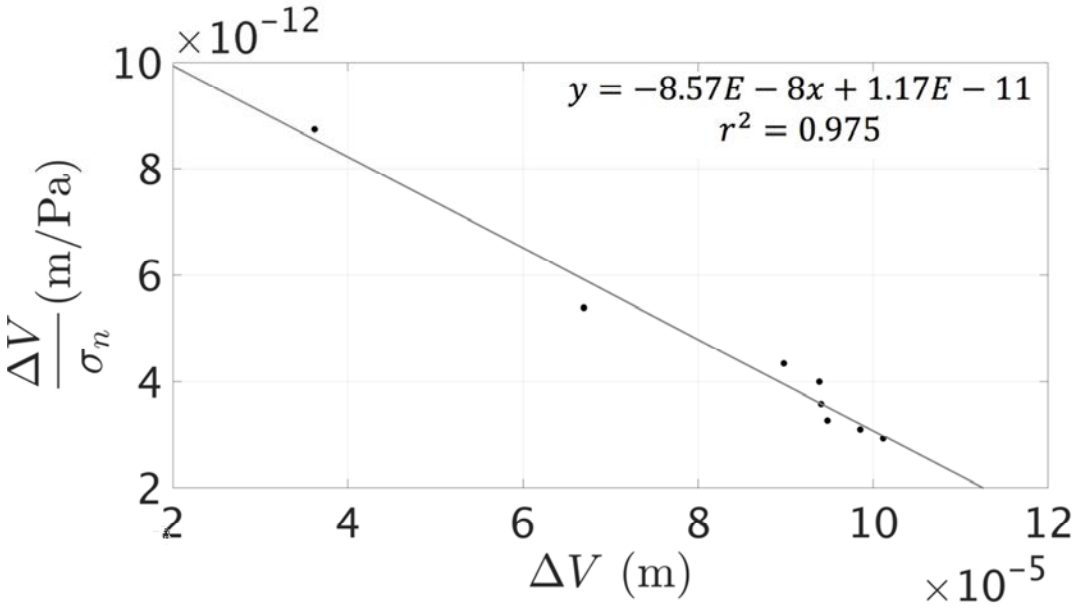

Fig 4-11: Fitting of laboratory data from large microannulus to hyperbolic model.

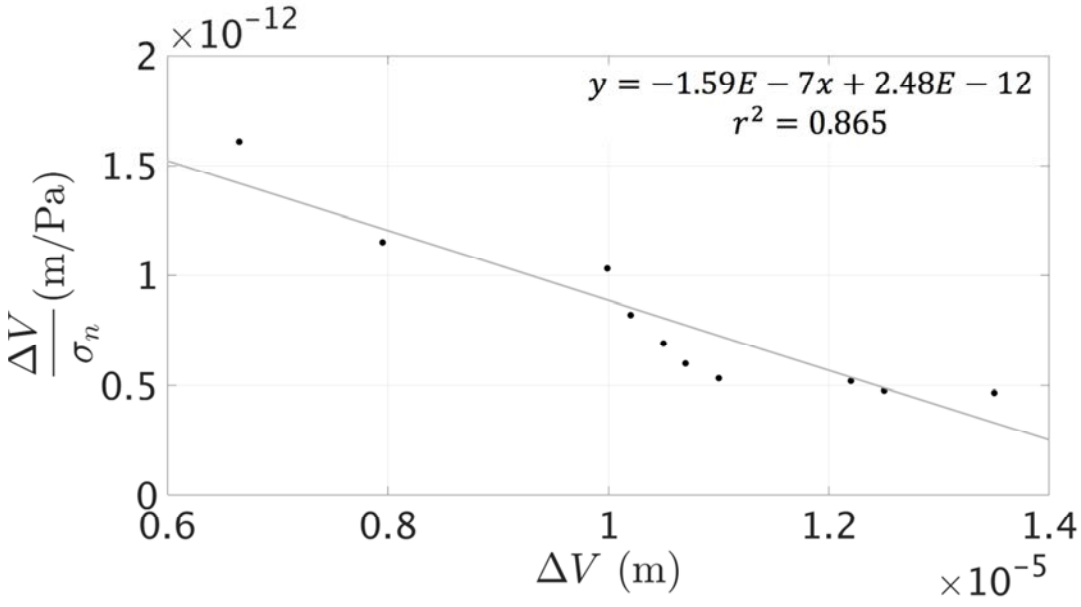

Fig 4-12: Fitting of laboratory data from small microannulus to hyperbolic model.

Using the parameters derived from fitting the data to the hyperbolic model, the prediction for hydraulic aperture as a function of confining pressure is given in **Figure 4-11** and **Figure 4-12**. These results suggest that the hyperbolic model provides a reasonable representation of the measured microannulus response to confining pressure. The hyperbolic model is subsequently implemented in finite element modeling of wellbore system to describe the stress-dependent change in the hydraulic aperture and consequently permeability of a wellbore microannulus.

The joint parameters derived from laboratory tests were used to populate the numerical model of the microannulus. **Figures 4-13** and **4-14** compare the laboratory data for the large (136 μm) and small (19 μm) microannuli with the numerical results, respectively. Both microannulus sizes were analyzed with the cement sheath parameterized with a Kayenta constitutive model. The modeled microannulus is shown to be slightly stiffer than the laboratory measured values in the 136 μm microannulus model. It is hypothesized that the occurrence of the large microannulus showing increased stiffness with respect to the small microannulus is due to furthered discontinuity between the cement and steel interface. That is, it is assumed that the microannulus is in contact throughout the circumference of the laboratory wellbore during FE computations; missing elements, voids or spaces of non-contact were not accounted for in this simulation.

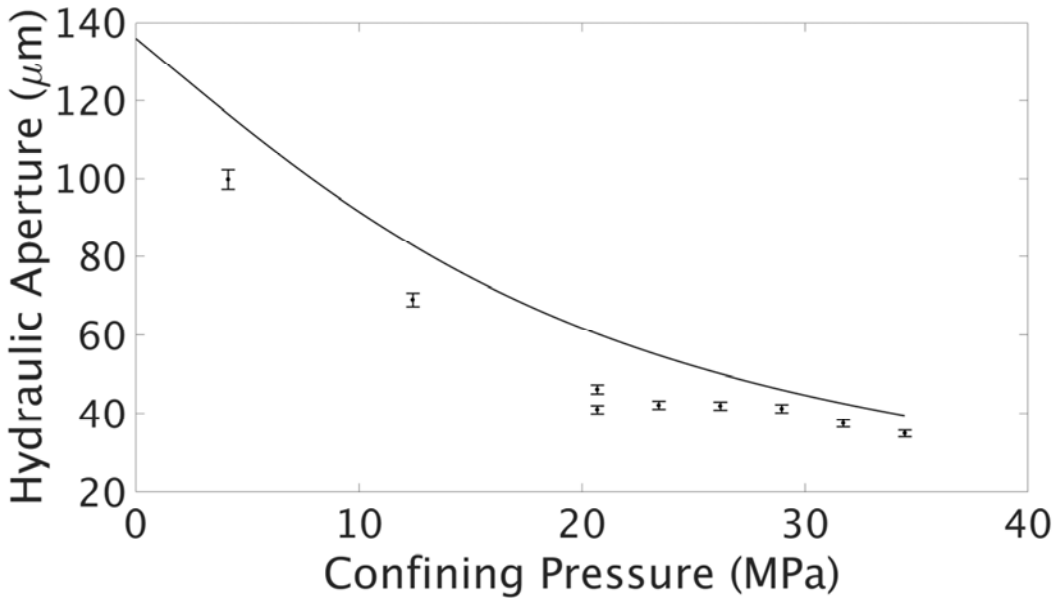

Fig 4-13: Laboratory measurements and numerical model comparison for the 136 μm microannulus joint (5% experimental error bars are shown for laboratory measured data).

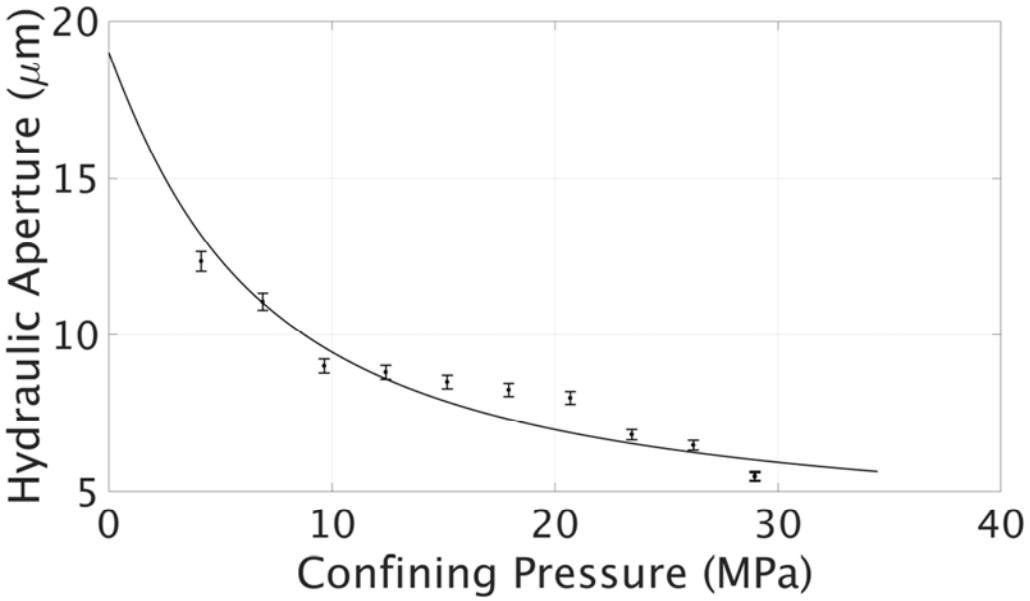

Fig 4-14: Laboratory measurements and numerical model comparison for the 19 μm microannulus joint (5% experimental error bars are shown for laboratory measured data).

4.3.6 - Discussion

With this model, the size (thickness over cross sectional area) of the microannulus is equivalent to the hydraulic aperture. Thus, the permeability of the microannulus can be back-calculated using the Forchiemer equation (Forchheimer 1901). **Figure 4-15** shows the permeability of the microannuli as a function of confining pressure. The permeability decreases as confining pressures are applied. For the larger microannulus, the permeability decreases from an initial permeability of 3.2×10^{-13} m^2 to 7.8×10^{-15} m^2 as the confining pressure is increased to 34 MPa; for the smaller microannulus, the permeability increases from 6.8×10^{-16} m^2 to 1.8×10^{-17} m^2 for this same increase in confining pressure. The permeability of intact cement is approximately 1×10^{-18} m^2 (Bear, 2013). Therefore, even with confining pressures of 34 MPa, an unrepaired wellbore microannulus can exhibit permeability approximately one to two orders of magnitude higher than that of intact cement and thus serve as a significant leakage pathway.

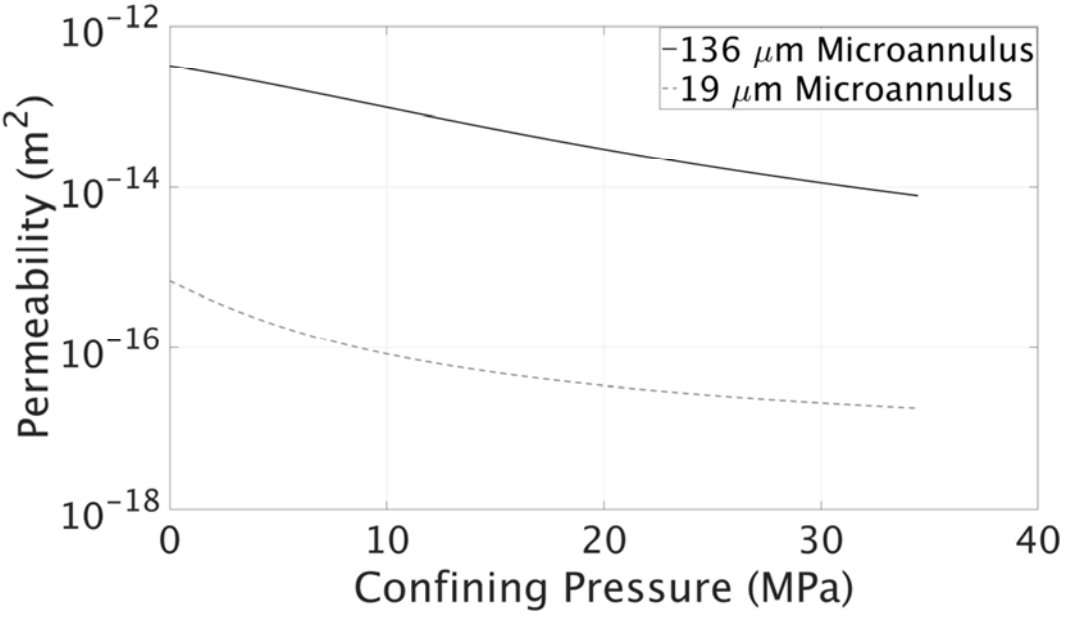

Fig 4-15: 136 μm and 19 μm microannulus permeability shown upon increasing confinement pressure.

Joint parameterization using laboratory data assumed that the joint normal stress is equivalent to the confining pressure, while numerical simulations used the stress normal to the microannulus element. In **Figure 4-16**, the applied confining pressure and the calculated contact normal stress across the face of the microannulus is given. For both microannuli, the contact stress is reasonably close to the confining pressure. For the larger and less stiff microannulus, this relationship is less linear.

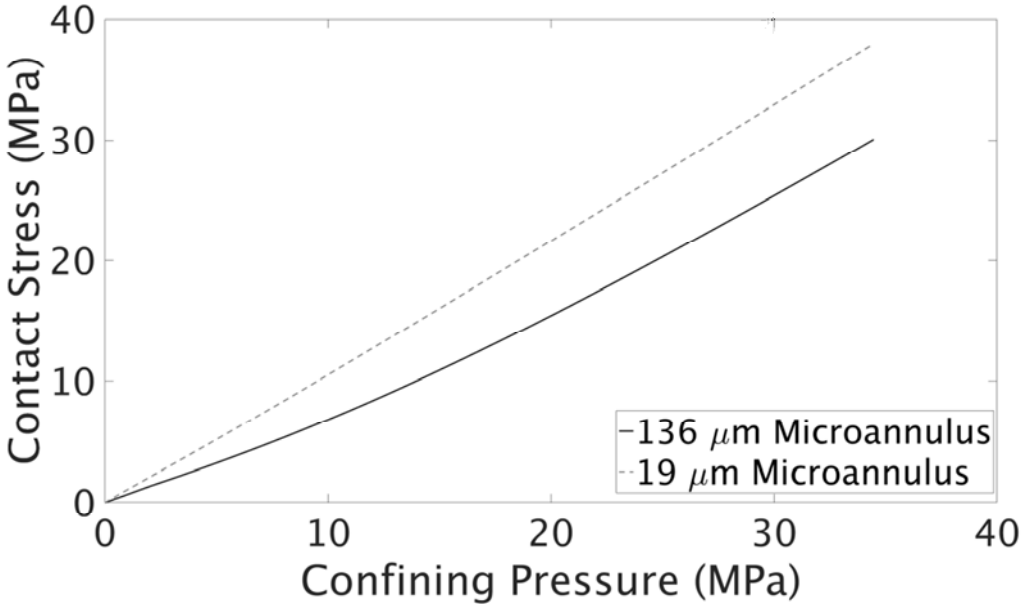

Fig 4-16: 136 μm and 19 μm microannulus joint contact stress and confinement pressure relationship.

The "cubic law" is used to estimate the hydraulic aperture, which in turn was assumed to be equivalent to the mechanical aperture. Under high flow rates and large apertures, it is a reasonable assumption that the mechanical and hydraulic aperture are equivalent. However, this assumption becomes less certain when fracture aperture approaches the scale of the surface roughness (Iwai, 1976; Renshaw, 1995). In this study, the surface roughness between the steel casing and cement sheath was accounted for by adjusting the stiffness based on the model of Bandis et al. (1983), thereby the microannulus roughness features are embedded into the model description. However, by accounting for the surface roughness as a fitting coefficient, it is possible that a more accurate representation of hydraulic aperture closure may be developed. Explicitly incorporating the surface roughness in a model of microannulus behavior would require characterizing and parameterizing the surface roughness, which was not available for these experiments.

The joint aperture response during loading and unloading can be different (Souley et al., 1995). Similarly, the hydraulic apertures interpreted from measurements on microannuli have indicated that the response may be hysteretic: hydraulic aperture changes during unloading were sometimes smaller than those during loading (Stormont et al., 2015). However, the constitutive

model implemented for the microannulus does not have history dependent properties. A more complete model for microannulus behavior would include hysteresis.

The numerical implementation for the microannulus behaves in response to normal joint behavior in a hyperbolic manner as discussed by Bandis et al. (1983). Other relationships may fit these data as well. Future studies should also consider the joint response to shear loading in addition to normal loading such as that given by Souley et al. (1995).

4.3.7 - Conclusions

Laboratory tests measured the compressibility and flow characteristics of wellbore microannuli. Specimens, consisting of a cement sheath cast on a steel casing with microannuli, were subjected to confining pressures and casing pressures in a pressure vessel that allows simultaneous measurement of gas flow along the axis of the specimen. The flow was interpreted as the hydraulic aperture of the microannuli. We found the hydraulic aperture decreases as confining stress is increased. The larger the initial hydraulic aperture, the more it decreases as confining stress increases. The changes in measured hydraulic aperture correspond to changes of many orders of magnitude in permeability of the wellbore system, suggesting that microannulus response to stress changes may have a significant impact on estimates of wellbore leakage.

The experimental data were satisfactorily described by the hyperbolic model of Bandis et al. (1983) which had been previously developed for closure of rock joints and fractures. The model is parameterized with two terms, one for the initial stiffness of the microannulus and one for the maximum aperture closure. With this model, we can estimate the hydraulic aperture, and therefore permeability, as a function of the stress acting across the microannulus.

A finite element model of a wellbore system was developed that included elements representing the microannulus that incorporated the hyperbolic joint model. The thickness of the microannulus elements is equivalent to the hydraulic aperture. The calculated normal stress across the microannulus used in the numerical implementation was found to be similar to the applied confining pressure in the laboratory tests. The microannulus elements were found to reasonably reproduce laboratory behavior during loading from confining pressure increases. The calculated microannulus response to internal casing pressure changes was less stiff than measured, which may be due to hardening of the microannulus during testing.

We found that the Bandis et al. (1983) joint closure model satisfactorily describes microannulus response, and therefore can be incorporated into models of damaged wellbore systems to estimate the response to different conditions that may be of interest to particular applications where wellbore integrity is of interest. In particular, the microannulus model could be used to estimate CO_2 leakage as a function of formation stress changes and/or displacements, or loading from casing expansion or contraction during wellbore operations. Future work should consider the role of hysteresis and shear loading on the joint response.

4.4 Modeling at the Field Scale and Wellbore Scale

Even though modeling at the Field Scale and Wellbore Scale were not part of this projects objectives, the methodologies and results are presented to provide a more thorough discussion of the on-going research in this field.

4.4.1 Summary

A critical aspect of designing effective wellbore seal repair materials is predicting thermo-mechanical perturbations in local stress that can compromise seal integrity. For applications associated with CO_2 sequestration, the stress-strain history of abandoned wells, as well as changes in local pressure, stress, and temperature conditions that accompany carbon dioxide injection or brine extraction are of interest. Building on existing thermo-hydro-mechanical (THM) finite element modeling of wellbore casings subject to significant tensile and shear loads, we have been developing advancements to a conceptual and numerical methodology to assess responses of annulus cement and casing. The experimental component utilizes bench-top experiments of an integrated seal system in an idealized scaled wellbore mock-up to test candidate seal repair materials (Genedy et al. 2014, Stormont et al. 2015). These bench-top experiments have been modeled with bench-scale numerical models to identify and evaluate the essential hydrologic and mechanical properties of the candidate sealants (see **Section 4.3**).

This section describes the manner in which field scale models using the stratigraphy from a pilot CO_2 injection operation can be used to estimate the necessary mechanical properties needed for a successful repair material. A field scale model that uses the stratigraphy, material properties, and injection history from a pilot CO_2 injection operation to develop stress-strain histories for wellbore locations from 100 to 400 meters from an injection well. The results from these models are used as input to a more detailed model of a wellbore system. The 3D wellbore model

examines the impacts of various loading scenarios on a wellbore system. The results from these models can be used to estimate the necessary mechanical properties needed for a successful repair material.

4.4.2 The Field Scale Model

A field scale model was implemented that uses the stratigraphy, material properties, and injection history from a pilot CO_2 injection operation to develop a stress-strain history for wellbore locations from 100 to 400 meters from an injection well. A field scale model of this sort would be most applicable if it were based on an active fluid injection site for which substantial material property, injection rate, stratigraphy, in-situ stress, and surface subsidence/uplift data are available or can be readily obtained through laboratory testing. One of the best sites that currently fits most of these criteria is the Cranfield CO_2 storage site in the state of Mississippi (Lu et al. 2013, Hovorka et al. 2013, Hosseini et al. 2013, Nicot et al. 2013). A field scale model for this site has been constructed, based on a previous model of a similar injection site (Martinez et al. 2013). Mechanical and hydrological data for the model have been recently published (Lu et al. 2013, Hovorka et al. 2013, Hosseini et al. 2013, Nicot et al. 2013), and additional property data has been recently obtained from laboratory experiments (Rinehart 2015).

Description of CO_2 Injection site

The Cranfield CO_2 injection project was developed by the National Energy Technology Laboratory (NETL) to "develop technologies to demonstrate that ... injected CO_2 remains in the injection zones" (National Energy Technology Lab 2011). The site is located in southwestern Mississippi, as shown in **Figure 4-17**, and is a former oil production site that had been in disuse since 1966. During this idle period, the reservoir pressure recovered to near-initial pressure as a result of natural water incursion. Between 2008 and 2013, nearly 4 million metric tons of CO_2 have been injected into the formation at Cranfield (Hovorka et al. 2013).

The Cranfield site consists of several alternating layers of limestone, sandstone, mudstone, and calcium-rich marl and chalk. **Figure 4-18** shows the generalized stratigraphy of the Cranfield site. The mudstone, marl and chalk act as barrier layers, confining water and other fluids to the limestones and sandstones. The injection zone is the Lower Tuscaloosa sandstone, whose 20-28 m thickness contains many alternating sublayers of chert- and volcanic-rock-fragment-rich sandstones and conglomerates. The region is populated by many abandoned wells from the oil

production era; some of the wells have been examined for the well casing and cement liner integrity, as shown in **Figure 4-19**. Several new injector wells have been drilled into the formation. Injection of CO_2 began in 2008, and the injection rate was steadily ramped up until a target rate of 1 million metric tons per year was achieved in April 2010 (Hovorka et al. 2013).

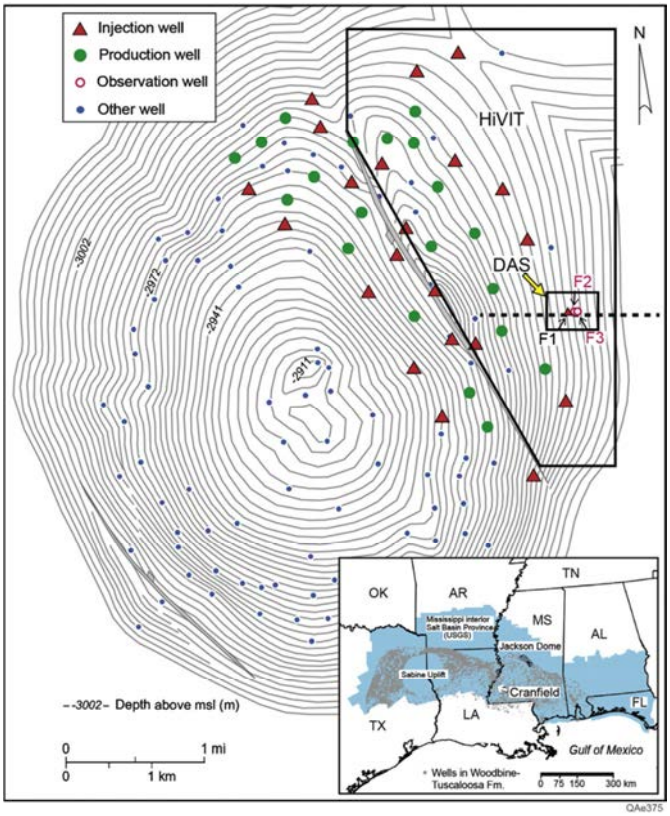

Fig 4-17. Aerial view of the Cranfield Site (Nicot et al. 2013).

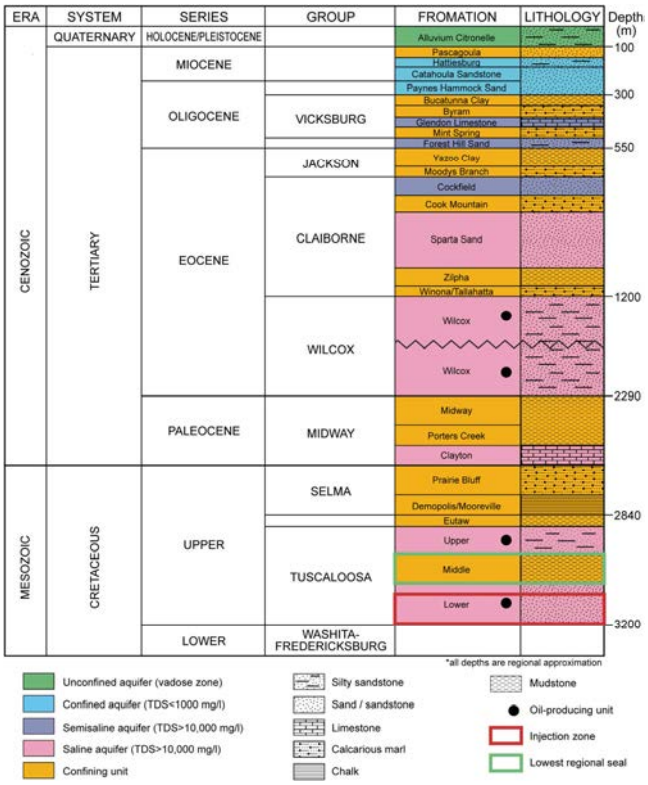

Fig. 4-18. Generalized stratigraphic column for area of Cranfield field, Mississippi, USA (Lu et al. 2013).

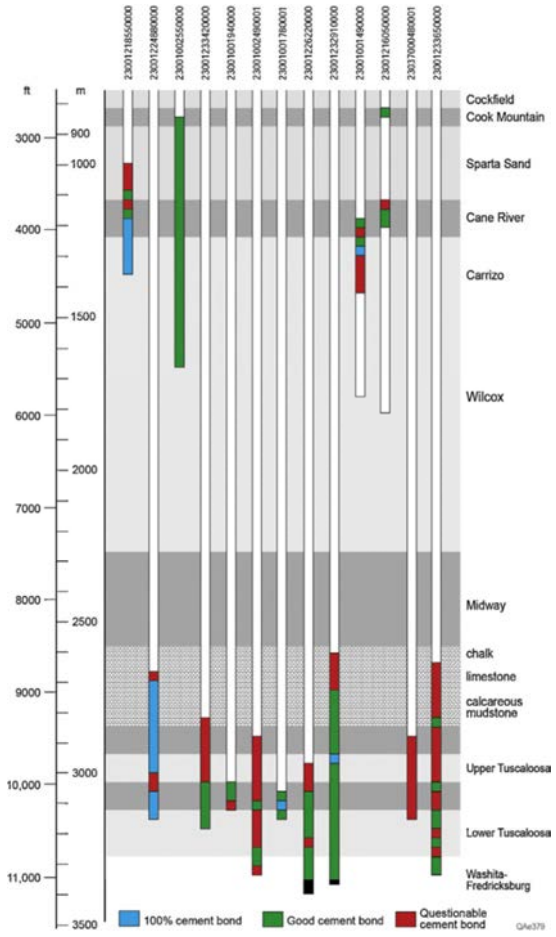

Fig 4-19. Stratigraphy view of the Cranfield Site showing abandoned wells profile (Nicot et al. 2013).

Description of Field-Scale Model

Field scale modeling, which features coupled geomechanical and multiphase flow models, is used to predict pore pressure, deformation, and non-wetting phase (CO_2) saturation, and the resultant changes to in situ stress, strain, and deformation (including surficial uplift and vertical displacement along columns). These predictions can, in turn, be used as input to a 3D geomechanical wellbore model to realistically predict wellbore stresses and strains.

The computational mesh of the field scale model is shown in **Figure 4-20**. The mesh comprises 515,000 elements, five horizontal stratigraphic layers, an area bounded by a 5,000-m square, and four columns representing locations of existing boreholes, spaced 100 m apart. The Lower Tuscaloosa aquifer is the layer into which fluids are injected, via a borehole at the mesh origin (lower left corner). For the simulation, the injection rate is increased linearly over the first year

from 0 to 1 million metric tons per year, then held constant at that rate for an additional four years.

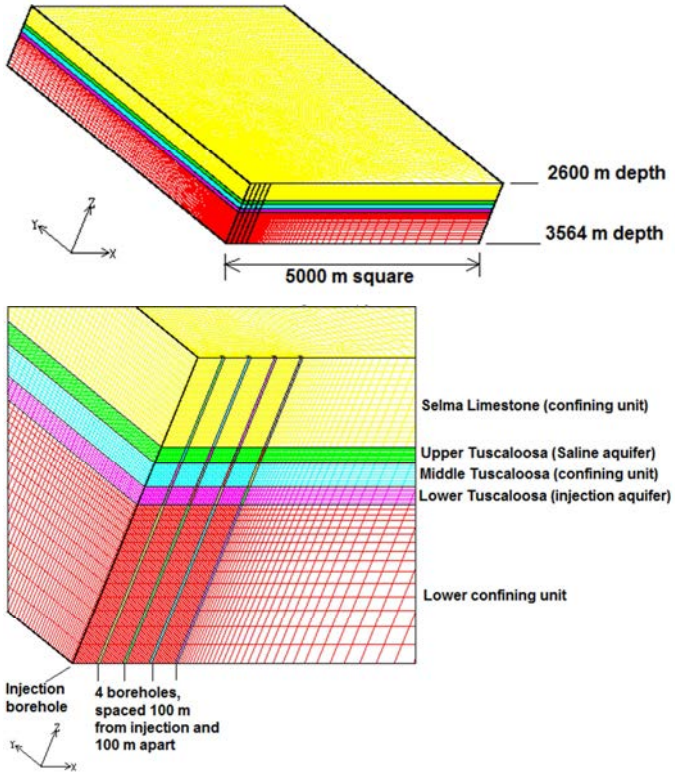

Fig 4-20. Computational mesh for Cranfield field-scale model.

The computational software used for the coupled hydrological-mechanical calculations is SIERRA, framework of coupled multiphysics simulation software composed of a suite of highly parallelized finite element analysis code modules for coupled fluid, solid, thermal, and chemical processes (Edwards et al. 2001, Martinez et al. 2011, Notz et al. 2007, SIERRA Solid Mechanics Team 2010, SIERRA Solid Mechanics Team 2011). The work described here utilizes the coupling of the Sierra/Aria module for multiphase flows (Notz et al. 2007) with the Sierra/Adagio module for nonlinear geomechanics (SIERRA Solid Mechanics Team 2011). The majority of the stratigraphic layers in the computational model are assumed to behave elastically. For simulation of the coupled hydrological-mechanical behavior in the Lower Tuscaloosa injection layer, the Kayenta constitutive model (Brannon et al. 2009), which was developed to include features and fitting functions appropriate to a broad class of materials including rocks, rock-like engineered materials (such as concretes and ceramics), was used. Fundamentally, Kayenta is a generalized plasticity models that includes a yield surface, with the term "yield"

generalized to include any form of inelastic material response including microcrack growth and pore collapse. Kayenta supports optional anisotropic elasticity associated with joint sets modeled as a continuum, as well as optional deformation-induced anisotropy through kinematic hardening. The governing equations are otherwise isotropic. Because Kayenta is a unification of simpler models, it can be run using as few as 2 parameters (for linear elasticity) to as many as 40 material and control parameters in the exceptionally rare case when all features are used. Isotropic damage is modeled through loss of stiffness and strength. In the Kayenta model, the bulk modulus K is usually formulated as a function of the first stress tensor invariant I_1 (Brannon et al. 2009) or the mean normal stress σ (Dewers et al. 2014):

$$K = K_0(1 - K_2 \exp\left(-\frac{\gamma_p}{K_3}\right))(1 + K_1\sigma) \qquad \textbf{(4.2)}$$

A similar equation is used for defining the shear modulus G. Also, Kayenta defines a yield function F in stress space (taking into account the Lode angle) such that elastic states satisfy $F <$ 0:

$$F_f(I_1) = a_1 - a_3 e^{-a_2 I_1} + a_4 I_1 \qquad \textbf{(4.3)}$$

Table 4-4. Kayenta parameter values for Lower Tuscaloosa sandstone (Rinehart 2015).

Parameter, units	Value
B0, MPa	2846
B1, MPa	100
B2, MPa	150
B3, MPa	2561
B4, dimensionless	0.0020
G0, MPa	1200
G1, dimensionless	0.01
G2, 1/MPa	0.0002
G3, MPa	1080
G4, dimensionless	0.0030
a1, MPa	26.5
a2, 1/MPa	0.03
a3, MPa	6.51
a4, dimensionless	0.210

Recently, laboratory mechanical property tests were performed on core specimens from the Lower Tuscaloosa sandstone (Brannon et al. 2009, Dewers et al. 2014). Parameters for the bulk and shear moduli and yield function equations were developed from those tests, and those

selected for the Lower Tuscaloosa predominantly quartz-cemented tabular very fine sandstone are listed in **Table 4-4**.

Results of Field-Scale Model

At this time, only preliminary results from the field scale calculations are available. These results used comparable mechanical properties from another simulation (Martinez et al. 2013), so they cannot be used to compare to the Cranfield data, but they can be used from a qualitative standpoint to describe the behavior of the aquifer during injection and the potential resulting effects on borehole casings in the vicinity. **Figures 4-21** and **4-22** show the initial hydrostatic pore pressure and the resulting pore pressure from 270 days of CO_2 injection. Note that the CO_2 wetting plume has extended through and past all four borehole locations. The result of the pressurized injection is that uplift is induced into the overlying formation, as shown in **Figure 4-23**. This uplift creates stress and strain changes in the host rock media which are transmitted to the cement liner and/or epoxy-filled spaces between the rock and the steel casings.

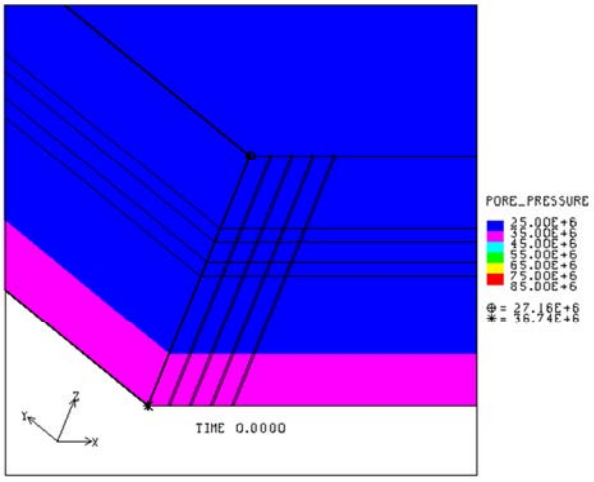

Fig 4-21. Field scale modeling results, hydrostatic pore pressure at time zero.

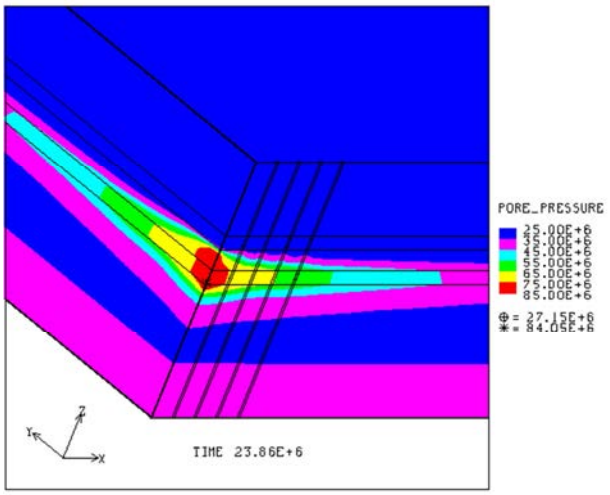

Fig 4-22. Field scale modeling results, pore pressure at 270 days of injection.

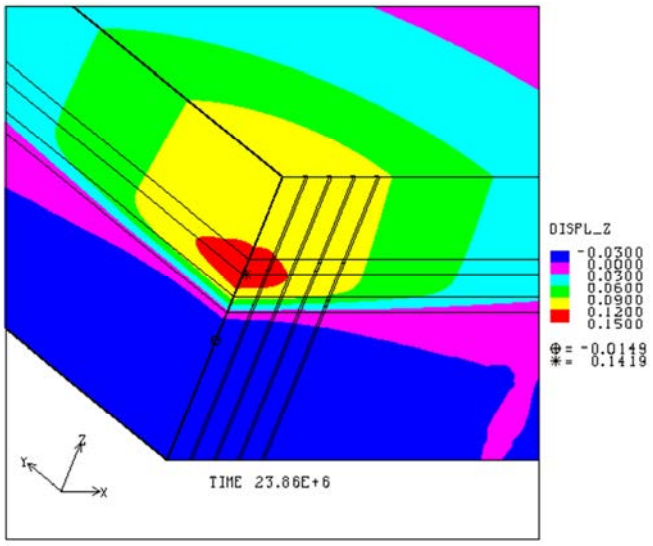

Fig 4-23. Field scale modeling results, vertical displacement at 270 days.

4.4.3 – Wellbore Scale Model

The final component of the evaluation of the seal repair materials uses a wellbore-scale model. Wellbore modeling is being used to quantify the stresses and strains that seal repair materials will face in the wellbore environment. The material properties of the developed nanocomposites were obtained in the bench-scale laboratory experiments and corresponding analyses. The field scale model provides the stress-strain environment that will be applied to the wellbore. These data

will also be used as input for the wellbore model to predict the response of the synthesized nanocomposites.

Two separate wellbore-scale models have been developed during this study. The first model includes steel casing(s); cement surrounding the casing(s); and formation rock around everything, and was designed to evaluate the stresses induced on casing materials under shear loading. The computational domain included two different bedded geologic media with a horizontal slip plane between them. Displacement boundary conditions arising from slippage along the slip interface were imposed on the boundaries of the wellbore model to simulate shearing and parting along a bedding plane cutting through the well axis. The interface is treated as a "slip surface" at the top or bottom of a layer. The two rock formations subject to slippage and the associated wellbore cement, steel, and epoxy system are highlighted in **Figure 4-24**. Vertical profiles of predicted Von Mises stress and equivalent plastic strain (EQPS) are shown in **Figures 4-25** and **4-26**.

Additional studies were performed by inserting cement material parameters inside of the microannulus region, creating a perfect bond between the steel and cement interfaces. Under the loading conditions of the slipping bed rock system, stress at the cement/casing interface is greater when the yield stress of cement is low as shown in **Figures 4-27** and **4-28**.

The second wellbore model contains a similar steel casing and cement-or-epoxy annulus representation for an entire length of borehole that matched the 100-m-spaced borehole columns of the field-scale model. The next step in this analysis process is to transfer the computed stress, strain, pore pressure, and displacement histories for each borehole column in the field-scale model to the wellbore-scale model to evaluate the effects on the cement and nanocomposite epoxy. Kayenta mechanical properties will be developed for the epoxy from the suite of laboratory bench-scale tests that are still in progress.

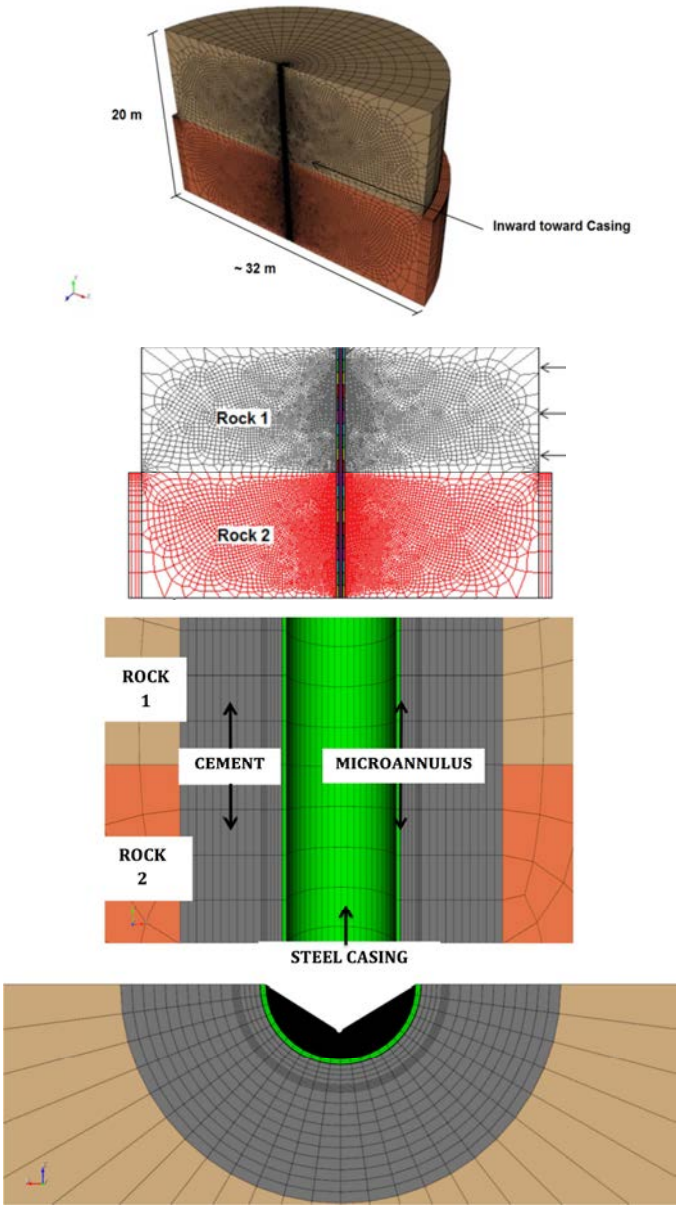

Fig 4-24. Simplified mesh (top) was used to develop and test simulation code. The mesh includes well casing, cement sheath, open annular region, and rock formation. The open annular region or "microannulus" can represent a flaw (annular gap), intact cement, or epoxy.

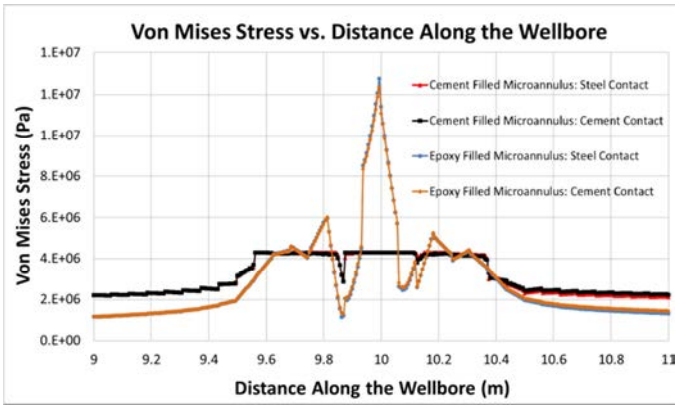

Fig 4-25. Von Mises Stress results plotted along the wellbore microannulus. The cases presented include the microannulus filled with cement and epoxy, analyzed on their respective contact surfaces.

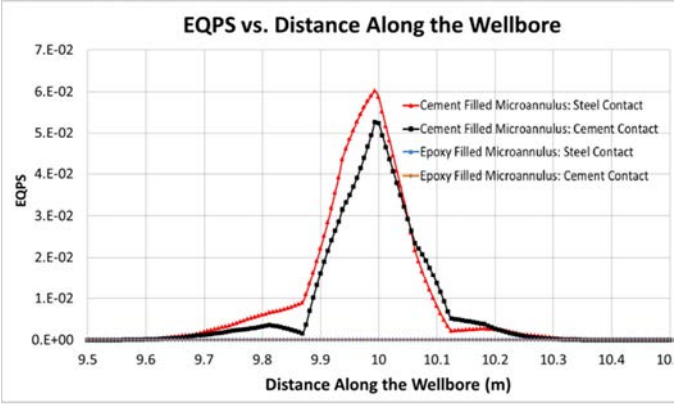

Fig 4-26. Equivalent Plastic Strain (EQPS) results plotted along the wellbore microannulus. The cases presented include the microannulus filled with cement and epoxy, analyzed on their respective contact surfaces.

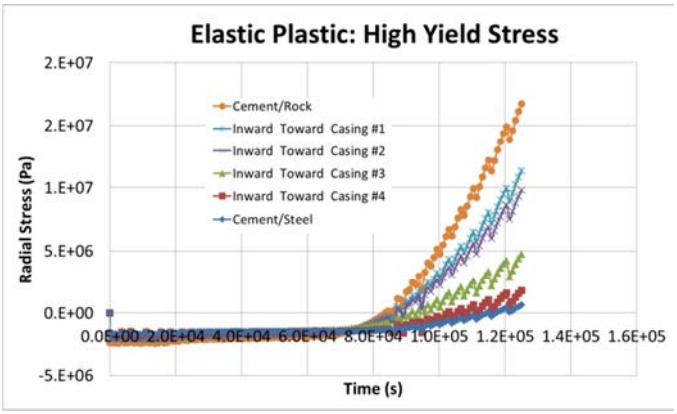

Fig 4-27. Modeling results under elastic-plastic conditions with a cement microannulus for a cement with a high yield stress.

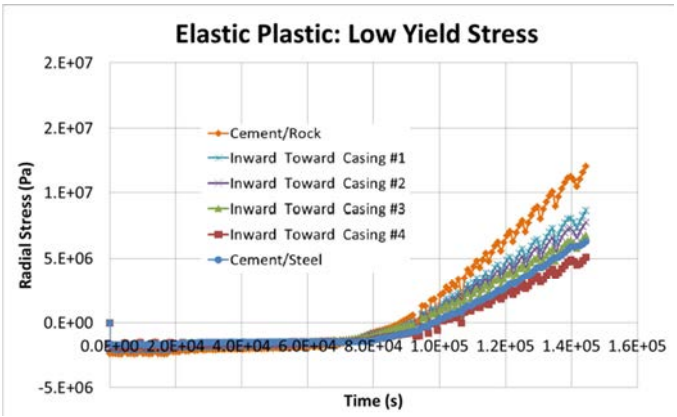

Fig 4-28. Modeling results under elastic-plastic conditions with a cement microannulus for a cement with a low yield stress, indicating the importance of the yield stress model employed.

4.4.4 Conclusions

A combined study of nanocomposite sealant materials for borehole repair, comprising laboratory bench-scale testing and numerical modeling at three different scales, has been initiated. Bench-scale testing has progressed to a point where cement fracture has been generated under certain axial and confining pressure conditions. A bench-scale numerical model has been developed to simulate the experiments, with some initial success. A field-scale model designed to predict loading conditions on nanocomposite materials used for borehole repair has been developed, and sandstone mechanical properties measured in the laboratory have been obtained for the model. Finally, a wellbore model has been developed that can be used to evaluate the response of the wellbore system (casing, cement, and microannulus), including the use of either cement or an epoxy in the microannulus to represent a repaired system. The current wellbore model will use prescribed characteristic stratigraphy used to evaluate other scenarios, including a reservoir depletion case and respective pore pressure gradient, in order to assess the expected wellbore conditions that a repair material will experience. These results will be used to inform our continuing nanocomposite repair material development and testing efforts

5. CONCLUSIONS

Conclusions and accomplishments of the project are given below. They are organized in the three principal activities of the project: materials development, seal system testing, and modeling.

Materials development

Candidate repair materials were synthesized from combinations of 3 different types of base polymers and 4 different nanoparticles. Base polymers were styrene-butadiene rubber (SBR) polymer latex, low modulus polysulfide-siloxane epoxy and novolac epoxy; candidate nanomaterials were carbon nanotubes (CNTs), nanoclay, nanosilica and nanoalumina particles. A total of 26 formulations were prepared and tested, along with a type G cement which served as the reference material. We developed both polymer cement nanocomposites (PCNCs), which included a filler, and polymer nanocomposites (PNCs) which did not include a filler. We developed methods for mixing the nanocomposites to ensure complete dispersion of the nanoparticles.

We down-selected candidate materials based on flowability and bond strength testing. The nanocomposites provided such a strong bond with steel that pull-off tests resulted in failure within the nanocomposite rather than at the interface with the steel. Subsequently, slant shear tests were conducted to force failure along the nanocomposite-steel interface. Slant shear tests were also used to obtain stress-strain behavior. We found that all nanocomposites were superior to microfine cement in terms of bond strength and had acceptable flowability. Novolac epoxy combined with CNTs or nanoalumina particles produced nanocomposites with the best properties.

Additional microscale tests were conducted to characterize the nanocomposite repair material. Dynamic Mechanical Analyses (DMA) were used to investigate the effect of the nanoparticles on the glass transition temperature (T_g) of the polymers and cross-linking density. The degree of chemical reactivity of the nanomaterials with the polymer matrix was determined using Fourier Transform Infrared (FTIR). X-ray photoelectron spectroscopy (XPS) measurements were used to identify the binding energy between the polymer/cement nanocomposite used and the steel substrate. One important result from these tests was that incorporating ANPs decreasing

polymer crosslinking and results in a more flexible epoxy nanocomposite compared with neat epoxy.

Push-out tests were used to investigate the bond strength of shale-cement interfaces that had been repaired with different repair materials. Microphotographs showed the existence of microcracks at the cement-shale interface repaired with microfine cement, whereas repair with Novolac epoxy with and without alumina nanoparticles showed no gaps. This ability of epoxy and alumina nanoparticle-epoxy nanocomposite to penetrate the shale microcrack network at the interface created mechanical interlocks in addition to the adhesion between epoxy and shale. These interfacial microcracks at the shale surface also provide potential leakage pathways and thus compromise wellbore seal integrity. The penetration of the epoxy nanocomposite repair material not only improves the shale-cement bond strength, but it also seals leakage pathways adjacent to the interface and thus improves wellbore seal integrity.

The ability of repair materials to fill microcracks was investigated by injecting material into smooth-walled cracks with widths of 13, 25, 50, 75, and 100 microns formed between transparent plexiglass sheets. Microfine cement failed to fill microcracks with crack width lower than 50 microns. For 50, 75, and 100 microns crack width, microfine cement was able to partially fill the microcracks. However, the microfine cement was not uniformly distributed throughout the crack space. In addition, bleeding of microfine cement was observed during injection. On the other hand, neat Novolac epoxy and Novolac epoxy with 2% nanoalumina were able to 100% fill the crack width of 13 microns.

Integrated wellbore system testing

We have developed an experimental system to test wellbore specimens comprised of a cement sheath cast on a steel casing. The system allows independent application of confining pressures to 35 MPa and casing pressures to 20 MPa while gas flow is measured through the specimens along the wellbore axis at pore pressures up to 15 MPa. Wellbore specimens were created with various flaws, including cement fractures and microannuli between the steel casing and the cement. Thermal transients induced by cooling and heating the casing were used to produce flaws in the wellbore samples, consistent with wellbore damage from field operations that arises from temperature changes within a casing. We interpreted the hydraulic aperture of the flaws from gas flow measurements; we found from post-test measurements that the hydraulic aperture

compares well with the average actual (mechanical) aperture. The size (hydraulic aperture) of the microannuli ranged from less than 10 μm to more than 100 μm. This range appears to be on the order of the size of wellbore flaws implied from limited field measurements and observations of leaky wellbores.

Testing damaged wellbore samples revealed that flaws are capable of transmitting large flows. The flow rate through samples with microannuli is approximately 10^3 to 10^5 times the flow rate of intact wellbore cement. We also found that samples created with a corroded casing were comparable samples that had been thermally de-bonded.

We found that microannuli are fracture-like in how they deform in response to stress changes. With an increase in confining pressure, the hydraulic aperture of the microannulus decreases in a non-linear manner. Most often, the hydraulic aperture changes from loading are recovered during unloading. The microannuli response is less sensitive to casing pressure changes compared to confining pressure changes even when accounting for stiffness and geometric differences between loading the exterior of the cement sheath and loading the interior of the casing. In one instance, the cement sheath failed when the casing pressure was increased significantly above the confining pressure. This confirms another mechanism by which wellbores may become damaged.

We repaired a number of the flawed wellbore specimens. For samples with flaws less than about 50 μm, we repaired samples by injecting repair material under a nominal pressure of 0.7 MPa. Repair with the nanocomposite epoxy base material was successful in reducing the flow through flaws of various sizes and types to that equivalent to an intact cement. The repair remained effective after cycling the confining stress. In contrast, repair of flawed samples with microfine cement was initially less effective. In addition, the hydraulic aperture of the cement repaired sample increased with cycles of confining stress, indicating that the microfine cement repair was degrading.

After repair and testing, we sliced samples to allow for observations of the repair effectiveness. The nanocomposite epoxy base material appeared to fill all voids along the microannulus; in contrast, the microfine cement clearly did not. Image analysis of microphotographs of the cement-casing interface at a number of locations in a sample with a large microannulus were used to provide measurements of the actual (mechanical) aperture around the entire

circumference. These data reveal that the actual aperture is highly variable along the circumference of the cement-casing interface, and suggest that it is necessary for a repair material to penetrate sizes smaller than the average hydraulic aperture to effectively seal a microannulus. Our investigations also confirmed that realistic simulation of flow at the wellbore interface might not be possible without representative description of the actual aperture at the microannulus.

Modeling studies

Finite element (FE) analyses of the slant shear test configuration was conducted using ABAQUS modeling software. PNC was defined as a nonlinear elastic-plastic material using the constitutive stress-strain response measured in the uniaxial compression tests. Our objective was to use the validated FE model to realize the local shear stresses developed at failure of the slant shear test. As slippage occurs, the maximum local shear stress moves along the interface. Slant shear tests show that complete slippage occurs after the ultimate load due to release of energy as a result of bond failure. These results indicate that while incorporating nanoparticles in PC resulted in increasing the bond strength of PC to steel substrates, this improvement in bond strength when measured in terms of maximum local shear stresses is less significant than that measured using the apparent shear strength. Our simulations also confirmed the role of stiffness on stress development at the interface. It is apparent that improving wellbore integrity might not be accomplished through using materials with improved bond strength only, but also by engineering materials with specific stiffness that would minimize shear stresses under thermal and pressure gradients.

Numerical models were also developed of the laboratory integrated wellbore system test configuration, and included modeling flaws of varying dimensions along the casing-cement interface. A joint model was used to describe the hydraulic aperture of the microannulus region, where the mechanical stiffness is altered in response to the imposed stress state across the joint interface. The aperture-stress behavior is based upon laboratory measurements of hydraulic aperture as a function of imposed stress conditions. This investigation found that the microannulus elements reasonably reproduce laboratory behavior during loading from confining pressure increases. The calculated microannulus response to internal casing pressure changes

was less stiff than measured, which may be due to hardening of the microannulus during testing.

Even though modeling at the Field Scale and Wellbore Scale were not part of this projects objectives, the methodologies and results are presented to provide a more thorough discussion of the on-going research in this field. Modeling of field scale wellbore systems involved two distinct steps. First, a field scale model was developed that uses the stratigraphy, material properties, and injection history from a pilot CO_2 injection operation to develop stress-strain histories for wellbore locations from 100 to 400 meters from an injection well. The results from these models are used as input to a more detailed model of a wellbore system. Two separate wellbore-scale models have been developed during this study. The first model includes steel casing(s); cement surrounding the casing(s); and formation rock around everything, and was designed to evaluate the stresses induced on casing materials under shear loading. The second wellbore model contains a similar steel casing and cement or nanocomposite annulus representation for an entire length of borehole that matched the 100-m-spaced borehole columns of the field-scale model. The next step in this analysis process would be to transfer the computed stress, strain, pore pressure, and displacement histories for each borehole column in the field-scale model to the wellbore-scale model to evaluate the effects on the cement and nanocomposite epoxy.

Graphical material list

Fig. 3.8 – A sample with a microannulus created by the release film method. From left to right: sample at end of curing showing release film (plastic) on top of sample; cooling casing with liquid nitrogen; removing release film and casing; casing removed from cement sheath.
Fig. 3.9: Using dry ice to cool the casing and de-bond the steel casing and cement sheath
Fig. 3.10 – Casing with (left) and without (right) corrosion.
Fig. 3.11 – Figure showing the "epoxy capsule" method for injecting repair material into sample with flaws.
Fig. 3.12 – Sample 24 in pressure vessel with tube with epoxy. End cap was replaced and casing was pressurized in an attempt to inject epoxy into microannulus.
Fig. 3.13 – Analysis of non-linear flow for test on Sample 29 under 20.7 MPa confining pressure.
Fig. 3.14 – Flow rate through samples with representative seal system flaws. MA denotes microannulus. Microannulus is sample 11, large microannulus is sample 15, slot is sample 8, and cement fracture is sample 6.
Fig. 3.15 – Hydraulic aperture of sample 6 as a function of confining pressure.
Fig. 3.16 – Hydraulic aperture interpreted from flow measurements as a function of confining pressure for samples with small microannuli.
Fig. 3.17 – Hydraulic aperture vs. confining pressure on sample 52 (small microannulus).
Fig. 3.18 – Hydraulic aperture interpreted from flow measurements as a function of confining pressure for Sample 48.
Fig. 3.19 - Hydraulic aperture as a function of confining pressure for 1st, 10th, and 30th cycle of stress varying from 6.9 to 20.7 MPa (sample 48).
Fig. 3.20 – Hydraulic aperture interpreted from flow measurements as a function of confining pressure for Sample 51.
Fig. 3.21 – Hydraulic aperture interpreted from flow measurements as a function of confining pressure for Sample 29.
Fig. 3.22 - Hydraulic aperture as a function of casing pressure (black symbols) and calculated elastic contact stress (blue symbols) for test conducted at confining pressure of 14 MPa during (a) initial loading, and (b) unloading path.
Fig.3.23 – Hydraulic aperture vs. casing pressure for large microannulus at different confining pressures (sample 60).
Fig. 3.24– Hydraulic aperture as a function of calculated elastic circumferential stress. Confining pressure (CP) was held constant and casing pressure varied during these tests.
Fig.3.25 – Hydraulic aperture vs. effective stress for test on sample with large microannulus (sample 58).
Fig.3.26 – Hydraulic aperture vs. confining pressure for test on sample with corroded casing (sample 55).
Fig.3.27 – Hydraulic aperture vs. confining pressure for test on sample with corroded casing (sample 57).
Fig. 3.28 – Hydraulic aperture as a function of confining pressure for sample 7 (radial fracture) before and after repair.
Fig. 3.29 – Permeability vs. confining pressure for sample 7 (radial fracture) before and after repair.
Fig. 3.30 – Permeability reduction due to repair for sample 23.
Fig. 3.31– Permeabilities of sample 15 before and after repair.

References

ABAQUS 6.14 theory manual, ABAQUS online documentation.

Abdel Wahab, M., 2014. *The Mechanics of Adhesives in Composite and Metal Joints: Finite Element Analysis with ANSYS*, DEStech Publications Inc., Lancaster, PA, USA.

American Concrete Institute, ACI Committee 548 (2009), *Polymers and Adhesives in Concrete, State of the Art Report*, 2009.

American Petroleum Institute, API. (2009). "Specification for Cements and Materials for Well Cementing." *API Specification 10A*: Washington, DC.

ASTM C1437-07. (2007). "Standard Test Method for Flow of Hydraulic Cement." *ASTM International 2007*: West Conshohocken, PA.

ASTM C150 (2005). "Standard Specification for Portland Cement." *ASTM International 2005*: West Conshohocken, PA.

ASTM C305 (2005). "Standard Practice for Mechanical Mixing of Hydraulic Cement Pastes and Mortars of Plastic Consistency." *ASTM International 2005*: West Conshohocken, PA.

ASTM C882 (2013), "Standard Test Method for Bond Strength of Epoxy-Resin Systems Used With Concrete By Slant Shear", *ASTM International 2013*: West Conshohocken, PA.

ASTM C1583 / C1583M – 13 (2013), "Standard Test Method for Tensile Strength of Concrete Surfaces and the Bond Strength or Tensile Strength of Concrete Repair and Overlay Materials by Direct Tension (Pull-off Method)", *ASTM International 2013*: West Conshohocken, PA.

Bachu, S. and Bennion, D.B., 2009. Experimental assessment of brine and/or CO_2 leakage through well cements at reservoir conditions. Int. J. Greenhouse Gas Cont., 3, 494-501.

Bandis, S.C., Lumsden, A.C., and Barton, N.R., 1983. Fundamentals of rock joint de- formation. In: International Journal of Rock Mechanics and Mining Sciences & Geomechanics Abstracts. Vol. 20. 6. Elsevier, pp. 249–268.

Bear, J., 2013. Dynamics of fluids in porous media. Courier Corporation.

Bellabara, M., 2008. Ensuring Zonal Isolation Beyond the Life of the Well. Oilfield Review, Springer, 8 – 31.

Bois, A.P., Garnier, A., Galdiolo, G., and Laudet, J.B., 2012. Use of a mechanistic model to forecast cement-sheath integrity. SPE Drilling & Completion 27.02, pp. 303–314.

Brannon, R.A., A.F. Fossum, and O.E. Strack, 2009. KAYENTA: Theory and User's Guide. Sandia National Laboratories, SAND2009-2282. Albuquerque, NM.

Carey, J.W., Lewis, K., Kelkar, S., and Zyvoloski, G.A., 2013. Geomechanical Behavior of Wells in Geologic Sequestration. Energy Procedia 37, pp. 5642–5652.

Chekai, D., S. Bryant, and Q.Tao, 2013, Towards a Frequency Distribution of Effective Permeabilities of Leaky Wellbores, Energy Procedia 37, pp. 5653-5660.

Dewers, T., Newell, P., Broome, S., Heath, J., and Bauer, S., 2014. Geomechanical Behavior of Cambrian Mount Simon Sandstone Lithofacies, Iowa Shelf, USA. *International J. of Greenhouse Gas Control,* v. 21, p. 33-48.

Douba, A. E., Genedy, M., Matteo, E., Stormont, J., Reda Taha, M. M., "Apparent vs. True Bond Strength of Steel and PC with NanoAlumina", *Proceedings of International Congress on Polymers in Concrete (ICPIC)*, Singapore, Advanced Materials Research, Vol. 1129, pp. 307-314, Fun W. S. et al. Eds., Trans Tech Publications, October 2015.

Douba, A., Genedy, M., Matteo, E., Stormont, J., Reda Taha, M.M. "The Significance of Nanoparticles on Bond Strength of Polymer Concrete to Steel", *International Journal of Adhesion and Adhesives*, In Review, 2016.

Edwards, H. C., & Stewart, J. R. 2001. SIERRA: A Software Environment for Developing Complex MultiPhysics Applications. Amsterdam : Elsevier, 2001. In K. J. Bathe (ed.), First MIT Conference on Computational Fluid and Solid Mechanics.

Forchheimer, P., 1901. Wasserbewegung durch Boden, Zeitz ver Deutch Ing., 45, 1782-1788.

Gasda, S.E., Bachu, S., and Celia, M.A., 2004. Spatial characterization of the location of potentially leaky wells penetrating a deep saline aquifer in a mature sedimentary basin. Environmental geology 46.6-7, pp. 707–720.

Genedy, M., Stormont, J., Matteo, E. and Reda Taha, M. M. "Examining Epoxy-based Nanocomposites in Wellbore Seal Repair for Effective CO2 Sequestration", *Energy Procedia*, Vol. 63, pp. 5798-5807, 2014.

Genedy, M., Kandil, U. F., Matteo, E., Stormont, J., Reda Taha, M. M., "A new polymer nanocomposite repair material for restoring wellbore seal integrity", *International Journal of Greenhouse Gas*, In Review, 2016.

Gray, K.E., Podnos, E., and Becker, E., 2009. Finite-element studies of near-wellbore region during cementing operations: Part I. SPE Drilling & Completion 24.1, p. 127.

Hawkes, C.D., McLellan, P.J., and Bachu, S., 2005. Geomechnical Factors Affecting Geological Storage of CO_2 in Depleted Oil and Gas Reservoirs. J. Can. Petr.Tech. 44 (10), 2-61.

Hovorka, S.D., Meckel T.A., and Trevino, R.H., 2013. Monitoring a large-volume injection at Cranfield, Mississippi—Project design and recommendations, *International Journal of Greenhouse Gas Control*, v. 18, p. 345-360.

Hosseini, S.A., Lashgari, H., Choi, J.W., Nicot, J.P., Lu, J., and Hovorka, S.D., 2013. Static and dynamic reservoir modeling for geological CO_2 sequestration at Cranfield, Mississippi, U.S.A. *International Journal of Greenhouse Gas Control*, v. 18, p. 449-462.

Iwai, K., 1976. Fundamental studies of fluid flow through a single fracture. PhD thesis. University of California, Berkeley.

Khokhar, Z. R., I. A. Ashcroft, and V. S. Silberschmidt, 2011. Interaction of matrix cracking and delamination in cross-ply laminates: Simulations with stochastic cohesive zone elements. *Applied Composite Materials* 18.1, 3-16.

Kim, J. J., Rahman, M.K., Abdulaziz, A.A., Al-Zahrani, M. and Reda Taha, M.M (2013) "Nanosilica Effects on Composition and Silicate Polymerization in Hardened Cement Paste Cured under High Temperature and Pressure", *Cement and Concrete Composites*, Vol. 43, pp.78-85.

Kutchko, B.G., Strazisar, B.R., Dzombak, D.A., Lowry, G.V., and Thaulow, N., 2007. Degradation of well cement by CO_2 under geologic sequestration conditions. In: Environmental science & technology 41.13, pp. 4787–4792.

Lavrov, A., Todorovic, J., and Torsaeter, M., 2015. Numerical study of tensile thermal stresses in a casing-cement-rock system with heterogeneities, Proceedings of the 49th US Rock Mechanics / Geomechanics Symposium. San Francisco, CA, June 28 – July 1, paper ARMA 15-110.

Lu, J., Kordi, M., Hovorka, S.D., Meckel, T.A., Christopher, C.A., 2012c. Reservoir characterization and complications for trapping mechanisms at Cranfield CO_2 injection site. *International Journal of Greenhouse Gas Control*, Vol. 18, 361-374, October 2013.

Martinez, M.J., Stone, C.M., Notz, P.K., et al., 2011. Computational Thermal, Chemical, Fluid and Solid Mechanics for Geosystems Management. Tech. Rept. SAND2011-6643. Sandia National Laboratories, Albuquerque, NM.

Martinez, M.J., P. Newell, J.E. Bishop, and D.Z. Turner, 2013. Coupled multiphase flow and geomechanics model for analysis of joint reactivation during CO_2 sequestration operations, *Int. Journal of Greenhouse Gas Control*, Vol. 17, 148-160, September 2013.

Matteo, E.N. and Scherer, G.W., 2012. Experimental study of the diffusion controlled acid degradation of Class H Portland cement. In: International Journal of Greenhouse Gas Control 7, pp. 181–191.

Meo, M. and E. Thieulot. Delamination modeling in a double cantilever beam. *Composite Structures* 71 (2005); 429-434.

National Energy Technology Lab, 2011. Carbon Sequestration Program: Technology Plan: Enhancing the Success of Carbon Capture and Storage Technologies. Applied Research

and Development from Lab- to Large-Field Scale, 52 p. http:// www.netl.doe.gov/technologies/carbon seq/refshelf/2011 Sequestration Program Plan.pdf.

Nicot, J-P., C. M. Oldenburg, J. E. Houseworth, and J-W. Choi, 2013. Analysis of potential leakage pathways at Cranfield, MS, U.S.A., CO_2 sequestration site, *International Journal of Greenhouse Gas Control*, v. 18, p. 388-400.

Nordbotten, J.M., Celia, M., and Bachu, S., 2004. Analytical solutions for leakage rates through abandoned wells. Water Resources Research 40.4.

Nordbotten, J.M., Celia, M., and Bachu, S., 2005a. Injection and storage of CO_2 in deep saline aquifers: Analytical solution for CO_2 plume evolution during injection. Transport in Porous media 58.3, pp. 339–360.

Nordbotten, J.M., Celia, M., Bachu, S., and Dahle, H. ,2005b. Semianalytical solution for CO_2 leakage through an abandoned well. Environmental science & technology 39.2, pp. 602–611.

Notz, P.K., Subia, S.R., Hopkins, M.M., Moffat, H.K., Noble, D., 2007. Aria 1.5: User Manual SAND2007-2734. Sandia National Laboratories Technical Report, Albuquerque, NM.

Orlic, B., 2008. Some Geomechanical Aspects of Geological CO_2 Sequestration. Proceeding of the 12th International Conference of International Association for Computer Methods and Advances in Geomechanics , Goa, India, 1-6 October, 2204 – 2212.

Philippacopoulos, A.J. and Berndt, M.L., 2001. Mechanical property issues for geothermal well cements. Transactions Geothermal Resources Council, pp. 119–124.

Renshaw, C.E., 1995. On the relationship between mechanical and hydraulic apertures in rough-walled fractures. Journal of Geophysical Research: Solid Earth (1978–2012) 100.B12, pp. 24629–24636.

Rinehart, A., 2015. Mechanical Variability and Constitutive Behavior of the Lower Tuscaloosa Formation at Reservoir Conditions in the Presence of CO_2. Dissertation, New Mexico Institute of Mines and Technology, Socorro, New Mexico.

Schreppers, G., 2015. A framework for wellbore cement integrity analysis. ARMA 15-349 Proceedings of the 49th US Rock Mechanics-Geomechanics Symposium, San Francisco, CA, USA. American Rock Mechanics Association.

Seidel, F.A. and Greene, T.G., 1985. Use of Expanding Cement Improves Bonding and Aids in Eliminating Annular Gas Migration in Hobbs Grayburg-San Andres Wells. Paper SPE 14434 presented at the SPE Annual Technical Conference and Exhibition, Las Vegas, Nevada, USA, 22–25 September. DOI: 10.2118/14434-MS.

Soliman, E., Kandil, U. F., Reda Taha, M.M. (2012a) "The Significance of Carbon Nanotubes on Styrene Butadiene Rubber (SBR) and SBR Modified Mortar", *Materials and Structures*, Vol. 45, No. 6, pp. 803-816.

Soliman, E., Al-Haik, M., Reda Taha, M.M. (2012b), "On and off-axis tension behavior of fiber reinforced polymer (FRP) composites incorporating multi-walled carbon nanotubes", *Journal of Composite Materials*, V. 46, No. 14, 2012, pp. 1661–1675

SIERRA Solid Mechanics Team, 2010. Adagio 4.18 User's Guide. SAND2010-6313, Sandia National Laboratories, Albuquerque, New Mexico.

SIERRA Solid Mechanics Team, 2011. Sierra/Solid Mechanics 4.22 User's Guide. SAND2011-7597, Sandia National Laboratories, Albuquerque, New Mexico.

Souley, M., Homand, F., and Amadei, B.,(1995). An extension to the Saeb and Amadei constitutive model for rock joints to include cyclic loading paths. International journal of rock mechanics and mining sciences & geomechanics abstracts. Vol. 32. 2. Elsevier, pp. 101–109.

Stormont, J.C., Ahmad, R. Ellison, J., Reda Taha, M. M. , and E.N.Matteo, 2015. Laboratory measurements of flow through wellbore cement-casing microannuli, ARMA 15-294, Proceedings of the 49th US Rock Mechanics/Geomechanics Symposium, San Francisco, CA, USA, 28 June- 1 July 2015.

Ugwu, I.O., 2008. Cement fatigue and HPHT well integrity with application to life of well prediction. PhD thesis. Texas A&M University.

Witherspoon, P.A., Wang, J.S., Iwai, K., Gale, J.E., 1980. Validity of cubic law for fluid flow in a deformable rock fracture. Water Res. Res. 16 (6), 1016-1024.

Zhang, M. and Bachu, S., 2011. Review of integrity of existing wells in relation to CO_2 geological storage: What do we know? Int. J. Greenhouse Gas Cont. 5, 826-840.

List of Acronyms and Abbreviations

ACI:	American Concrete Institute
ANPs:	Alumina nanoparticles
API:	American Petroleum Institute
ASTM:	American Socitey for Testing Materials
CCVD:	Catalysed Chemical Vapor Deposition
COOH:	Carboxyl group
CNTs:	Carbon Nanotubes
HSR:	High sulfate-resistant cement
MSR:	Moderate sulfate-resistant cement
MWCNTs:	Multi-wall carbon nanotubes
OWC:	Oil Well Cement
PCNC:	Polymer/cement nanocomposite
PNC:	Polymer nanocomposite
SBR:	Styrene-Butadiene Rubber copolymer

Appendix A

Cost Estimate Information for Application of Wellbore Seal Repair Technology

This appendix contains a stand-alone report submitted on December 16, 2013.

Cost Estimate Information for Application of Wellbore Seal Repair Technology

A. 1 Summary

This project involves developing nanocomposite wellbore repair materials for repairing leaky wellbores. These materials are intended to replace conventional materials in repair operations. In particular, these materials are intended to be used in "squeeze" operations which are directed at injecting repair material into the flaws and voids in the cement-filled annulus between the casing and formation. The deployment of these materials in repair operations is expected to utilize existing equipment and methods. The cost of using these materials is the cost of bulk materials plus any additional material preparation beyond that required for conventional materials. The epoxy materials used as the base for the nanocomposites are comparable to conventional polymer materials; therefore, the materials cost beyond the conventional approach is that associated with the nanomaterials themselves. In addition, the processing step of dispersing the nanomaterials within the epoxy is an extra cost. In total, the nanocomposites are estimated to cost between 10 and 30% more than conventional materials. This cost should be balanced with the benefits from the improved performance of the nanocomposites relative to conventional materials.

A. 2 Motivation

The seal integrity of abandoned wellbores is central to ensuring permanent storage of CO_2 in geologic formations. A wellbore that intersects the storage formation represents a potential leakage pathway that can lead to subsurface migration of stored CO_2 and/or subsequent venting of stored CO_2 to the surface. In terms of potential risk for leakage, wells can be broadly divided into 3 categories: 1) future wells, 2) low leakage-risk abandoned wells, and 3) high leakage-risk abandoned wells. Both geographic location and time period of abandonment -- and practices and regulations, if any, in place at the time of abandonment -- have a significant impact on whether or not an abandoned well falls into the low leakage-risk or high leakage-risk category (Watson and Bachu 2008). Both future wells and low leakage risk abandoned wells are of lower priority with respect to preventing leakage, as best practices for well completion and abandonment implemented can greatly reduce the occurrence of factors that increase the risk of wellbore leakage (IEA 2009, NETL 2011).

Since there can be thousands of wells that intersect a subsurface formation used for CO_2 storage, it can be expected that an appreciable fraction of such wells were likely drilled/completed/abandoned before current best practices were put into practice. Such wells represent an increased risk for leakage, and it is likely that at a typical storage operation, reworking or recompleting leaky or high risk of leakage wells will be an important part of ensuring permanent storage. Even using today's technology, the number of wells that suffer from bad cement jobs and are therefore likely to be leaky has been estimated in the range

of 15% (King, 2011; Conca, 2012). Future degradation of wellbores is likely in response to mechanisms such as formation compaction and internal wellbore pressure and temperature cycling during operations. It is clear that addressing leaky wells is a requirement for successful CO_2 sequestration.

Well repair, as opposed to re-completion, may be both economically and technically preferable in certain contexts. Since there is heterogeneity of failure modes that can be specific to a particular well (or group of wells), a portfolio of repair techniques/options may be best suited to ensuring seal integrity in a cost effective manner.

A. 3 Repair technology

Conventional technology for repairing leaky wellbores typically involves "squeezing" cement into the annulus behind the casing. Penetration into the microannulus and small cracks can be problematic with conventional cements due to the size of the cement constituents. Microfine cement is comprised of smaller particle sizes compared to conventional cement and is intended to increase penetration into small cracks; however, the fundamental problem of adhesion versus cohesion bond failure of cement and steel casing in the downhole environment is not addressed by most cement-based materials. Adhesion failure is characteristically brittle and unpredictable -- classical cement-steel failure is a typical adhesion failure. For these and other reasons, squeeze jobs with cements are not always successful. It has been reported that three squeezes are typically required to fix a problem in a cement job (King, 2011). Costs for squeeze jobs are highly variable, but have been reported to be on the order of $500k to $1.5M (e.g., Rusch and Slezak, 2005; Halliburton, 2013). In some cases squeeze jobs are not successful, and a very expensive re-completion of the well may be required.

Specialty materials have been developed to provide repair materials that address some of the shortcomings of cementitious materials. In particular, non-particulate chemical grouts (polymers) are able to penetrate smaller flaws than cementitious materials. These materials are expected to be more effective than cementitious materials in many situations. While they be more expensive on a per unit weight or volume basis compared to cementitious materials, they are often a cost-effective solution as their use should result in fewer instances where squeeze jobs have to be repeated compared to cementitious materials.

The repair materials we are developing in this project are the "next generation" of repair materials, and can be compared with the polymers that have are presently being used in repair operations. The nanocomposites being developed in this project have the distinct advantages of being more durable in the expected conditions in production wells, being more ductile and having a better bond to the casing. Thus, it is likely that the use of nanocomposites will result in fewer instances where the repair will fail

compared to conventional materials. Furthermore, the nanocomposites should be effective for a longer duration compared to other repair materials.

A. 4 Cost estimate information for nanocomposite wellbore seal repair material

The most straightforward approach to evaluating the cost of nanocomposite wellbore repair material is to compare their incremental or additional costs compared to the polymers that are sometimes used for wellbore repair. As the nanocomposites being developed in this project are being formulated with conventional epoxies, we assume that the cost of the epoxy is comparable to existing commercial products and therefore additional cost is due to the addition of the nanomaterials. The costs associated with the nanomaterials are the material costs and additional costs associated with incorporating the nanomaterials into the epoxies.

There are two important considerations regarding the costs of nanomaterials. First, their costs continue to decline dramatically as the technology for their production develops. Second, there is an economy of scale associated with industrial users that is difficult to estimate at this time. Cost estimates used here are for relatively small quantities at today's prices, and will therefore likely be conservative (high).

We have developed and tested nanocomposite repair materials with various nanomaterials, including carbon nanotubes, nanosilica, nanoclay, and nanoalumina. Each nanomaterials has its attributes, and therefore, we have included cost estimates for all of these materials in Table A.1 below.

Table A.1 - Costs of nanomaterials under consideration for repair nanocomposites.

Nanomaterial	Cost per kg	Source
Carbon nanotubes	$210	http://www.cheaptubesinc.com/carbon-nanotubes-prices.htm#Multi_Walled_Nanotubes_Prices
Nanosilica	$8	http://www.alibaba.com/showroom/nano-silica-powder.html
Nanoclay	$220	http://www.sigmaaldrich.com/catalog/product/aldrich/685445?lang=en&region=US
Nanoalumina	$150	http://www.aliexpress.com/price/nano-alumina-price.html

The amount of nanomaterials used on a weight basis in the repair nanocomposites under development is on the order of 1%. If we assume an epoxy cost of $10/kg, then adding 1% of carbon nanotubes, nanoclay or nanoalumina adds on the order of 20% to the cost of the nanocomposite compared to the conventional material. Using nanosilica adds about 1% to the cost of the nanocomposite relative to the conventional material.

To create an effective nanocomposite material, it is critical to disperse the nanomaterial throughout the epoxy resin. This dispersion represents an additional step in processing beyond that required for conventional materials. Dispersion is achieved by essentially mixing the nanomaterials in the epoxy resin but at very high velocities and/or with sonification. Our first order estimate based on the scaling up laboratory operations is that this step could add up to 10% to the material cost.

Thus, the combined materials and processing costs are estimated that nanocomposites are approximately 10 to 30% more costly than conventional polymer materials.

The amount of material required for a repair job depends on the particular conditions associated with the leaky wellbore and is highly variable. The reported range of quantities per squeeze is on the order of 100 to 1000 gallons (Creel and Crook, 2008; Halliburton, 2012). The materials cost as a function of the squeeze volume is shown in Figure A.1 below assuming the nanocomposite repair material costs 20% more than conventional material.

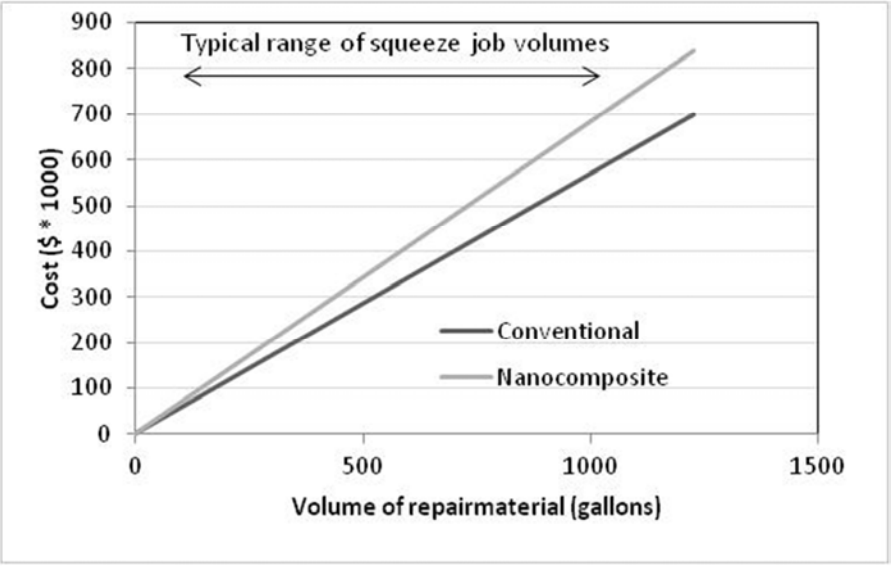

Figure A. 1 – Cost of conventional and nanocomposite wellbore seal repair material as a function of the volume of repair material required for a squeeze job.

A. 5 References

Conca, J., 2012, The Fracking Solution is a Good Cement Job, Forbes, Blog. (http://www.forbes.com/sites/jamesconca/2012/09/10/the-fracking-solution-is-a-good-cement-job/)

Creel, P. and R.J. Crook, 2008, Cementing: Injectrol and PermSeal Sealants Repair Leaks, Restore Integrity to Casings, Halliburton Energy Services, Inc.

Halliburton, 2012, WellLock Resin System, Sales Presentation. (http://www.halliburton.com/public/cem/contents/Presentations/TECH/MM/WellLock%20Resin%20Sales%20Presentation.pptx)

Halliburton, 2013, A Case Study: Halliburton Advanced Cement Evaluation service saved operator $1.2 million and 16 days of rig time, Document HO10341. (http://www.halliburton.com/public/lp/contents/Case_Histories/web/H010341.pdf)

IEA Greenhouse Gas &D Programme (IEA GHG), 2009, Long Term Integrity of CO_2 Storage – Well Abandonment., 2009/08, July 2009.

King, G., 2011, Cementing, GEK Engineering presentation. (http://gekengineering.com/Downloads/Free_Downloads/Cementing.pdf)

National Energy Technology Laboratory (NETL), 2011, Best Practices for Carbon Storage Systems and Well Management Activities. *DOE/NETL-2001/1458*, December.

Rusch, D.W. and M.T. Slezak, 2005, Annulus Communications Eliminated using Pressure-Activated Sealant, Spring 2005 Conference, April 17-20, Syracuse, NY.

Watson, T.L., and Bachu, S., 2008, Identification of Wells With High CO2-Leakage Potential in Mature Oil Fields Developed for CO2-Enhanced Oil Recovery. *SPE* 112924-MS.